Alma Mater Studiorum · University of Bologna

School of Science
Department of Physics and Astronomy
Master Degree in Physics

Reconstruction of neutrino events with scintillation light in the SAND detector

Supervisor:
Dr. Gabriele Sirri

Co-supervisors:
Dr. Valentina Cicero
Dr. Nicolò Tosi

Submitted by:
Giacomo Santoni

Academic Year 2022/2023

Abstract

The Deep Underground Neutrino Experiment (DUNE) is a next-generation long-baseline accelerator experiment under construction in the United States which aims to address the open questions in neutrino physics, by measuring several undetermined parameters, such as the mass ordering and the CP violating phase.

DUNE will consist of a Near and a Far Detector complex, $\sim$ 1300 km apart. One of three sub-components of the Near Detector complex is the SAND apparatus, which will include GRanular Argon for Interaction of Neutrinos (GRAIN). GRAIN is a novel liquid Argon detector that aims at imaging neutrino interactions with scintillation light detected through an optical readout system based on *coded aperture cameras*, which allow to obtain a voxelized distribution of the photon emission.

This work aims to assess the performance of a track finding algorithm for the reconstruction of charged-current quasi-elastic neutrino interactions in the GRAIN volume. A convolutional neural network algorithm is implemented to filter the cameras suitable for the voxel reconstruction, improving the dataset purity. From the 3D reconstructed voxel distribution a sequence of algorithms has been optimized to obtain track candidates. A comparison between the reconstructed tracks and the Monte Carlo truth is carried out obtaining a good match of the vertex position with an excellent estimate of the track direction.

Contents

Introduction

Neutrinos are the most abundant known matter particles in the Universe. Although they appear in the Standard Model as massless particles, the evidence of the flavour oscillations implies a non-zero neutrino mass. Experimental studies of this phenomenon have led to determine many of the parameters linked to neutrino masses, by using several complementary channels and sources. However, the determination of some parameters, such as the ordering of neutrino masses, the CP violating phase and the value of θ_{23} mixing angle, represents a still open question. Next generation experiments are being built to search for these unknowns and to find which is the most suitable model for their description.

The Deep Underground Neutrino Experiment (DUNE) will be an accelerator-based experiment that will utilize the highest power neutrino beam, peaked at 2.5 GeV, a Near Detector at Fermilab, and a Far Detector at the Sanford underground laboratories in South Dakota, $\sim$ 1300 km away. It will measure the neutrino mass ordering, the CP violation phase, and the consistency of the three-flavour paradigm. The Far Detector will consist of four Liquid Argon Time Projection Chambers, with an overall mass of 68 ktons, which allow the identification of several neutrino processes. At the near site a detector complex will contribute to the analysis of the Far Detector data, by providing complementary information with measurements on the neutrino beam on- and off-axis and by refining the neutrino interaction models.

At the Near Detector complex, SAND is a multipurpose detector composed of a superconducting solenoidal magnet that surrounds a calorimeter, repurposed from the KLOE experiment at the INFN Frascati laboratories. An inner tracker and an active $\sim$ 1 ton liquid argon target (GRAIN) are placed inside the magnetic volume. SAND will continuously monitor the beam by performing tracking and calorimetric measurements of neutrino interactions. GRAIN and the downstream tracker will also contribute to neutrino interaction model studies and to constrain nuclear effects, by providing a large sample of neutrino interactions on different nuclear targets.

The GRAIN sub-detector is equipped with *coded aperture cameras* and relies on a novel technique: the imaging of the argon scintillation light produced by the passage of a charged particle. A camera is composed of a coded aperture mask, which has a specific pattern of holes, and a SiPM matrix as an image sensor. Thanks to the geometric properties of the coded mask, the voxelized region of photon emission can be estimated from the detected image with a suitable algorithm.

Starting from this voxel distribution, this work aims to assess the performance of a track finding algorithm for the reconstruction of charged-current quasi-elastic neutrino events in the GRAIN volume. Sometimes, the photons can be produced in the region between the mask and the sensors, "dazzling" the camera. Since the reconstruction technique can only exploit "non-dazzled" cameras, for a more ac-

curate estimate of the photon source distribution, it is necessary to exclude the dazzled ones. To this end, we implemented a deep-learning algorithm that classifies the cameras. After obtaining the voxel score, applying a selection cut and voxel distribution clustering, we employed the local principal curve algorithm to identify the set of points (referred to as ℓpc points) that best approximate this distribution. Subsequently, employing the Hough transform method, we identified the collinear points from these ℓpc points and performed linear fitting on them. As a final step, we estimated the direction of the produced particles. The performance of the reconstruction process was assessed comparing the results with the Monte Carlo truth.

In chapter 1 an overview of the main properties of neutrinos, their interactions and of the oscillation phenomenon is presented; furthermore, the main neutrino experiments and the open questions are explained. Chapter 2 presents the DUNE experiment with the detector design, its physics motivations, and sensitivity. In chapter 3 a detailed description of the SAND detector and its physics goals, with a particular focus on the GRAIN sub-detector, is provided. In chapter 4, the description of the pre-existing simulation and photon distribution reconstruction is presented. In chapter 5 the implementation and the results of a Deep Learning algorithm to filter GRAIN data are discussed. In chapter 6 the track reconstruction process and fitting method are presented. Finally, the reconstructed particle directions are compared to the corresponding Monte Carlo truth.

Chapter 1

Neutrino Physics

1.1 Neutrino in Standard Model

The Standard Model (SM) of particle physics is a gauge theory, based on the QFT framework, obtained from the composition of three local gauge symmetries: $SU(3)_C \times SU(2)_L \times U(1)_Y$, where the labels C, L, Y denote colour, left-handed chirality and weak hypercharge. It describes three out of the four fundamental interactions: the strong, the weak and the electromagnetic interaction, except gravity. In particular, $SU(3)_C$ describes the strong interaction, $SU(2)_L$ the weak interaction, and the electromagnetic $U(1)_{QED}$ is hidden inside $U(1)_Y$.

The SM is based upon the idea that the matter is made up of fermions, spin-1/2 point-like particles, that interact through fields, that have integer-spin particles associated, called bosons [1]. Fermions are divided into two sectors, quarks and leptons, and, in each sector, the constituents are arranged as follows:

$$\begin{pmatrix} e^- \\ \nu_e \end{pmatrix} \begin{pmatrix} \mu^- \\ \nu_\mu \end{pmatrix} \begin{pmatrix} \tau^- \\ \nu_\tau \end{pmatrix}, \begin{pmatrix} u \\ d \end{pmatrix} \begin{pmatrix} c \\ s \end{pmatrix} \begin{pmatrix} t \\ b \end{pmatrix}$$

Quarks feel all the three interactions of SM; electrons, muons and taus feel only the weak and the electromagnetic ones.

Neutrinos inside the SM are neutral and massless fermions and can interact only weakly. They were hypothesized by W. Pauli in 1931 and then observed for the first time by Reines and Cowan in 1956. They are part of the lepton doublet $L_L = \begin{pmatrix} l \\ \nu_l \end{pmatrix}_L$, where the subscript L denotes the left-handed component of the fermion. Considering only ν_{l_L} by assumption, neutrinos in SM are massless. Their interactions can be mediated by a neutral current, through Z^0 boson, or a charged current, with $W^\pm$. The correspondent lagrangians are:

$$\mathcal{L}_{I,L}^{CC} = -\frac{g}{\sqrt{2}} \sum_{\alpha=e,\mu,\tau} \bar{l}_{\alpha_L} \gamma^\mu \nu_{\alpha_L} W_\mu^- + \text{H.c.}, \tag{1.1}$$

$$\mathcal{L}_{I,L}^{NC} = -\frac{g}{2cos\theta_W} \sum_{\alpha=e,\mu,\tau} \overline{\nu}_{\alpha_L} \gamma^\mu \nu_{\alpha_L} Z_\mu^0 \tag{1.2}$$

where g is the coupling associated with the electro-weak $SU(2)_L$ interaction and θ_W is the Weinberg angle.

The SM provides three generations of neutrinos, observed in 1956 (ν_e), in 1962 (ν_μ) and in 2000 (ν_τ). This is justified basically by two facts:

1. Z-boson decay: Z boson decays 70% of the time into hadrons, 10% into charged leptons and 20% into neutral leptons, i.e. neutrinos, where the "invisible" part is predicted to be twice than the charged leptons' ones. This was measured at LEP [2], and the resulting number of neutrino types was:

$$N_\nu = \frac{\Gamma_{inv}}{\Gamma_l}\left(\frac{\Gamma_l}{\Gamma_\nu}\right)_{SM} = 2.984 \pm 0.008$$

   The observation of this fact confirmed the existence of three flavours of neutrinos, below $m_0/2 = 45$ Mev/c^2.

2. Influence on cosmic signals of neutrinos produced during the first seconds after the Big Bang: three generations of neutrinos are indeed consistent with the explanation of the ratio of light elements, with the description of the fluctuations of the cosmic microwave background and with the pattern of the baryon acoustic oscillations.

However, the flavour oscillation of neutrinos has been discovered for many years, and massive neutrinos are needed to explain this phenomenon. For this reason, it is necessary to go beyond the SM theory, as we will see in Sec. 1.2.

1.2 Neutrinos beyond Standard Model

The SM is the most complete theory in describing the particle physics world and in making predictions, but it fails to explain some observed phenomena. For example, one such phenomenon is the experimental evidence of the neutrino oscillation. It was first hypothesized in 1957 by Pontecorvo [3] before the unexpected results of the Homestake experiment [4] and definitely claimed in 2003 thanks to the SNO experiment [5]. This discovery was a breakthrough in particle physics since it can be explained only by assuming that neutrinos have mass, that is in contrast with the SM predictions. Hence, this opened the era of the "new physics", for which a Beyond Standard Model (BSM) theory is needed. Indeed, this observation led to a lot of still open questions: the absolute mass scale of neutrinos, the mechanism through which they gain mass and the reason why it is so small compared to the other particles. In the next sections, some theories on neutrino mass are outlined.

1.2.1 Neutrino masses

Dirac mass

The Dirac lagrangian for a free fermion is:

$$\mathcal{L}_D = \overline{\nu}_L i\partial\!\!\!/ \nu_L + \overline{\nu}_R i\partial\!\!\!/ \nu_R - m(\overline{\nu}_L\nu_R + \overline{\nu}_R\nu_L) \tag{1.3}$$

where $\partial\!\!\!/ \equiv \gamma^\mu \frac{\partial}{\partial x^\mu}$. Here, the lagrangian is written in chiral components, such that $\nu_{R/L} = P_{R/L}\nu = \frac{1\pm\gamma_5}{2}\nu$. As said before, in the SM, only ν_L are considered by

assumption, so the mass term vanishes. Anyway, since all the fermions in SM have both left and right components, the simplest way to give mass to neutrinos is using an extension of the Higgs' mechanism, introducing a right-handed neutrino ν_R and describing the particle through a four-component spinor:

$$\nu = \begin{pmatrix} \psi_R \\ \psi_L \end{pmatrix} = \begin{pmatrix} \psi_{R1} \\ \psi_{R2} \\ \psi_{L1} \\ \psi_{L2} \end{pmatrix}$$

So, defining a modified Higgs field $\tilde{\Phi} = i\sigma_2\Phi^*$, with $\Phi = \frac{1}{\sqrt{2}}\begin{pmatrix} 0 \\ v+H \end{pmatrix}$, we can rewrite the Lepton-Higgs Yukawa lagrangian as:

$$\mathcal{L}_{H,L} = -\left(\frac{v+H}{\sqrt{2}}\right)\left[\bar{l}'_L Y'^{l} l'_R + \overline{\nu}'_L Y'^{\nu} \nu'_R\right] + \text{H.c.} \tag{1.4}$$

Changing basis of lepton fields, with a unitary matrix V, Y' becomes diagonal, yielding to:

$$\begin{aligned} \mathcal{L}_{H,L} &= -\left(\frac{v+H}{\sqrt{2}}\right)\left[\bar{\boldsymbol{l}}_L Y^l \boldsymbol{l}_R + \overline{\boldsymbol{n}}_L Y^\nu \boldsymbol{n}_R\right] + \text{H.c.} = \\ &= -\left(\frac{v+H}{\sqrt{2}}\right)\left[\sum_{\alpha=e,\mu,\tau} y^l_\alpha \bar{l}_{\alpha L} l_{\alpha R} + \sum_{k=1}^{3} y^\nu_k \overline{\nu}_{kL} \nu_{kR}\right] + \text{H.c.} = \\ &= -\sum_{\alpha=e,\mu,\tau} \frac{y^l_\alpha v}{\sqrt{2}} \bar{l}_\alpha l_\alpha - \sum_{k=1}^{3} \frac{y^\nu_k v}{\sqrt{2}} \overline{\nu}_k \nu_k - \sum_{\alpha=e,\mu,\tau} \frac{y^l_\alpha}{\sqrt{2}} \bar{l}_\alpha l_\alpha H - \sum_{k=1}^{3} \frac{y^\nu_k}{\sqrt{2}} \overline{\nu}_k \nu_k H, \end{aligned} \tag{1.5}$$

where $V^{l\dagger}_{L/R} \boldsymbol{l}'_{L/R} = \boldsymbol{l}_{L/R}, V^{\nu\dagger}_{L/R} \boldsymbol{\nu}'_{L/R} = \boldsymbol{n}_{L/R}$ and charged lepton and neutrino masses are respectively $m_l = y^l_\alpha v/\sqrt{2}$ and $m_\nu = y^\nu_k v/\sqrt{2}$. It can be observed that the lepton - Higgs coupling is proportional to the lepton mass.

Majorana mass

A massless neutrino can be described by a Weyl spinor. However, in 1937 Majorana [6] showed that also a massive neutrino can be described by a two-component spinor ν, if ν_L and ν_R are not independent:

$$\nu_R = \nu^C_L = \mathcal{C}\overline{\nu}^T_L \rightarrow \nu = \nu^C$$

with the spinor:

$$\nu = \begin{pmatrix} i\sigma_2 \chi^*_L \\ \chi_L \end{pmatrix} = \begin{pmatrix} \chi^*_{L2} \\ -\chi^*_{L1} \\ \chi_{L1} \\ \chi_{L2} \end{pmatrix}$$

The Majorana equation is:

$$i\partial\!\!\!/ \nu_L = m\nu^C_L \tag{1.6}$$

and the correspondent lagrangian is:

$$\mathcal{L}^M = \overline{\nu}_L i\partial\!\!\!/ \nu_L - \frac{m}{2}(\overline{\nu}_L^C \nu_L + \overline{\nu}_L \nu_L^C) \tag{1.7}$$

The mass term in Eq. 1.7 clearly violates the lepton number conservation ($\Delta L = \pm 2$) and so a BSM theory is needed to explain how neutrinos gain mass [7].

1.2.2 Experimental mass measurements

β decay experiments

Electron neutrino mass can be measured by observing the electron energy spectrum in a β-decay. If m_{ν_e} is small, its effect on the electron spectrum is maximal at the end-point of the spectrum, where the events are very rare. To maximize the fraction of decay events that occur in this region, it is better to use a reaction with the smallest Q-value possible. The best reaction for this goal is the tritium β-decay, $^3\mathrm{H} \rightarrow {}^3\mathrm{He} + e^- + \overline{\nu}_e$, since it has one of the smallest Q-value among all known β-decays. For these measurements, it's useful to define the so-called "Kurie function":

$$K(T) = \left[(Q_\beta - T)\sqrt{(Q_\beta - T)^2 - m_{\nu_e}^2}\right]^{1/2} \tag{1.8}$$

where $Q = M(^3\mathrm{H}) - M(^3\mathrm{He}) - m_e = 18.58$ keV.
If $m_{\nu_e} = 0$, then $K(T)|_{m_{\nu_e}=0} = Q_\beta - T$, that is a linear relation on T. While, if the mass is non-null, there is a deviation from the linear function, as can be seen in Fig. 1.1.

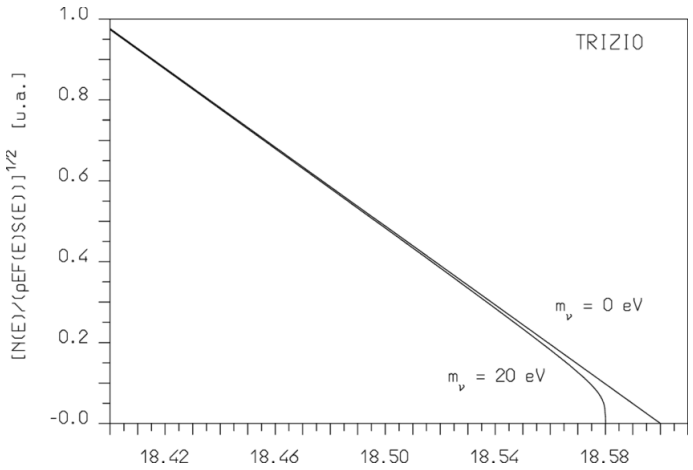

Figure 1.1: Tritium Kurie plot, near to the end-point, computed for neutrino masses of 0 eV and 20 eV [8].

As explained in Sec. 1.3, neutrinos can be seen as a superposition of different mass eigenstates, but in this context, the electron neutrino is considered as a mass eigenstate. A similar, but more complex, analysis can be carried out considering the neutrino mixing. Such a precise measurement is extremely challenging, therefore, only an upper limit on the value of m_{ν_e} has been obtained. The strongest constraint, given by the KATRIN experiment, that combined two data-taking campaigns, is $m_{\nu_e} < 0.8$ eV at 90% C.L. [9]

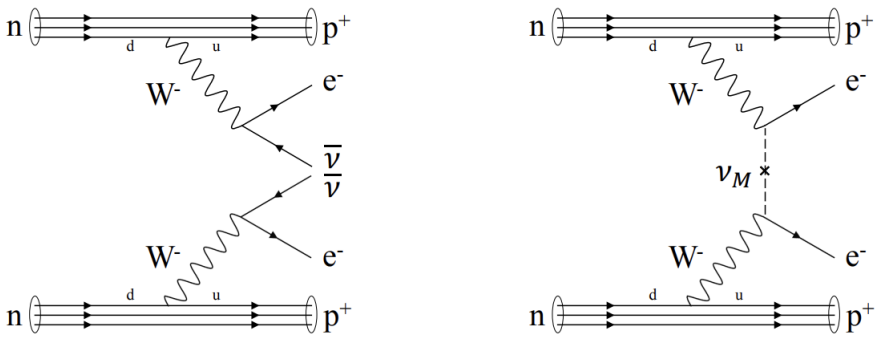

Figure 1.2: Feynman diagrams of the double β decay (left) and of the neutrinoless double β decay (right) [10].

This reaction, however, can't solve the neutrino Dirac or Majorana nature since the effect of neutrino mass for this method is due to a kinematical relation that is satisfied by both fields.

Neutrinoless double β decay experiments

Neutrinoless double β decay ($2\beta_{0\nu}$-decay) is the golden channel to measure neutrino mass and to test if they are Majorana particles.
Double β decay ($2\beta_{2\nu}$) is the following process:

$$\mathcal{N}(A,Z) \rightarrow \mathcal{N}(A,Z \pm 2) + 2e^{\pm} + 2\overset{(-)}{\nu}_e. \tag{1.9}$$

where (A, Z) are the mass number and the atomic number of the nucleus, respectively. It is a second-order process in the perturbative expansion of weak interactions in the SM, hence it is observable in practice only if the single β-decay is forbidden or strongly suppressed. The $2\beta_{0\nu}$ decay is the same as Eq. 1.9 but without neutrinos in the final state. It occurs only if neutrinos have mass, which has been proven, and if neutrinos are Majorana particles and there is no lepton number conservation. The last two requirements have not been verified yet, but are crucial for the observation of the decay: in particular, the Majorana nature of neutrinos would allow the interaction, since a neutrino and antineutrino would be the same particle. The Feynman diagrams of these processes are shown in Fig. 1.2.

The $2\beta_{0\nu}$ half-life of a nucleus can be obtained from:

$$[T^{0\nu}_{1/2}(\mathcal{N})]^{-1} = G^{\mathcal{N}}_{0\nu} |\mathcal{M}^{\mathcal{N}}_{0\nu}|^2 \frac{\langle m_{\beta\beta} \rangle^2}{m_e^2} \tag{1.10}$$

where $G^{\mathcal{N}}_{0\nu}$ and $\mathcal{M}^{\mathcal{N}}_{0\nu}$ are the phase space factor and the nuclear matrix element, respectively, $\langle m_{\beta\beta} \rangle = |\sum_i U^2_{ei} m_{\nu_i}|$ is the effective Majorana mass and m_e is the electron mass.

The goal of the experiments is to measure the half-life of $2\beta_{0\nu}$ decay, that is proportional to $T^{0\nu}_{1/2} \propto \sqrt{\frac{M_{det} t_{obs}}{B \Delta E}}$, where M_{det} is the detector mass, t_{obs} is the observation time duration, B is the rate of background events for unit of mass, time and energy and ΔE is the search energy window [11]. Hence, experiments usually measure the energy spectrum and then infer the value of the half-life. As shown in Fig. 1.3, it

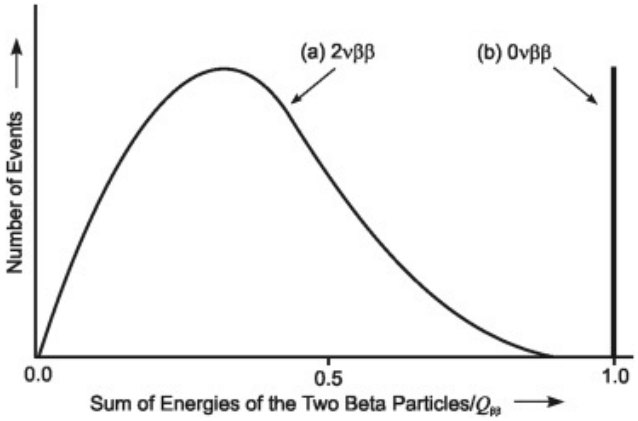

Figure 1.3: Distribution of the sum of the two electron energies for $2\beta_{2\nu}$ and $2\beta_{0\nu}$ decay [18].

has a continuous spectrum for $2\beta_{2\nu}$-decay and a value equal to Q-value in case of $2\beta_{0\nu}$-decay. Moreover, the experiments need a large mass, the best possible energy resolution and an extremely low background. The chosen isotopes are usually the ones for which the single β-decay is forbidden or strongly suppressed. Only 36 nuclei that can undergo double β decay are known, that are reported in [12]. There are typically two types of $2\beta_{0\nu}$ experiments: those in which the source is inserted as thin foil inside a tracking detector, such as NEMO3 [13], and experiments where the detector itself is the source, such as CUORE [14], HdM [15] and GERDA [16]. The problems of the first kind of experiments are the limitation of source material and the limited energy resolution. Up to now, no experiment claimed the observation of a clear signal of this decay. The GERDA experiment obtained a lower bound on the half-life of $2\beta^-_{0\nu}$ decay, that is $T^{0\nu}_{1/2}(^{76}\mathrm{Ge}) > 1.8 \times 10^{26}$ y at 90% C.L. that corresponds to an effective neutrino mass $m_{\beta\beta} < (0.06 - 0.16)$ eV. [17]

Cosmological constraints

Cosmology experiments give the strongest constraints on the value of neutrino mass. They are based on the ΛCDM model (the Standard Model of Cosmology), that assumes the existence of hot relic neutrinos as products of the Big Bang [7].

A way to get a constraint is through imposing a limit on the fraction of the energy-density of the Universe in the form of massive neutrinos, that is:

$$\Omega_\nu = \frac{\rho_\nu}{\rho_c} = \frac{\sum_i m_i}{93.14h^2 \text{ eV}} \tag{1.11}$$

Since matter should not be so heavy to overclose the Universe, the neutrino's energy-density fraction must be $\Omega_\nu < 1$. This condition leads to a powerful bound on the sum of neutrino masses. An analysis of WMAP data on the matter present in the Universe leads to [7]:

$$\Omega_\nu h^2 < \Omega_M h^2 \simeq 0.14 \Longrightarrow \sum_i m_i < 13 \text{ eV}. \tag{1.12}$$

Another way to put an upper bound on the neutrino mass is by studying their effects on the cosmological structures' formation. These structures are generated by

the growth of perturbations of the dark matter density, under gravitational effect. If fluctuations overcome a threshold, gravitation wells are able to trap the matter. Hence, Cold Dark Matter (CDM) falls inside these wells, contributing to their growth and yield to galaxies and clusters formation. Hot Dark Matter (HDM), instead, is too fast to be captured by these wells, hence the small structures are suppressed in favour of larger structures, that can trap the hot DM. Neutrinos, that decoupled in the early Universe when they were relativistic, behave as hot dark matter, thus suppressing the growth of structures at small scales. A recent analysis that used data from Planck, BOSS experiment, Pantheon sample and CMB lensing reconstruction power spectrum [19] reached an upper bound on neutrino mass of $\sum_i m_i < 0.087$ eV.

Future experiments, such as CMB-S4 [20], will determine if the neutrino mass is non-null at 3σ level, being sensitive to $\sum_i m_i > 2 \times 10^{-1}$ eV.

1.3 Neutrino mixing and oscillation

The neutrino mixing comes straight forward from the massive neutrinos [7]. In fact, we can think of the neutrino flavours as a mixing of three mass eigenstates. Getting back to the Eq. 1.1, the leptonic weak charged current is:

$$j^{\rho\dagger}_{W,L} = 2 \sum_{\alpha=e,\mu,\tau} \bar{l}'_{\alpha L} \gamma^\rho \nu'_{\alpha L} = 2 \bar{\boldsymbol{l}}'_L \gamma^\rho \boldsymbol{\nu}'_L \tag{1.13}$$

We can rearrange the current through a unitary matrix V, and so it becomes:

$$j^{\rho\dagger}_{W,L} = 2 \bar{\boldsymbol{l}}_L V_L^{l\dagger} \gamma^\rho V_L^\nu \boldsymbol{\nu}_L = 2 \bar{\boldsymbol{l}}_L \gamma^\rho U \boldsymbol{n}_L = 2 \sum_{\alpha=e,\mu,\tau} \sum_{k=1}^{3} \bar{l}_{\alpha L} \gamma^\rho U_{\alpha k} \nu_{kL} \tag{1.14}$$

with $U = V_L^{l\dagger} V_L^\nu$. This is the Pontecorvo-Maki-Nakagawa-Sakata (PMNS) matrix, that "matches" neutrinos in mass basis with neutrinos in flavour basis. It has 9 parameters (3 angles and 6 phases), that can be reduced into 4 (3 angles, $\theta_{12}, \theta_{13}, \theta_{23}$, and one phase, δ_{13}), so usually it's represented as:

$$U = \begin{pmatrix} 1 & 0 & 0 \\ 0 & c_{23} & s_{23} \\ 0 & -s_{23} & c_{23} \end{pmatrix} \begin{pmatrix} c_{13} & 0 & s_{13} e^{-i\delta_{13}} \\ 0 & 1 & 0 \\ -s_{13} e^{i\delta_{13}} & 0 & c_{13} \end{pmatrix} \begin{pmatrix} c_{12} & s_{12} & 0 \\ -s_{12} & c_{12} & 0 \\ 0 & 0 & 1 \end{pmatrix}$$

where $c_{ij} = \cos\theta_{ij}$ and $s_{ij} = \sin\theta_{ij}$, with $0 < \theta_{ij} < \pi/2$ and $0 < \delta_{13} < 2\pi$.

1.3.1 Oscillations in vacuum

The U_{PMNS} matrix plays a fundamental role in the description of the neutrino oscillations in vacuum. Indeed, a neutrino of flavour α with momentum $\vec{p}$ is described by the flavour state:

$$|\nu_\alpha\rangle = \sum_{k=1}^{3} U^*_{\alpha k} |\nu_k\rangle \,, \tag{1.15}$$

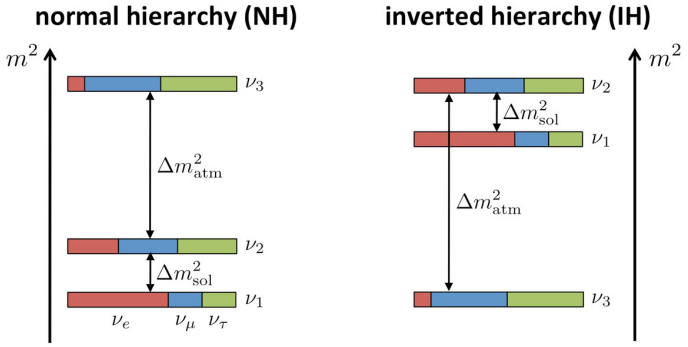

Figure 1.4: Representation of the two possible mass orderings with flavour content of each mass eigenstate.

expression allowed thanks to Eq. 1.14. A given mass eigenstate $|\nu_k\rangle$ propagates in time as plane waves:

$$|\nu_k(t)\rangle = e^{-iE_k t}\,|\nu_k\rangle \tag{1.16}$$

So, combining Eqs. 1.15 and 1.16, a neutrino $|\nu_\alpha\rangle$ at a time t can be described as:

$$|\nu_\alpha(t)\rangle = \sum_{k=1}^{3} U^*_{\alpha k} e^{-iE_k t}\,|\nu_k\rangle \tag{1.17}$$

Since a flavour eigenstate can be considered a linear combination of mass eigenstates, there is a non-null probability that a neutrino α during its propagation changes to a flavour β. This probability is:

$$P_{\nu_\alpha\to\nu_\beta}(t) = |\,\langle\nu_\beta|\nu_\alpha(t)\rangle\,|^2 = \sum_{kj} U^*_{\alpha k}U_{\beta k}U_{\alpha j}U^*_{\beta j}\exp(-i(E_k - E_j)t) \tag{1.18}$$

In the relativistic limit, $E_k \simeq E + \frac{m_k^2}{2E}$, hence $E_k - Ej \simeq \frac{\Delta m^2_{kj}}{2E}$, where $\Delta m^2_{kj} = m^2_k - m^2_j$. So, the probability can be approximated as:

$$P_{\nu_\alpha\to\nu_\beta}(L,E) \simeq \sum_{kj} U^*_{\alpha k}U_{\beta k}U_{\alpha j}U^*_{\beta j}\exp\left(-i\frac{\Delta m^2_{kj}L}{2E}\right). \tag{1.19}$$

Here we have substituted the time of flight t with L, the distance between the source and the detector, since it is a known quantity, being neutrinos relativistic particles. For what concern the squared mass difference, we have Δm^2_{21} called "solar mass splitting" and $\Delta m^2_{31} = \Delta m^2_{32} + \Delta m^2_{21}$, called "atmospheric mass splitting". Given these differences, we have two possible ways to order 3 neutrinos: *normal ordering* (NO), where $m_1 < m_2 < m_3$ and *inverted ordering* (IO), where $m_3 < m_1 < m_2$, as shown in Fig. 1.4.

Historically, the oscillation was analyzed between two states and without considering CP violation. In this approximation, the mixing depends only on one parameter θ and the probability can be expressed as:

$$P_{\nu_\alpha \to \nu_\beta} = \delta_{\alpha\beta} - (2\delta_{\alpha\beta} - 1) \sin^2 2\theta \sin^2 \frac{\Delta m^2 L}{4E} \tag{1.20}$$

From this Eq. 1.20, comes straightforward that, in an ideal experiment, it is possible to play with L and E in order to tune the oscillation probability of neutrinos for our purpose, changing the length of neutrinos' path or their energy production. Furthermore, the mass difference appears squared, and this doesn't allow us to know the mass ordering from the oscillation probability.

It must be noted that the plane-wave treatment is an approximation. In fact, since a plane wave has a definite momentum $\vec{p}$, its position is undefined due to the Heisenberg principle $\Delta x \Delta p \geq \hbar/2$. However, to determine the overall distance L it is crucial to know where the neutrino is produced and where is detected. Hence, to describe a real localized particle the wave-packet treatment is used. In this picture, each mass eigenstate is described by a wave packet that can have a different mass. So, different mass eigenstates produced at the same instant will arrive at separate times, depending on their individual speeds, impeding the oscillation phenomenon. For example, for accelerator neutrinos with an energy of 1 GeV the separation occurs in 10^{20} km, much higher than the distances considered in the accelerator experiments, therefore this separation can be disregarded. Instead, for a supernova neutrino, with energy of 10 MeV, the separation occurs over a distance of 10^3 km, and neutrinos arrive with a time difference of 10^{-4} s.

1.3.2 Matter effects

During the propagation of neutrinos in matter, effective potentials coming from the coherent interactions with the medium, shown in Fig. 1.5, must be taken into account. In particular, electron neutrinos can experience extra charged current interactions due to the presence of electrons in standard matter. Incoherent scatterings with particles are also present, but are extremely rare and can be neglected [7]. This phenomenon was predicted by Wolfenstein, Mikheev and Smirnov and is known as *MSW effect*. They predicted that flavour transitions are possible when neutrinos propagate in a medium with variable density, even with a small vacuum mixing angle, and that there is a region in which the effective mixing angle is at its maximum value of $\pi/4$.

Considering a constant matter density, and including the effects of V_{CC} and V_{NC}, the transition probability of Eq. 1.20, in the case of ν_e and ν_μ, changes to:

$$P_{\nu_e \to \nu_\mu}(x) = \sin^2 2\theta_M \sin^2 \frac{\Delta m_M^2 x}{4E} \tag{1.21}$$

where x is the propagation length,

$$\Delta m_M^2 = \Delta m^2 \sqrt{\sin^2(2\theta) + (\cos 2\theta - \zeta)^2}, \tag{1.22}$$

$$\sin^2 2\theta_M = \frac{\sin^2 2\theta}{(\sin^2 2\theta + (\cos 2\theta - \zeta)^2}, \tag{1.23}$$

and

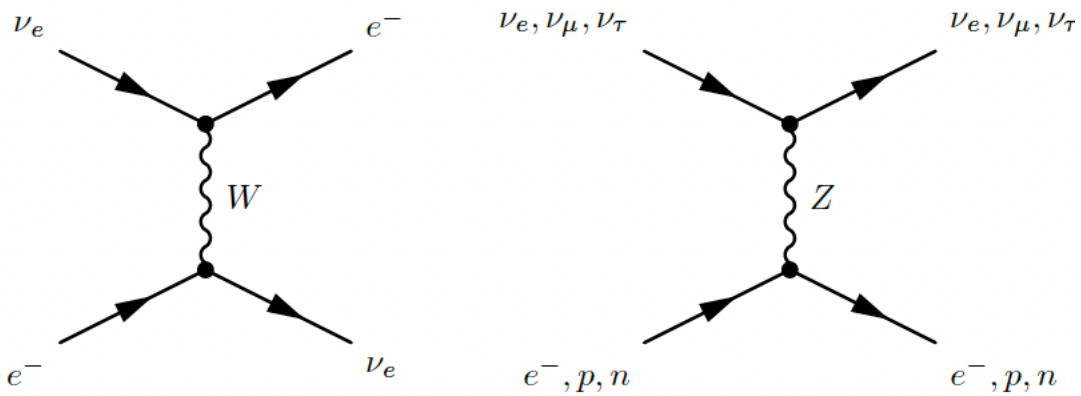

Figure 1.5: Feynman diagrams of coherent elastic scattering processes, responsible of the CC potential (V_{CC}) and the NC potential (V_{NC}) through W and Z exchange respectively.

$$\zeta = \frac{2\sqrt{2}G_F N_e E}{\Delta m^2}, \tag{1.24}$$

with N_e electron density, E energy and G_F Fermi coupling constant. From Eq. 1.23 follows that exists a value of electron density N_e for which ζ equals $\cos 2\theta$, leading to $\sin^2 2\theta_M = 1$. This means that even if the vacuum mixing angle is very small, for a certain density, the matter mixing angle θ_M is maximal.

Moreover, the sign of ζ can give information about the mass ordering of neutrinos. In fact, ζ is related to Δm^2 and in Eq. 1.23 it is not squared, so it preserves the sign of the mass difference. This is one of the most important features of this phenomenon, which is not present in the vacuum oscillation formula, where the sine is squared and cannot give any information about the mass ordering. Lastly, it can be observed that, if Δm^2 or θ are null, also the mixing angle in matter is null, so vacuum oscillation is necessary to have oscillation in matter; if there is no matter, ζ vanishes returning to the vacuum case [7].

1.4 Measurements of oscillation parameters

Neutrinos originate from several sources, such as the Sun and cosmic ray interactions with the atmosphere. They can also be produced by nuclear reactors and accelerators. These sources vary in terms of the distance L from the detection point and for the energy E of the produced neutrinos, thus leading to different accessible Δm^2 values. Over the years, various experiments have been built to study neutrino properties. These experiments can be based on two different modes of observation:

- **Appearance mode**: given a source of ν_α, the goal is to detect a different flavour at a distance L from the source, with a probability $P_{\nu_\alpha \to \nu_\beta}$, according to Eq. 1.20. In this case, the final flavour in the initial beam is either absent or present as contamination. Hence, the background can be quite small and so this mode can be used for the measurement of small mixing angles.

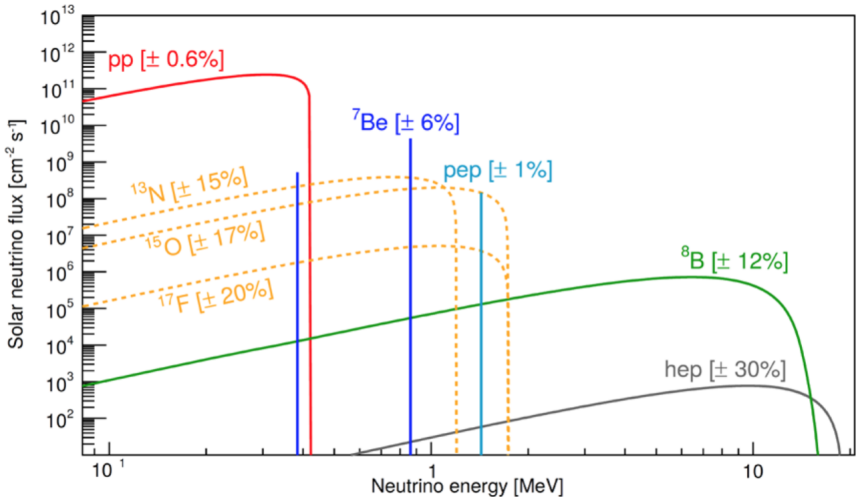

Figure 1.6: Spectrum of solar neutrino fluxes predicted by the SSM [21].

- **Disappearance mode**: given a source of ν_α, the goal is to measure ν_α flux at a distance L from the source, with the "survival" probability $P_{\nu_\alpha \to \nu_\alpha}$, according to:

$$P_{\nu_\alpha \to \nu_\alpha} = 1 - \sum_{\beta \neq \alpha} P_{\nu_\alpha \to \nu_\beta} \tag{1.25}$$

  In this case, the measurement is based on a comparison of the initial and final interaction rates. The disappearance mode is not suitable for measuring small mixing angles because small disappearances are not easily detected due to statistical fluctuations.

For long-baseline experiments, two main detectors are tipically constructed: a near detector that measures the neutrino flux close to the source and monitors the beam, and a larger far detector that measures the flux after a distance L. Both detector have usually the same technology, to reduce the systematic uncertainties.

1.4.1 Solar neutrinos experiments

Solar neutrinos come from processes inside the Sun. In the solar core, thermonuclear fusion reactions occur, producing electron neutrinos with energy of the order of 1 MeV [7]. According to the Solar Standard Model (SSM), the neutrino flux is made of many components that come from various reactions, as shown in Fig. 1.6. Neutrinos cross the solar inner matter and then pass through the space, arriving on Earth with a flux of $\sim 6 \times 10^{10}$ cm^{-2}s^{-1}. However, the detection of these neutrinos is difficult, mainly because of their very small cross section ($\mathcal{O}(10^{-43})$ cm^2). For this reason solar neutrino experiments usually are designed as large detectors, placed underground to avoid the huge background given by cosmic rays.

The first solar experiment built was the Homestake experiment, in 1968. It was a radiochemical experiment, that detected ν_e through the inverse β-decay reaction $\nu_e + {}^{37}\mathrm{Cl} \to {}^{37}\mathrm{Ar} + e^-$. It had an energy threshold of $E_{thr} = 800$ keV, being sensitive to ^{8}B and ^{7}Be neutrino sources. It ran from 1970 to 1994 and observed about 1/3

of the solar neutrinos predicted by the SSM [4]. The scientific community proposed three possibilities to explain this deviation: the Standard Solar Model was wrong; the experiment was not well-calibrated; there was some phenomenon that was being neglected and it could be responsible of this deficit.

In the 1990s other experiments such as GALLEX/GNO [22] and SAGE [23] were built. They lowered the neutrino energy threshold at $E_{thr} = 233$ keV using the reaction $\nu_e + {}^{71}\mathrm{Ga} \rightarrow {}^{71}\mathrm{Ge} + e^-$. From their results, a deficit of 1/2 from the predictions was confirmed.

Meanwhile, a new kind of detector was developed: the water Cherenkov detectors. They are water-filled detectors that exploit the Cherenkov radiation to detect neutrinos. Their main advantage is their sensitivity to all the three flavours of neutrinos and to the directionality of the radiation. Construction of the Kamiokande experiment began in 1983 [24]. The detector consisted of a 3 kton water-filled tank, with an energy threshold of $E_{thr} = 6.5$ MeV. It detected solar neutrinos from ${}^8\mathrm{B}$ that undergo elastic scattering. Then, it was improved with the construction of Super-Kamiokande, filled with 50 kton of water. Both these experiments measured again a deviation from the SSM predictions, with a deficit of $\sim 1/2$.

Pontecorvo already proposed in 1957 that neutrinos could oscillate between the three flavours. Actually, this could be a possible explanation of this observation but these experiments were only sensitive to CC interactions, they could not test this hypothesis. A new experiment that could measure also the neutral current interactions was necessary.

The SNO experiment was built in 1999. Its goal was to compare the observed deficit with the amount of neutrinos of the other flavours. In its final version, it consisted of a giant bath filled with 1 kton of D_2O and equipped with 9600 photosensors. The detection technique was based on the following reactions: $\nu_e + d \rightarrow p + p + e^-$ (CC), sensitive to electron neutrinos; $\nu_\alpha + d \rightarrow p + n + \nu_\alpha$ (NC) and $\nu_\alpha + e^- \rightarrow \nu_\alpha + e^-$ (ES) sensitive to all the three flavours. In 2003, definitive results were published: they confirmed that only 1/3 of solar neutrinos were electronic, while the remaining 2/3 were muonic and tauonic, indicating that electronic neutrinos converted into another flavour [5]. This is shown in Fig. 1.7.

The oscillation phenomenon related to solar neutrinos is governed by two parameters: θ_{12} and Δm^2_{12}. From these experiments, an allowed region of values for these parameters was determined, as shown in Tab. 1.1.

Data combination	$\tan^2\theta_{12}$	$\Delta m^2_{21}(\mathrm{eV}^2)$
Solar experiments [5]	$0.427^{+0.028}_{-0.028}$	$5.13^{+1.29}_{-0.96} \times 10^{-5}$
KamLAND [25]	$0.481^{+0.092}_{-0.080}$	$7.54^{+0.19}_{-0.18} \times 10^{-5}$
Solar + KamLAND [26]	$0.427^{+0.027}_{-0.024}$	$7.46^{+0.20}_{-0.19} \times 10^{-5}$

Table 1.1: Values of parameters obtained using data from solar experiments, from KamLAND and from a combination of them.

1.4.2 Reactor experiments

Nuclear reactors are sources of $\overline{\nu}_e$, that are produced in β-decays. The nuclei most commonly used in nuclear reactors are ${}^{235}\mathrm{U}$, ${}^{238}\mathrm{U}$, ${}^{239}\mathrm{Pu}$ and ${}^{241}\mathrm{Pu}$. The production

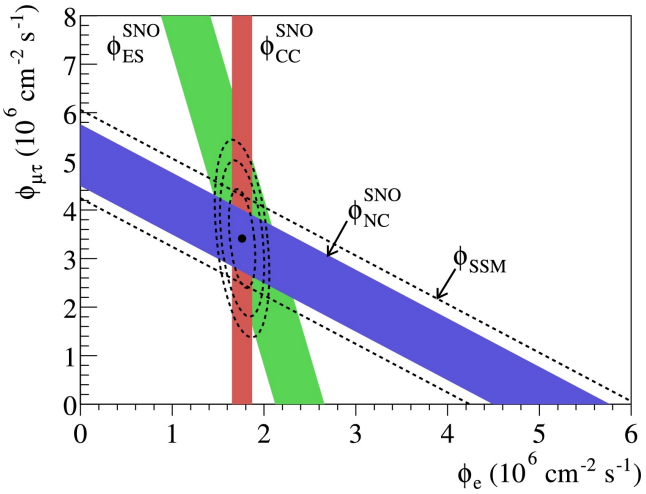

Figure 1.7: Flux of ^{8}B solar ν_μ or ν_τ ($\Phi_{\mu\tau}$) versus flux of ν_e (Φ_e). It shows the consistency between the total flux (blue band) with the prediction of the SSM (band between the dashed lines) [5].

of antineutrinos is isotropic, then the flux decreases with the distance from the source. The neutrino production rate and the spectrum can be estimated from the thermal power and fuel composition as a function of time. The detection technique, in reactor experiments, is based on the inverse β-decay: $\overline{\nu}_e + p \rightarrow e^+ + n$. From this reaction two scintillation signals are observed: a prompt one, from the annihilation of the positron with an electron, and a delayed one, of 2.2 MeV, produced ~ 200 μs later, due to the neutron capture and the subsequent de-excitation of the nucleus.

The KamLAND experiment started the operations in 2002, exploiting the neutrino flux produced by 53 commercial nuclear reactors, located on average 180-km away from the detector [25]. The detector was made of 1 kton of ultra-pure liquid scintillator, which acted as the neutrino target and was contained in a spherical balloon of 13-m-diameter. The average energy of the $\overline{\nu}_e$ spectrum was $\langle E_\nu \rangle \simeq 3.6$ MeV, that is the same energy region of solar neutrinos. KamLAND [25] showed the $\overline{\nu}_e$ disappearance at 99.95% confidence level and determined the oscillation parameters presented in Tab. 1.1. Furthermore, reactor experiments have a good energy resolution but low event statistics, while solar experiments have high statistics and a low energy resolution. Hence, a combined analysis is possible: using the data of KamLAND and of solar neutrino experiments, the allowed region for the values Δm^2_{12} and $\sin^2\theta_{12}$ was constrained, as reported in Fig. 1.8.

Other nuclear reactor experiments such as Daya-Bay, RENO, Double Chooz have been built to study the value of $\sin^2\theta_{13}$ from the $\overline{\nu}_e$ disappearance. They showed a non-zero value for this parameter and Daya-Bay, in particular, measured a value of $\sin^2 2\theta_{13} = 0.0851 \pm 0.0024$ [27].

1.4.3 Atmospheric neutrino experiments

Atmospheric neutrinos are produced from the interaction of primary cosmic rays (CRs) with the nuclei in the atmosphere [7]. The principal components of CRs are protons, that produce secondary CRs when interacting with nuclei. These secondary CRs include hadrons, in particular many pions, and their decay products, which

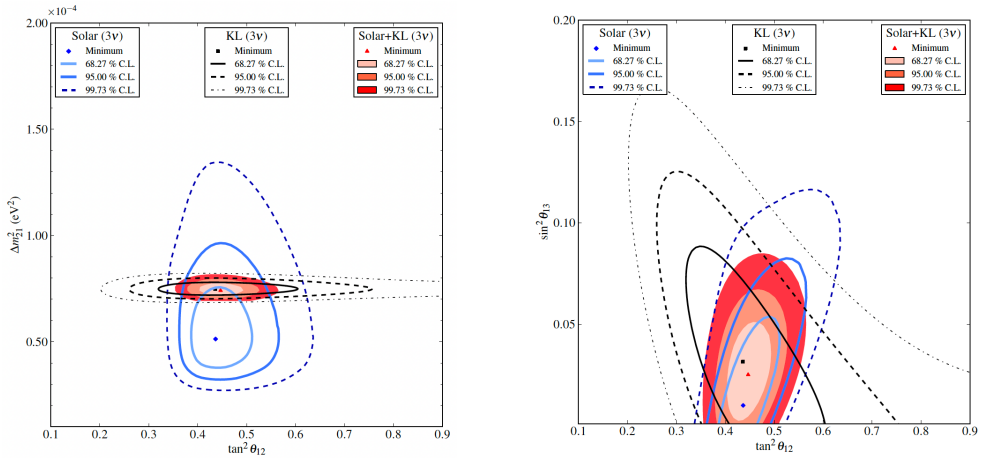

(a) (b)

Figure 1.8: Three-flavour neutrino oscillation analysis contour using both solar and KamLAND (KL) data [26].

tipically have energy of the order of GeV. The reaction chain is the following (Eqs. 1.26, 1.27, 1.28):

$$p + N \rightarrow \pi^{\pm}, \pi^0, K^{\pm}, K^0, p, n, ... \tag{1.26}$$

where N is a generic nucleus of the atmosphere. Then, pions and, at high energies, also kaons, decay into muons and muon neutrinos:

$$\pi^+ \rightarrow \mu^+ + \nu_\mu, \pi^- \rightarrow \mu^- + \overline{\nu}_\mu \tag{1.27}$$

At last, low-energy muons decay before reaching the ground, producing an electron, an electron neutrino and a muon neutrino:

$$\mu^+ \rightarrow e^+ + \nu_e + \overline{\nu}_\mu, \mu^- \rightarrow e^- + \overline{\nu}_e + \nu_\mu. \tag{1.28}$$

The typical experiments that detect atmospheric neutrinos utilizes Cherenkov underground detectors. In fact, being shielded from the large background given by the secondary CRs is fundamental.

In 1980s, atmospheric neutrinos were observed by Kamiokande and IMB, two large underground water Cherenkov detectors. These experiments could detect either neutrinos that interacted within the detector, either upward- or downward-going muons produced by the neutrino interactions outside the tank. The results of both experiments showed a significant deficit in the number of atmospheric muon neutrino interactions, claiming for the first time the *atmospheric neutrino anomaly*. The successor of Kamiokande, Super-Kamiokande (SK), revealed the solution assuming muon neutrinos oscillations. This is clearly shown in Fig. 1.9: they present an up-down asymmetry, showing that data are in agreement with the oscillation hypothesis.

The SK experiment collected a significant amount of data on atmospheric neutrinos over the years, giving a great boost to model the atmospheric neutrino oscillations from muon to tau neutrinos, and to infer their parameters: Δm^2_{32} and $\sin^2\theta_{23}$. Other experiments such as MACRO and Soudan 2, confirmed these results.

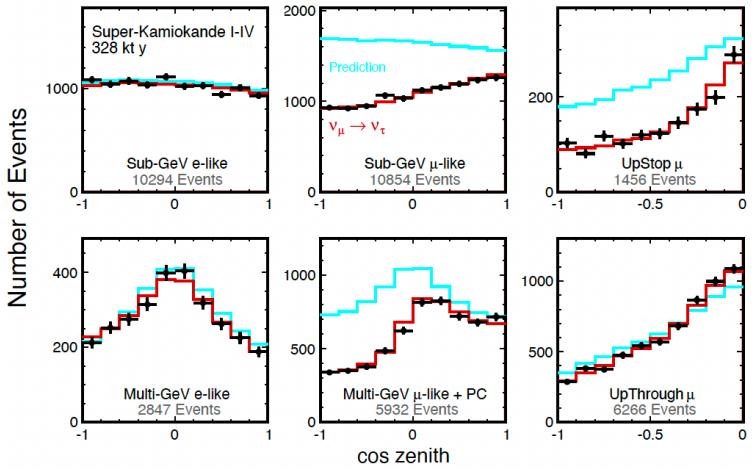

Figure 1.9: Super-Kamiokande plots: black dots are the experimental data, red and light-blue solid lines are MC predictions, assuming oscillation and no-oscillation hypothesis, respectively [28].

1.4.4 Accelerator experiments

Accelerator experiments were built to verify the results of atmospheric neutrino experiments, using a similar L/E ratio.

A conventional neutrino beam is produced by sending high-energy protons towards a target. The interaction produces hadrons, mainly pions and kaons, which are focused into a beam by magnetic horns. These horns can be controlled to choose the operating mode of the beam, i.e. neutrino or antineutrino mode. Then, in the decay pipe, they decay into neutrinos. The remaining hadrons and muons are absorbed and stopped, leaving only neutrinos inside the beam. Actually, the beam can be contaminated. Considering a ν_μ beam, the larger amount of neutrinos comes from pion decay as shown in Eq. 1.27, but from the subsequent decay of muons (Eq. 1.28), from $\pi^+ \rightarrow e^+\nu_e$ or $K^+ \rightarrow e^+\pi^0\nu_e$ also electron neutrinos can be produced, that contaminate the beam.

These experiments can reach different sensitivities depending on the value of L/E, which can be modified according to the experiment's goals. Depending on their baseline, the experiments can be categorized as: Long-Baseline (LBL) experiments, which use $\sim$ GeV neutrinos and a baseline of 10^{3-4} m and Short-Baseline (SBL) experiments, which have a baseline of 1 km and can study neutrino oscillations also at 1 eV. Tipically, LBL experiments have two detectors, a near one and a far one. The near detector aims to reduce the systematic uncertainties due to neutrino flux and neutrino interactions with nuclei. It provides data on the beam close to the source, monitors the beam, and gives information on the energy spectrum and cross sections. The far detector measures the flux and the eventual neutrino oscillation after the baseline. Accelerator experiments can also be classified according to energy spectrum of the beam. They can have a wide-band beam, that is, with a wide energy spectrum that can span one or two orders of magnitude, suitable for searching for new oscillation signals in a wide range of Δm^2 values; a narrow-band beam, obtained selecting the momenta of pions and kaons, suitable for precise measurements of Δm^2; "off-axis", with the detector shifted from the beam axis by a small angle.

Numerous experiments have been conducted in the past 25 years. The first LBL experiment was K2K, which sent a neutrino beam for 250 km from the KEK proton synchrotron to the Super-Kamiokande detector. The beam consisted mainly of muons, with an average energy of $\langle E_\nu \rangle \sim 1.3$ GeV. The near detector, a 1 kton water tank, was placed 300 m away from the source. K2K confirmed the results obtained from atmospheric neutrinos observations, showing again a muon deficit.

The OPERA experiment was built at the LNGS and operated until 2012. It exploited the CERN to Gran Sasso (CNGS) muon neutrino beam, with a baseline of 730 km and an average energy of $\langle E_\nu \rangle \sim 17.7$ GeV. The OPERA detector was based on nuclear emulsions and muon spectrometers. It provided significant evidences for $\nu_\mu \to \nu_\tau$ oscillation, detecting precisely the ν_τ appearance in the beam [29].

Roughly in the same years, the MINOS experiment operated. It was a LBL experiment with a 735-km baseline, that ran from Fermilab to the Soudan mine. It used the muon neutrino beam produced with an average energy $\langle E_\nu \rangle \sim 120$ GeV by the Main Injector at Fermilab. The near and the far detectors consisted of iron-scintillator tracking calorimeters with toroidal magnetic fields. MINOS confirmed the observation of the SK experiment and measured the oscillation parameters: Δm^2_{32} and $\sin^2 2\theta_{23}$ [30].

The latest experiments are T2K and NOνA. T2K is a LBL experiment in Japan which started in the last decade. It has a 295-km baseline, stretching from Tokai to Super-Kamiokande. The muon neutrino beam energy spectrum is centered on 600 MeV, to maximize the oscillation probability over its baseline. The near detector complex, which includes an on- and off-axis detector, is located 280 m from the source. The on-axis detector, INGRID, monitors the flux before the oscillations occur.

The off-axis detector consists of a water-scintillator detector to identify π^0s, TPCs for tracking, fine grained detectors to study CC interactions, and an ECAL. It is located at 2.5° to the central direction of the beam as well as SK. T2K in 2011 claimed for the first time the observation of muon to electron neutrino oscillations [31].

The NOνA experiment is an LBL experiment, with an 810-km baseline. The beam, produced at NuMI at Fermilab is sent to Ash River, in Minnesota. The near detector, located 1 km from the source, uses liquid scintillator detectors, as does the far detector, but it also has a module for muon/pion discrimination. Both detectors are located off-axis, precisely 14.6 mrad from the central direction of the beam. It recorded several $\overline{\nu}_\mu \to \overline{\nu}_e$ events that have been analyzed, constraining Δm^2_{32} and $\sin^2 \theta_{23}$ parameters [32]. The off-axis (OA) technique yields an almost monochromatic neutrino flux in a detector that is shifted by an angle from the central direction of the high-intensity wide-band beam, as Fig. 1.10b shows. The OA configuration is based on the dependence of the neutrino energy E on the small off-axis angle θ. With some assumptions, the relation is described by the Eq. 1.29, which shows the monochromatic nature of off-axis the neutrino energy:

$$E \simeq \left(1 - \frac{m_\mu^2}{m_\pi^2}\right) \frac{E_\pi}{1 + \gamma^2 \theta^2} = \left(1 - \frac{m_\mu^2}{m_\pi^2}\right) \frac{E_\pi m_\pi^2}{m_\pi^2 + E_\pi^2 \theta^2} \tag{1.29}$$

For a on-axis detector, with $\theta = 0°$, the neutrino energy E is proportional to the pion energy E_π. As the detector moves off-axis, the dependence of E from E_π

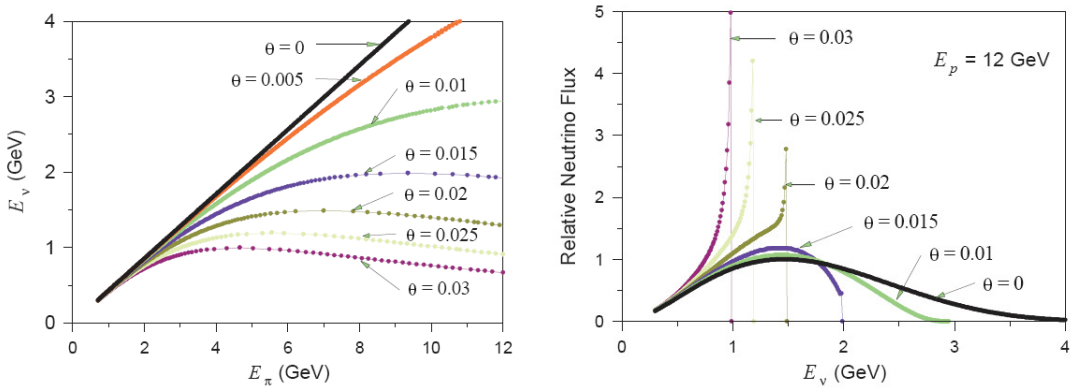

(a) (b)

Figure 1.10: (a): neutrino energy as a function of the parent pion energy. (b): neutrino fluxes integrated over all pion energies produced by a proton beam of 12 GeV. The angle θ is an angle between pion direction and neutrino direction. As the angle increases, the neutrino flux has a more peaked energy [33].

quenches, as can be seen from the plot in Fig. 1.10a.
Future LBL experiments are DUNE, that will be outlined in Chap. 2 and Hyper-Kamiokande, the upgrade of Super-Kamiokande, with a 260-kton total mass.

The other kind of experiments are the SBL ones, where the detector is placed near the neutrino beam source.
LSND was an experiment located at Los Alamos National Laboratory that sent $\overline{\nu}_\mu$ beam to a cylindrical tank detector at 29.8 m from the source. LSND found a evidence for $\overline{\nu}_\mu \to \overline{\nu}_e$ oscillation, observing a $\overline{\nu}_e$ abundance in 2001 [34].
MiniBooNE was a SBL experiment at Fermilab, that operated from 2002 to 2012 with the goal of testing LSND observations. It confirmed LSND results, observing also a $\nu_\mu \to \nu_e$ excess. These are important results because, if confirmed, they require an extension of the 3-ν paradigm to be explained. Future experiments such as JSNS at J-PARC and the Short-Baseline Neutrino (SBN) program at Fermilab will further investigate the anomalies observed in LSND and MiniBooNE. The SBN program includes three experiments based on LAr-TPC technology, with different baselines: SBND at 110 m, MicroBooNE at 470 m and ICARUS at 600 m [35].

1.4.5 Current values of neutrino oscillation parameters

In Tab. 1.2 all current values of the known oscillation parameters are presented. They are obtained from a global fit analysis of all the experiments' results obtained up to now.

The parameters known with the best accuracy are $\theta_{12}, \theta_{13}, \Delta m^2_{21}$ and $|\Delta m^2_{32}|$:

1. θ_{12} and Δm^2_{21} have been determined with a 2% and 3% precision, respectively, by solar and reactor neutrino experiments such as SNO and KamLAND;

2. $\theta_{23}, |\Delta m^2_{32}|$ have been constrained with a precision of 3% and 1% by atmospheric and accelerator neutrino experiments such as SK and T2K or NOνA;

	Parameters	best fit param. $\pm 1\sigma$	3σ
Normal Ordering (NO)	$\theta_{12}/^\circ$	$33.82^{+0.78}_{-0.76}$	$31.61 \to 36.27$
	$\theta_{23}/^\circ$	$48.3^{+1.2}_{-1.9}$	$40.8 \to 51.3$
	$\theta_{13}/^\circ$	$8.61^{+0.13}_{-0.13}$	$8.22 \to 8.99$
	$\delta_{\rm CP}/^\circ$	222^{+38}_{-28}	$141 \to 370$
	$\Delta m^2_{21}/(10^{-5}\ {\rm eV}^2)$	$7.39^{+0.21}_{-0.20}$	$6.79 \to 8.01$
	$\Delta m^2_{32}/(10^{-3}\ {\rm eV}^2)$	$2.449^{+0.032}_{-0.030}$	$2.358 \to 2.544$
Inverted Ordering (IO)	$\theta_{12}/^\circ$	$33.82^{+0.78}_{-0.76}$	$31.61 \to 36.27$
	$\theta_{23}/^\circ$	$48.6^{+1.1}_{-1.5}$	$41.0 \to 51.5$
	$\theta_{13}/^\circ$	$8.65^{+0.13}_{-0.12}$	$8.26 \to 9.02$
	$\delta_{\rm CP}/^\circ$	285^{+24}_{-26}	$205 \to 354$
	$\Delta m^2_{21}/(10^{-5}\ {\rm eV}^2)$	$7.39^{+0.21}_{-0.20}$	$6.79 \to 8.01$
	$\Delta m^2_{32}/(10^{-3}\ {\rm eV}^2)$	$-2.509^{+0.032}_{-0.032}$	$-2.603 \to -2.416$

Table 1.2: Current values of 3-ν oscillation parameters obtained from a global analysis of neutrino data, for both the mass ordering. [2]

3. θ_{13} has been determined with 1.5% precision in reactor experiments, such as DoubleCHOOZ or Daya Bay, and also in accelerator experiments, such as T2K.

However, there are still some open questions. In particular, the unknown sign of Δm^2_{32} leads to two possible mass orderings, as explained in Sec. 1.3.1. Moreover, the octant of θ_{23} is undetermined, since it is unknown if it is smaller or larger than 45° and the leptonic CP phase $\delta_{\rm CP}$ has still large constraints [2].

1.5 Open questions

1.5.1 Mass ordering

Future experiments will focus on three different configurations in order to resolve the mass ordering (Sec. 1.3.1): medium-baseline reactor experiments, looking at the oscillations' interference, such as JUNO [36] or RENO-50 [37]; long-baseline accelerator experiments, such as NOνA or DUNE and atmospheric neutrino experiments, like PINGU [38], ORCA [39], DUNE [40] and HK [41], observing the matter effects.

The reactor experiments are based on $\overline{\nu}_e \to \overline{\nu}_e$ oscillations and study the oscillation interference between Δm^2_{31} and Δm^2_{32}. For the baselines of these experiments, the matter effects are negligible. The oscillation probability can be approximated as:

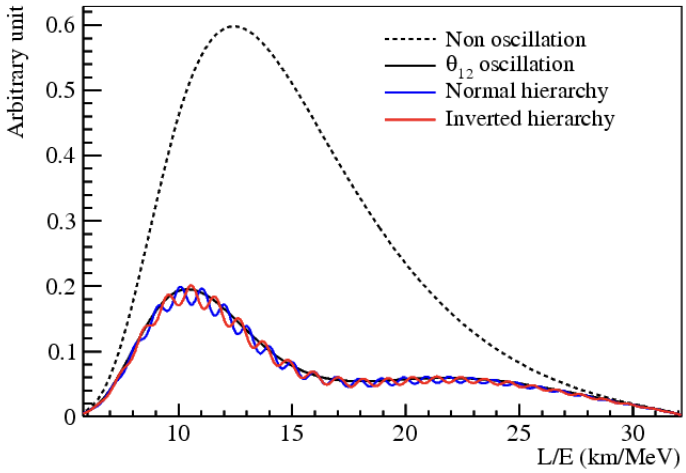

Figure 1.11: The relative shape difference of the reactor antineutrino flux for different neutrino mass hierarchies. The corrections due to the ordering are in phase opposition. The figure represents the product of the neutrino flux, the interaction cross section and the survival probability [36].

$$
\begin{aligned}
P_{\overline{\nu}_e \to \overline{\nu}_e} \simeq\ & 1 - \cos^4\theta_{13}\sin^2 2\theta_{12}\sin^2\left(\frac{\Delta m^2_{21}L}{4E}\right) \\
& - \sin^2 2\theta_{13}\sin^2\left(\frac{\Delta m^2_{31}L}{4E}\right) \\
& - \sin^2\theta_{12}\sin^2 2\theta_{13}\sin^2\left(\frac{\Delta m^2_{21}L}{4E}\right)\cos\left(\frac{2|\Delta m^2_{31}|L}{4E}\right) \\
& \pm \frac{\sin^2\theta_{12}}{2}\sin^2 2\theta_{13}\sin\left(\frac{2\Delta m^2_{21}L}{4E}\right)\sin\left(\frac{2|\Delta m^2_{31}|L}{4E}\right)
\end{aligned}
\tag{1.30}
$$

where the sign of the fourth term depends on the mass ordering. Moreover, this probability does not depend on the CP phase. In order to discriminate between the two mass ordering, a high-resolution energy spectrum is needed, as shown in Fig.1.11. JUNO and RENO-50 reactor experiments will exploit this oscillation channel, using large liquid scintillator detectors and a medium baseline of ~ 50 km.

The other kinds of experiments study $\overset{(-)}{\nu}_\mu \to \overset{(-)}{\nu}_e$ oscillations with long baselines. Their oscillation probability, assuming a constant matter density, is approximated at the second order in the small parameters $\sin\theta_{13}$ and α as:

$$
\begin{aligned}
P_{\overset{(-)}{\nu}_\mu \to \overset{(-)}{\nu}_e} \simeq\ & 4\sin^2\theta_{13}\sin^2\theta_{23}\frac{\sin^2\Delta}{(1-A)^2} \\
& + \alpha^2\sin^2 2\theta_{12}\cos^2\theta_{23}\frac{\sin^2 A\Delta}{A^2} \\
& + 8\alpha J^{max}_{\mathrm{CP}}\cos(\Delta \pm \delta_{\mathrm{CP}})\frac{\sin\Delta A}{A}\frac{\sin\Delta(1-A)}{1-A}
\end{aligned}
\tag{1.31}
$$

where

$$
J^{max}_{\mathrm{CP}} = \cos\theta_{12}\sin\theta_{12}\cos\theta_{23}\sin\theta_{23}\cos^2\theta_{13}\sin\theta_{13}, \tag{1.32}
$$

and

$$\Delta \equiv \frac{\Delta m^2_{31} L}{4E_\nu}, A \equiv \frac{2E_\nu V}{\Delta m^2_{31}}, \alpha = \frac{\Delta m^2_{21}}{\Delta m^2_{31}}, \tag{1.33}$$

with V, effective matter potential of the Earth and $+$ $(-)$ depending on neutrino (antineutrino) channel. In this probability, Δ, A and α are sensitive to the sign of Δm^2_{32} and there is a dependence on the CP phase. For this reason, the results of these experiments can give fundamental information on leptonic CP violation.
Up to now, all analyses show a preference for normal mass ordering, and inverted ordering is disfavoured with a $\Delta\chi^2$ between $2\sigma - 3\sigma$. But more precise measurements are needed to solve the mass quest [2].

1.5.2 θ_{23} octant

The parameter θ_{23} has not been precisely determined yet. In particular, it is unclear if its value is equal, smaller or larger than 45°, as the 3σ-column of Tab. 1.2 shows. This angle can be studied through $\nu_\mu \to \nu_e$ and $\overline{\nu}_\mu \to \overline{\nu}_e$ experiments. In fact, in the disappearance and appearance probabilities, respectively, the θ_{23}-term dominates:

$$P_{\nu_\mu \to \nu_\mu} \simeq 1 - \sin^2 2\theta_{23} \sin^2 \left(\frac{\Delta m^2_{31} L}{4E} \right) \tag{1.34}$$

$$P_{\nu_\mu \to \nu_e} \simeq \sin^2 \theta_{23} \sin^2 2\theta_{13} \sin^2 \left(\frac{\Delta m^2_{31} L}{4E} \right) \tag{1.35}$$

where $\alpha = \Delta m^2_{21}/\Delta m^2_{31} \ll 1/30 \ll 1$ and matter and δ_{CP}-phase terms have been neglected. [42]
If $\theta_{23} \neq \pi/4$, the so-called "octant degeneracy" arises: indeed, a value of θ_{23} either $< 45°$ (first octant) or $> 45°$ (second octant) satisfies

$$\sin^2 \theta_{23} = \frac{1}{2} \left[1 \pm \sqrt{1 - \sin^2 2\theta_{23}} \right]. \tag{1.36}$$

This degeneracy can be solved by combining the results of accelerator and reactor experiments, and also by adding the "silver" channel $\nu_e \to \nu_\tau$ [42]. According to Neutrino2020 updates [43], there is a mild preference for the second octant of θ_{23}, since the $\Delta\chi^2$ minimizes for $\sin^2 \theta_{23} = 0.57$, as shown by Fig. 1.12. Anyway, the local minimum in the first octant occurs at $\Delta\chi^2 = 0.53$ (2.2) without (with) SK-atm data for $\sin^2 \theta_{23} = 0.455$. Hence, the degeneracy is still not solved, since other values of θ_{23}, smaller or equal to $\pi/4$ are consistent at 3σ level [2]. The global fit value will be updated by adding new data from future experiments, such as DUNE or Hyper-Kamiokande.

1.5.3 CP violation

CP violation occurs if the PMNS matrix U is not real, thus $U \neq U^*$. This implies 14 conditions that must be satisfied for CP violation, namely:

- No mass degeneration between charged leptons or neutrinos (6 conditions),

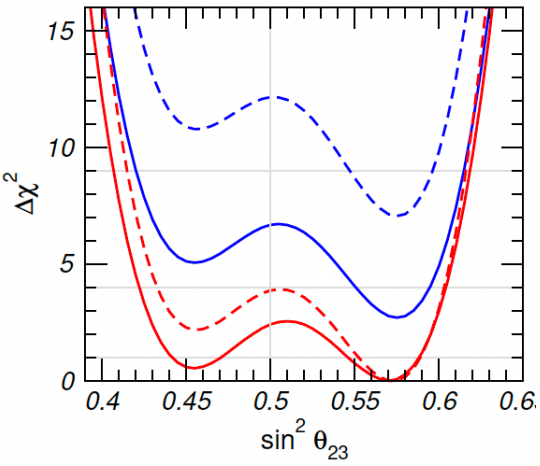

Figure 1.12: $\Delta\chi^2$ profile minimized with respect $\sin^2 2\theta_{23}$. The red (blue) lines correspond to NO (IO); solid (dashed) curves are without (with) SK-atmospheric data [43].

- Mixing angles must be different from 0 or $\pi/2$ (6 conditions),
- The physical phase must be different from 0 or π (2 conditions).

Defining $C = -i[M'^{\nu} M'^{\nu\dagger}, M'^{l} M'^{l\dagger}]$, these conditions can be combined into:

$$\det C \neq 0, \tag{1.37}$$

where $\det C$ can be rewritten as:

$$\det C = -2J(m^2_{\nu_2} - m^2_{\nu_1})(m^2_{\nu_3} - m^2_{\nu_1})(m^2_{\nu_3} - m^2_{\nu_2})(m^2_{\mu} - m^2_{e})(m^2_{\tau} - m^2_{e})(m^2_{\tau} - m^2_{\mu}). \tag{1.38}$$

J is the leptonic analogue to the Jarlskog invariant in the quark sector, which is defined as $J = \mathrm{Im}[U_{e2} U^*_{e3} U^*_{\mu 2} U_{\mu 3}]$. It is useful to quantify CP violation in a parametrization-independent way. In standard parametrization, it becomes

$$J = c_{12} s_{12} c_{23} s_{23} c^2_{13} s_{13} \sin\delta_{13} = \frac{1}{8} \sin 2\theta_{12} \sin 2\theta_{23} \cos\theta_{13} \sin 2\theta_{13} \sin\delta_{13}. \tag{1.39}$$

CP phase δ_{CP} plays an important role in long-baseline accelerator experiments, with $\nu_\mu \to \nu_e$ oscillation. CP violation can be observed only in case of interference between flavour oscillations involving at least two different phases and three mixing angles, since it is a three-flavour effect. To test the presence of CP violation, the behaviour of neutrino and anti-neutrino oscillations is studied, looking for some differences. If $\delta_{\mathrm{CP}} = 0$ or π, there is no CP violation, hence $P_{\nu_\mu \to \nu_e} = P_{\overline{\nu}_\mu \to \overline{\nu}_e}$; if $\delta_{\mathrm{CP}} = -\pi/2$ $(+\pi/2)$, $P_{\nu_\mu \to \nu_e}$ is enhanced (suppressed) and $P_{\overline{\nu}_\mu \to \overline{\nu}_e}$ is suppressed (enhanced). Moreover, matter effects must be considered, since they complicate the measurement.
Although reactor experiments cannot have access to δ_{CP}, they can be used to constrain the CP phase since it is strongly correlated with θ_{13}.

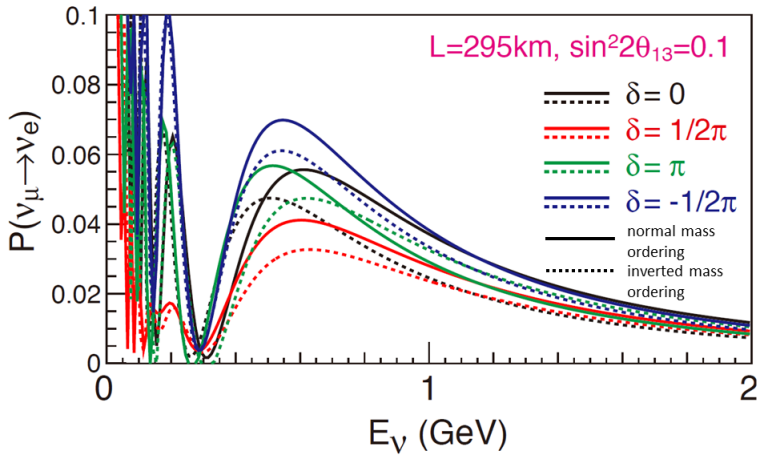

Figure 1.13: $\nu_\mu \to \nu_e$ oscillation probability at T2K as a function of neutrino energy for several values of $\delta_{\rm CP}$ and mass orderings. $\sin^2\theta_{23}$ and $\sin^2\theta_{13}$ are fixed to 0.5 and 0.1 [44].

At present, the main experiments that aim to measure $\delta_{\rm CP}$ are T2K and NOνA, LBL accelerator experiments. From the results obtained by T2K [45], the 3σ C.L. for $\delta_{\rm CP}$ is in the range $[-3.41, -0.03]$ in NO and in the range $[-2.54, -0.32]$ in IO. A NOνA recent analysis [46], excluded at 2σ C.L. values around $\delta_{\rm CP} = -\pi/2$ for the NO, and by $> 3\sigma$ values around $\delta_{\rm CP} = \pi/2$ for the IO. Comparing the best fits of these experiments, it is clear that they agree in the inverted ordering case, but they show tensions in the normal ordering case. This result probably reflects a more pronounced asymmetry in ν_e versus $\overline{\nu}_e$ observed in T2K [46]. NOνA and T2K will operate until 2026, with some upgrades, but they will never have the capability to measure $\delta_{\rm CP}$ with 5σ significance. Hence, future experiments such as DUNE and Hyper-Kamiokande are needed to measure definitely $\delta_{\rm CP}$.

Chapter 2

The DUNE experiment

The Deep Underground Neutrino Experiment (DUNE) will be a long-baseline neutrino oscillation experiment designed to address the unresolved questions about neutrino physics. It will be located in the United States, at the Long Baseline Neutrino Facility (LBNF), which will utilize the neutrino beam produced at Fermilab, in Illinois (Fig. 2.1). DUNE will consist of a Near Detector (ND), located 62 m underground and 574 m away from the target of the primary beam, and a Far Detector (FD), placed 1.5 km underground and 1285 km distant from Fermilab, at the Sanford Underground Research Facility (SURF). [40]

This chapter provides an overview of the DUNE experiment, including its physical motivations. Furthermore, a more precise description of the Far and Near detectors is outlined. The next chapter will present information on the SAND and GRAIN detectors.

2.1 Physical motivations and overview

The primary goals of DUNE, as next-generation long-baseline neutrino experiment, are:

- performing precise measurements of ν_1 - ν_2 and ν_2 - ν_3 oscillations phenomena, neutrino mass ordering, δ_{CP} phase, and test the consistency of the three-flavour paradigm;

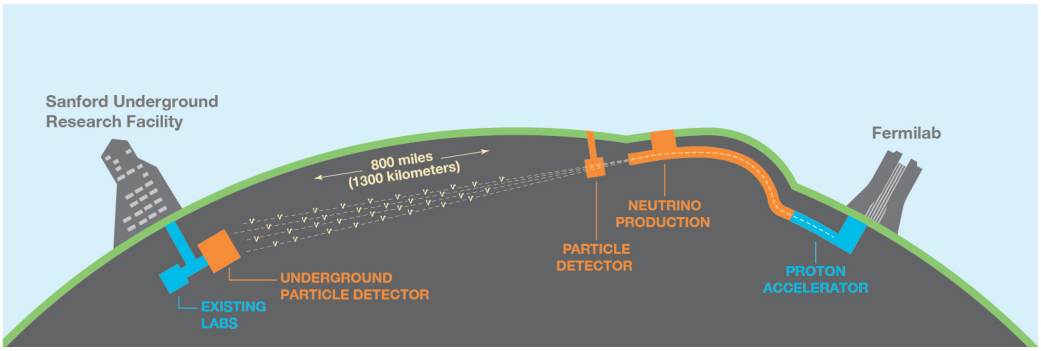

Figure 2.1: Qualitative scheme of LBNF for DUNE experiment. In blue are shown the already present components, in orange, the future ones [47].

- carrying on measurements both in astrophysical and particle physics field, studying low-energy neutrinos and neutrinos from supernova bursts;

- searching for hints of BSM-physics.

Given these premises, the design must satisfy many requirements to accomplish these demanding challenges. First, to precisely study the CP violation and to verify the three-flavour paradigm, neutrinos will be observed over more than one full oscillation period. The beam will be mostly composed of ν_μ, and it will have a peak at about 2.5 GeV, near the oscillation maximum, with significant rate that covers more than one oscillation period for energies between 0.5 and 4.0 GeV, at a fixed baseline of 1300 km. The contamination from the wrong sign of neutrinos will be less than 5%, while the one from electronic neutrinos will be less than 1%.

The Far Detector will be located $\sim$ 1300 km distant from the source. This choice will help in breaking the experimental degeneracy between neutrino mass ordering and the determination of δ_{CP}. The reason is that the asymmetry $P(\nu_\mu \to \nu_e)$ and $P(\bar{\nu}_\mu \to \bar{\nu}_e)$ due to the presence of matter is larger than the one due to the δ_{CP} phase [48][49]. The FD will be located underground to have a very low background from cosmic rays, that arrive with a high rate on the surface. The detector is planned to be a Time Projection Chamber filled with liquid Argon (LAr-TPC). The TPC combines tracking and calorimetry, and is well suited for identifying the different interaction processes that neutrinos undergo. This feature is crucial for an accurate study of neutrino oscillations, which requires an optimal separation of neutrino-charged-current interactions and a good energy reconstruction.

The Near Detector will consist of SAND, ND-LAr and TMS. In Phase II TMS will be replaced by ND-GAr. Thanks to the LAr detector, the experiment will be sensitive to the uncertainties related to flux, cross sections, and detector response, that affect the neutrino energy spectrum at FD. The goal of the ND complex is to measure neutrinos before the oscillation phenomenon and to reduce these systematic uncertainties. In particular, for the latter task, the calibration of position and energy deposits from different sources at a few percent level is essential. Furthermore, since the neutrino cross sections depend on energy, and the fluxes at ND and FD are different, it is important to study the data at different neutrino fluxes. For this reason, the PRISM technique is proposed: it consists in a mechanism that allow ND-LAr and TMS to move off-axis, thus studying neutrino beam at different energies.

A photon detection system that collects prompt scintillation light from charged particles will be implemented inside the LAr-TPCs, to determine the 3-D vertex position with a 1% resolution, in a joint analysis with the TPC. At last, the data acquisition system (receiving, processing, and recording data) will be built according to the needs of supernova burst neutrino detection.

The build schedule of DUNE is planned in two phases, as Table 2.1 shows. Phase I aims to start data-taking by the end of the 2020s with the Far Detector which will equipped with only 2 modules (20 kton of fiducial mass). In 2032 the beam, with 1.2 MW of power, and the Near Detector will become operational. In this phase, the experiment will be able to carry out results such as the determination of the neutrino mass ordering. However, to achieve the precision discussed in the Strategic Plan for U.S. Particle Physics [50] about the neutrino oscillation physics goals, the upgrades of Phase II are also necessary. In this second phase, the far detector will

Parameter	Phase I	Phase II	Impact
FD mass	20 kton fiducial	40 kton fiducial	FD statistic
Beam power	up to 1.2 MW	2.4 MW	FD statistic
ND config	SAND, ND-LAr, TMS	SAND, ND-LAr, ND-GAr	Syst. constraints

Table 2.1: Description of two-stage building program of LBNF and DUNE [40].

be expanded with the addition of two more modules (40 kton of fiducial mass), increasing by a factor of 4 the event rate in the LAr TPCs. Phase-II improvements are fundamental for the achievement of the desired physics goals. In particular, with the experiment at full capacity, the expected sensitivity will be much higher with respect to the Phase-I setup, as the next section will show. This approach will yield some early results but will slow down the construction of later stages.

2.2 Physics sensitivity

In this section, the expected sensitivity of the experiment is presented. An important parameter in this discussion is the "exposure", a quantity related to the detector size, beam power, and time, measured in kton · MW · yr, which refers to the data accumulated. Here, the sensitivity results corresponding to long baseline oscillation, to supernovae, and to BSM are reported, including the Phase-II program upgrades.

2.2.1 Long-baseline neutrino oscillations

The analysis, based on Monte-Carlo (MC) simulations performed on the long-baseline oscillation sensitivity, showed that DUNE can establish the neutrino mass ordering, accurately measure δ_{CP} and carry on precision measurements of the long-baseline oscillation parameters. The importance of the results that DUNE can achieve is confirmed by the plots presented in Fig. 2.2: at the exposure of 1104 kton · MW · yr, the allowed regions for $\sin^2\theta_{13}$, δ_{CP} and for $\sin^2\theta_{13}$, Δm^2_{32} are shrunk, getting closer to the current NuFIT best estimate (true value).

Mass ordering

Two plots are shown in Fig. 2.3: (a) shows the significance for the determination of the neutrino mass ordering as a function of δ_{CP} true values, for two different exposures. The solid lines represent the median sensitivity, and the bands limit the 68% of variations of statistics, systematics, and oscillation parameters. The near-degeneracy between matter and CP violating effects, that occurs close to $\delta_{\mathrm{CP}} = \pi/2$ for normal ordering, gives this characteristic shape to the plot. The plot in (b) relates the significance with the exposure in years, for different values of δ_{CP}. For an exposure of 100 kton · MW · year, DUNE can determine the mass ordering at 5σ for 100% of δ_{CP} values.

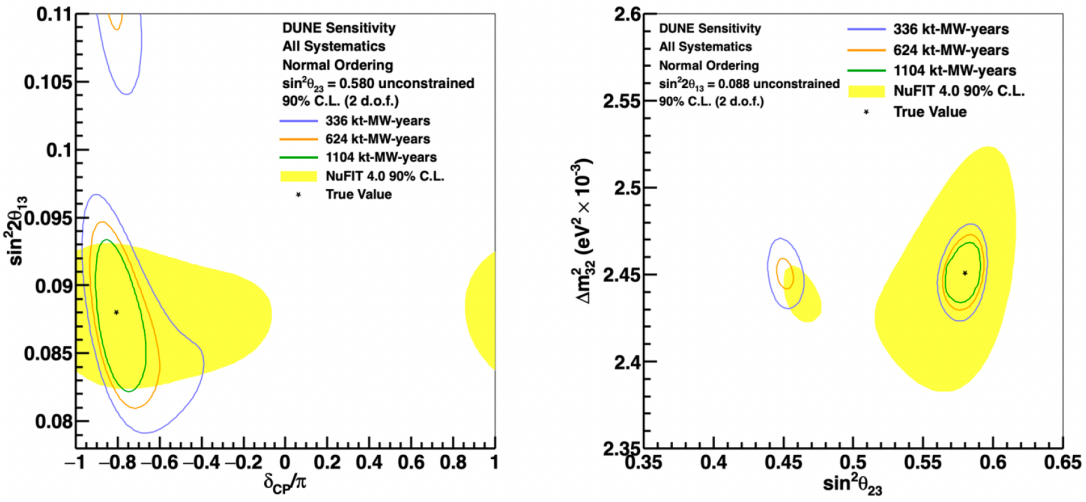

Figure 2.2: Plots representing 90% C.L. regions in the $\sin^2\theta_{13}-\delta_{\mathrm{CP}}$ (a) and $\sin^2\theta_{13}-\Delta m^2_{32}$ (b) planes, obtained with the beam in neutrino and antineutrino mode, in equal amount, and with Phase-II ND. The three colors correspond to different levels of exposure; the yellow area represents the 90% C.L. region for the NuFIT global fit [40].

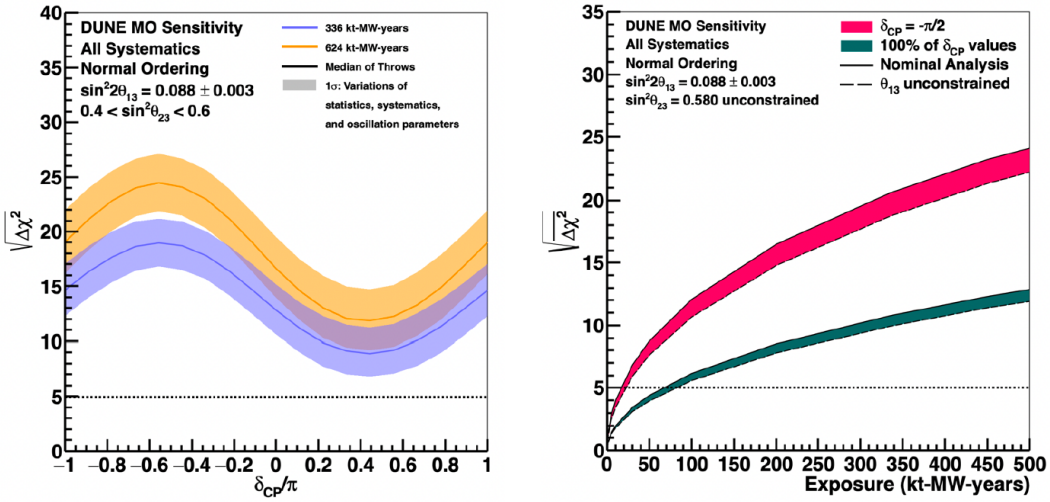

(a) (b)

Figure 2.3: Significance of the DUNE determination of the neutrino mass ordering as a function true values of δ_{CP} (a) and on the exposure (b) [40].

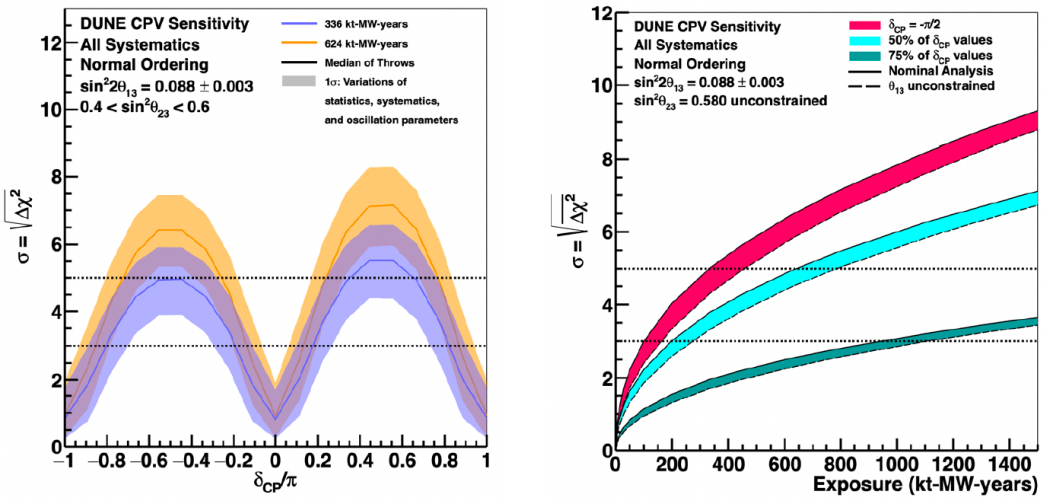

(a) (b)

Figure 2.4: Significance of DUNE determination of CP violation as a function of depending on true values of δ_{CP} (a) and on the exposure (b) [40].

CP violation

The plots in Fig. 2.4 show the expected CP violation significance as a function of δ_{CP} and of exposure.
The plot (a) is obtained assuming normal ordering and considering two different exposures. The solid line represents the median significance, and the bands cover 68% of variations of statistics, systematics and oscillation parameters. Here, the significance is maximal for $\delta_{\text{CP}} = \pi/2$ and, for an exposure of 336 kton $\cdot$ MW $\cdot$ yr, it's above 5σ for few values. In the plot (b), the significance is at 5σ for an exposure of about 300 kton $\cdot$ MW $\cdot$ yr if $\delta_{\text{CP}} = -\pi/2$, and for 600 kton $\cdot$ MW $\cdot$ yr of exposure for 50% of δ_{CP} values. For 75% of δ_{CP} values, the exposure needed for a significance of 3σ is almost 1000 kton $\cdot$ MW $\cdot$ yr.

Oscillation parameters

DUNE will be able to measure all the parameters that describe neutrino oscillations. In particular, it will have sufficient sensitivity to the θ_{23} octant for values of $\sin^2\theta_{23}$ in the range [0.47, 0.55], thus measuring it with at least 1° precision. This can be done through a combined analysis of $\nu_\mu \to \nu_\mu$ and $\nu_\mu \to \nu_e$ channels.

2.2.2 Supernovae and solar neutrinos

DUNE Far Detector can detect neutrinos coming from core-collapse supernovae and from the Sun, that have energies between $\sim$ 5 and 100 MeV.
Core-collapse supernovae occur very rarely in our Galaxy, therefore, it is crucial to gather as much data as possible when they occur. The design of the DUNE FD components will take this into account. The expected energy threshold is a few MeV of deposited energy and the expected energy resolution is 10-20% for these values of energy. The expected event rate for a 40-kton detector is about 3000 neutrinos

for a supernova 10-kpc distant. In this kind of supernovae, the neutrino signal begins with a short and sharp burst made mostly of ν_e, called "neutronization" burst; it is followed by an "accretion" phase, of hundreds of milliseconds and by a "cooling" phase, of about 10 seconds, that is the bulk of the signal, almost equally shared between the three flavours of neutrinos and antineutrinos. So, neutrinos are present in the processes that occur during the supernova evolution, thus the neutrino signal carries information on its source. Hence, a measurement of a supernova neutrino flux gives the chance to, for example: test stellar evolution models; warn the scientific community of the SN explosion, since neutrino burst happens before the electromagnetic signal; reconstruct the source direction.
Solar and background supernova neutrinos aren't easily detectable, but some studies suggest that a selection of a sample of solar neutrinos is possible. This would be very useful for the measurement of Δm^2_{21}.

2.2.3 Beyond Standard Model physics

The deep underground position of the DUNE far detector is a crucial feature in the search for rare processes of Beyond Standard Model physics. Here, some of the BSM phenomena that can be investigated by DUNE are outlined.

Sterile neutrino mixing Some theories hypothesize the existence of sterile states of neutrinos that, mixing with the known active neutrinos, can be responsible for disagreement with the 3-ν paradigm. Therefore, in order to ensure the detection of any potential anomalies, DUNE will be sensitive to a wide range of possible sterile neutrino mass splittings and will search for disappearance of CC and NC neutrino interactions over the long distance between Near and Far Detectors, as well as over the short baseline of the ND. Due to its long baseline, intense beam and large FD, DUNE will provide a greater sensitivity than the existing probes. Moreover, models that include sterile neutrinos, either heavy or light, imply that the 3×3 PMNS matrix is not unitary. This is caused by the presence of sterile neutrinos that mix with active neutrinos, and, if it is of order 10^{-2}, it can be observed by a decreasing in the event rate at DUNE [51].

Non-standard Interactions (NSI) Neutrinos may undergo non-standard interactions (NSI) during their propagation through the Earth. These processes can strongly affect the data to be collected by DUNE, as long as the new physics parameters are large enough. Due to its long baseline and wide-band beam, DUNE will be sensitive to these probes.

CPT violation DUNE can also improve the present limits on Lorentz and CPT violation by several orders of magnitude, testing their validity. For this goal, atmospheric neutrinos are optimal, since the oscillated flux, which consists of all three flavours of neutrinos and antineutrinos, is sensitive to matter effects and to both Δm^2 parameters and covers a wide range of L/E.

Neutrino trident production The electroweak process in which a neutrino scatters off a Coulomb field of a heavy nucleus producing a pair of charged leptons is

called neutrino trident production. In DUNE, due to the high intensity of ν_μ flux at ND, there would be enough production rate to observe events of this kind, giving the possibility to improve the current measurements.

Dark Matter searches DUNE also includes a dark sector-particle program, with a search for Axion-Like particles and Low-mass Dark Matter (LDM). This will be carried out mainly by the ND: the detector complex will be close enough to the beam source to detect a good amount of Dark Matter candidates, assuming they are produced; in addition, the PRISM capability will increase the control of SM neutrino backgrounds. Furthermore, DUNE will have unique sensitivity for the search of Heavy Neutral Leptons (HNL) and Boosted Dark Matter (BDM). In particular, the far detector will be able to detect BDM signals from several sources in the universe.

Baryon number violation and proton decay Some theories beyond the Standard Model, called Grand Unified Theories (GUTs), predict the baryon number violation. Under this assumption, proton decay would be possible. DUNE, thanks to its imaging, calorimetric, and PID capability, is expected to be sensitive to many processes that could be potential candidates for a baryon-number violation. These processes are difficult to reconstruct due to the low energy of the final state and the presence of background. In particular, DUNE will search for two proton decay modes: $p \to e^+\pi^0$ and $p \to K^+\overline{\nu}$. The first has the highest branching ratios among the predicted decays; the second can be exploited particularly in DUNE because stopping kaons have a higher ionization density with respect to lighter particles. Hence, the LAr TPC has to identify a K^+ track efficiently. In case of detection of proton decay, its lifetime value will be measured; in case of no detection in 10 years, instead, a lower limit of $1.3 \cdot 10^{34}$ years will be expected. Considering the total fiducial volume, DUNE will be able to improve the current limits on proton lifetime by an order of magnitude, with 90% C.L., after a 20-year run.

2.3 DUNE design

In this section, the LBNF beam and the detector design are described in detail.

2.3.1 LBNF beam

The Long-Baseline Neutrino Facility provides a neutrino beamline and the necessary conventional facilities to satisfy the DUNE science requirements [52]. The beam will travel for 1300 km from Fermilab to the SURF detectors, located 1.5 km underground. The energy spectrum of the beam must cover the region of the first two oscillation maxima, that are expected to be at 2.4 GeV and 0.8 GeV, for its baseline. The beam components must be sign-selected, to separate neutrino from antineutrino beam, and in particular, the electron neutrino content must be small to reduce systematic errors. Furthermore, the beam must be directed to the far detector with an angular accuracy to allow for the determination of the energy spectrum exploiting the near detector measurements. All of these requirements will be crucial for the determination of the mass hierarchy and the CP phase, and for accurate

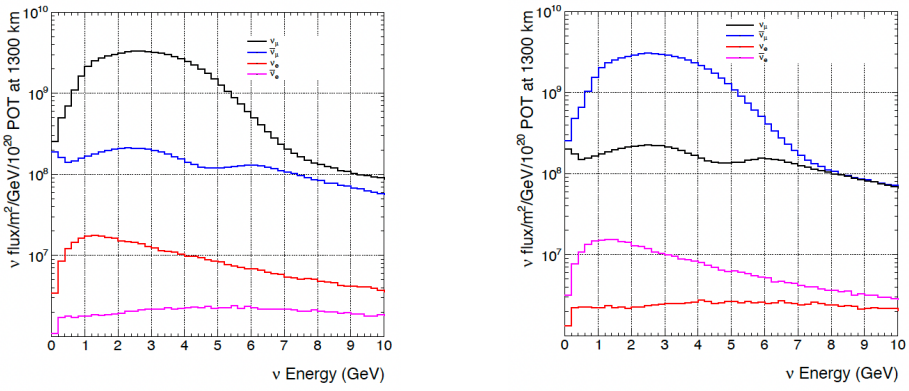

(a) (b)

Figure 2.5: Neutrino fluxes at far detector with the beam in neutrino (a) and antineutrino (b) mode [52].

measurements of the oscillation parameters. Optimization of the beam design can affect in a significant way the exposures needed to reach the desired physics goals, independent of any upgrades to the accelerator.
The LBNF beamline will use the proton beam from the PIP-II upgrade of the Main Injector. It will deliver a proton beam with energy in the range of 60-120 GeV, corresponding to a power of 1.2 MW in Phase I [53]. Future upgrades are already planned, that will enhance the power up to 2.4 MW: for this reason, some components are built taking already into account these improvements. The proton beam will be extracted at MI-10 extraction point, and then it will be bent towards the far detector. Hence, a hadronic shower formed mainly by pions and kaons will be produced upon hitting a graphite-beryllium target. These products then will be focused by horns into a $\sim$ 200 m long decay pipe, where they decay mostly into $\mu^{\pm}$ and $\overset{(-)}{\nu}_{\mu}$. Here, depending on the mesons' sign selection, the beam will run in either neutrino or antineutrino mode. Almost all the muons are stopped by the shielding walls, but some of them decay and contaminate the beam with electron neutrinos. In Fig. 2.5 the expected energy spectrum and the flux composition at the far detector in both running modes are reported. The plots show a clear abundance of the muon neutrino component, as expected.

2.3.2 Far Detector

The Far Detector complex of DUNE will be located at SURF, in South Dakota, 1.5 km underground, as Fig. 2.6 shows. It will consist of four LAr-TPC detectors, each with at least 10 kton of fiducial mass of liquid Argon. These four modules will be placed inside a cryostat of dimensions 15 m $\times$ 14 m $\times$ 62 m, thus containing almost 17.5 kton of total mass [47]. Currently, the choice for the best technology for the detector is under study: the possibilities being considered are single-phase or double-phase detector. The ProtoDUNE program, at CERN, has tested both detector technologies and is still performing studies on these topics. This program exploits prototypes of the future full-scale modules, approximately 1/20 of the size of the final detector but with the same components of the full-scale FD. Data acquisition

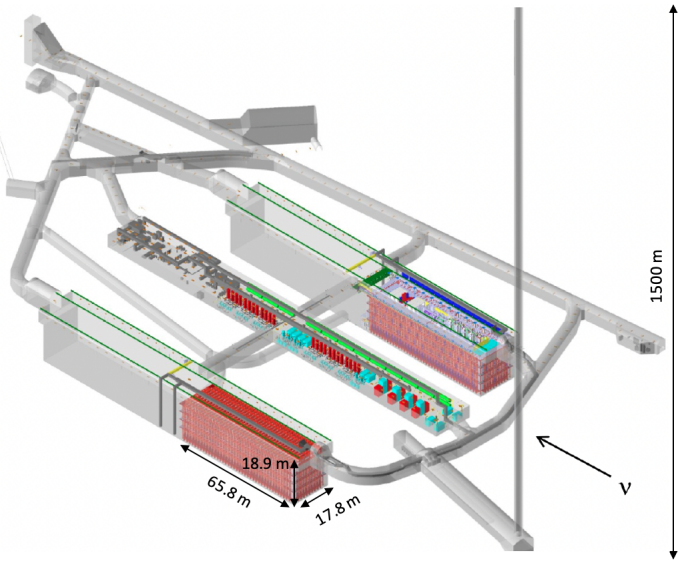

Figure 2.6: Underground caverns for the DUNE FD and cryogenics systems at SURF. The figure shows the first two Far Detector modules in place [47].

began in 2018, with the goals of testing the production and quality of the components, validating the installation procedures, operating with cosmic rays to see its performances, and collecting test beam data to measure the detector response. According to the 2020 Technical Design Report (TDR), only three out of four modules are already planned: in particular, two SP modules and one DP module. Recently, the results of ProtoDUNE changed the strategy, showing a preference for another single-phase module instead of a dual-phase. The current proposal provides an horizontal drift SP TPC for module FD1 and a vertical drift TPC for module FD2. The sequence of installation is FD2 first. In the next paragraphs, the two TPCs will be described.

Horizontal drift LAr TPC

The horizontal drift LAr TPC is a single-phase detector, in which the charged particles, passing through its volume, ionize the argon atoms. The electrons produced from the ionization drift in a horizontal electric field towards the anode planes, in a few milliseconds. The anode planes used are the APAs (Anode Assembly Planes), that are formed by three layers of active wires that form a grid, with the relative voltage between the layers selected. The voltage is chosen such that the first two layers are transparent to the drifting electrons, inducing a bipolar signal, and subsequently these electrons can be collected by the last layer, resulting in a unipolar signal. In this way, the grid provides the reconstruction of two coordinates.
The third coordinate is determined using the drift time, considered as the Δt between the prompt scintillation light and the arrival time of the electrons on the APAs. Liquid Argon is an excellent scintillator since it produces 40k photons per MeV. On the other hand, the scintillation light is VUV region, with a 127 nm wavelength. Hence, it is shifted into visible light, and then collected by photodetectors, providing the start time t_0 for the ionization. The operating scheme of a LAr TPC is reported in Fig. 2.7.

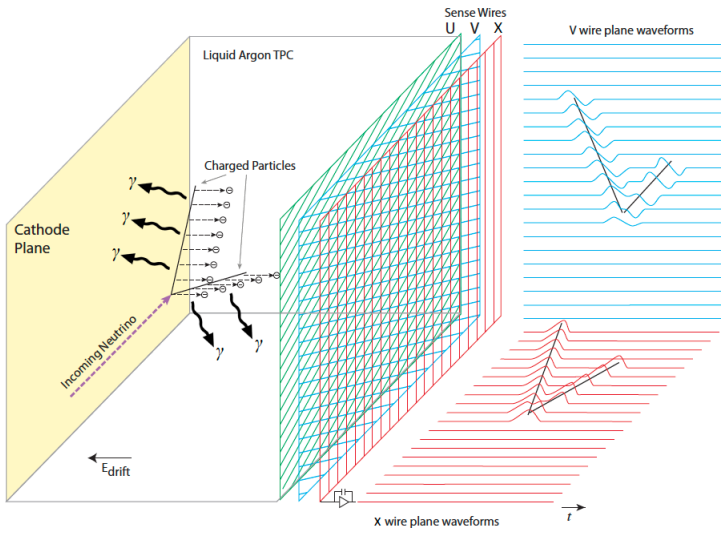

Figure 2.7: General operating principle of a single-phase LAr TPC [47].

In the DUNE experiment, the single-phase LAr TPC will have a mass of 17.5 kton, and it will be located inside a cryostat of 65.8 m × 17.8 m × 18.9 m dimensions. The whole volume is separated with alternating cathode and anode walls. A cathode wall consists of an array of 150 Cathode Plane Assemblies, which are 1.2 m × 4 m panels at -180 kV. An anode wall is formed by 50 APAs, which are modules of 6 m × 2.3 m, connected to the ground. Inside the drift volume, an electric field of 500 V/m is produced, and the maximum drift length is about 3.5 m. The readout cold electronics are placed at the top end of the top APA and at the bottom end of the bottom APA. The design is shown in Fig. 2.8.

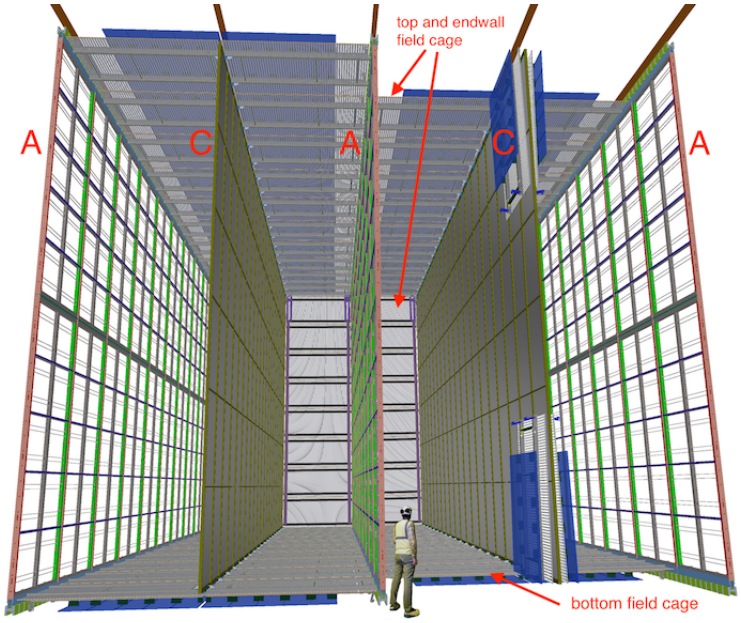

Figure 2.8: DUNE FD single-phase LAr TPC, showing the alternating anode (A) and cathode (C) planes, and the Field Cage that surrounds the drift regions between the planes [47].

The device chosen for the photon detection is the X-ARAPUCA Supercell. The

structure and working principle of a single X-ARAPUCA cell is shown in 2.9. Each photon detection module spans the width of the 2.3 m of the APA and is placed behind the anode wire-planes. For each module there are four X-ARAPUCA Super-cells with VUV light-transparent dichroic filters, alternated with wavelength shifters (WLS) plates to convert UV photons to visible spectrum at 430 nm. The photons emitted by the WLS plates at a smaller angle than the critical one are detected by the SiPM, otherwise, the photons are reflected back towards the WLS plates by the dichroic filters, being collected by the SiPM.

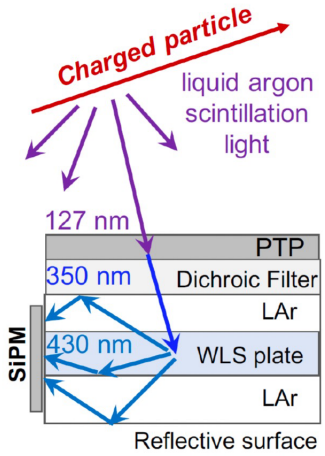

Figure 2.9: Working principle of an X-ARAPUCA cell. The VUV scintillation light emitted by the LAr is shifted to the visibile spectrum by the WLS. The escaping photons are reflected back by the dichroic filters and then collected by the SiPM.

The main drawbacks of the DUNE TPC are the LAr purity and the electronic noise. To mantain LAr purity, it is important to keep low the concentration of electronegative and nitrogen contaminants that, respectively, can absorb ionization electrons and quench scintillation photons. For this reason, the electronegative contaminants concentration must be below 100 ppt O_2 equivalent, such that the ionization electron lifetime is above 3 ms, and the SNR is large enough to perform good measurements. The nitrogen contaminants must be below 25 ppm, to have at least 0.5 photoelectrons per MeV detected. This is achieved through the use of a purification system and low-noise cryogenic electronics, which reduce thermal noise.

Vertical drift LAr TPC

For the second module of the DUNE FD, a vertical drift LAr TPC is proposed based on the results of the ProtoDUNE program carried out at CERN [54]. This detector is a TPC where the ionization electrons drift vertically, for a maximum of 6.5 m, towards anodes located at the top and bottom of the detector. The cathode hangs at mid-height, as shown in Fig. 2.10. It is a thin structure to reduce the loss of active volume and it is also 60% transparent to allow the passage of the Argon. The surrounding field cage ensures an electric field at 500 V/cm. The anode planes, of 60 m $\times$ 13.5 m dimensions, are based on perforated printed circuit boards (PCBs), a technology that avoids significant deformations to the planes, that are hung horizontally. Each anode plane consists of two PCB boards.

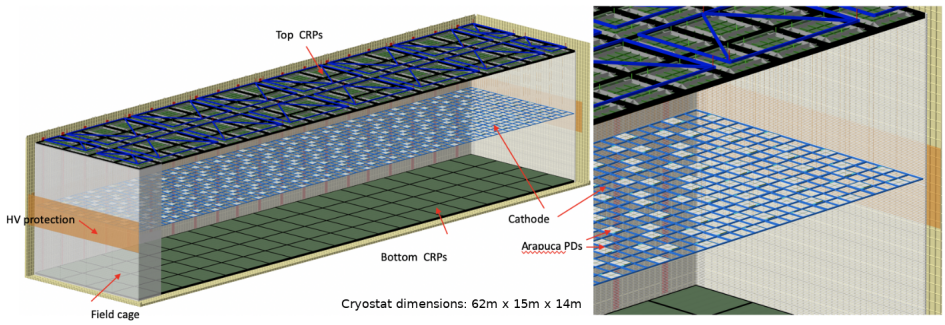

Figure 2.10: Scheme of the vertical-drift LAr TPC [54].

The photon detectors are based on X-Arapucas, which will be mounted on the cryostat walls, behind a field cage with increased transparency, or on the cathode surface. This system requires novel optoelectronic systems for signal and power transmission: the power of the system will be supplied over fiber and an analog optical transmitter is being developed to transmit the signals of the SiPMs in warm conditions.
Currently, an intense R&D campaign is being carried on to test and validate the system.

2.3.3 Near Detector

The Near Detector, shown in Fig. 2.11, is a complex of detectors located 574 m away from the source of the LBNF beam and 62 m underground. In Phase I, it will consist of three detectors: SAND, ND-LAr and TMS. In Phase II, the TMS will be replaced by ND-GAr [55]. Together with the FD, ND will be involved in the measurements of the CP violating phase, the determination of the mass ordering, the measurement of the mixing angle θ_{23} and its octant and the test of the three-neutrino paradigm. Furthermore, one of the general issues is the difficulty in reconstructing the energy spectrum, that is an unresolved convolution of cross section, flux and energy response, due to the finite energy resolution and non-zero biases. Hence, this requires the ND to outperform the FD and to independently constrain each quantity. The ND is expected to characterize with high statistic the beam close to the source: the data collected from the ND can be compared with the FD ones to reduce systematic uncertainties and to improve beam and neutrino interaction models. In addition, thanks to the Precision Reaction Independent Spectrum Measurement (PRISM) program, it will acquire data at different off-axis beam positions, thus with different energy spectra, allowing DUNE to deconvolve the beam and cross section models and constrain each component separately. So, the energy spectrum of neutrinos can be measured by both FD and ND, with the differential rates of ν_e and ν_μ, given by the Eqs. 2.1, 2.2.

$$\frac{dN^{FD}_{\nu_x}}{dE_{rec}} = \mathcal{N}^{FD} \int \Phi^{FD}_{\nu_\mu}(E_\nu) P_{\nu_\mu \to \nu_x}(E_\nu) \sigma^{Ar}_{\nu_x}(E_\nu) R^{Ar}_{\nu_x}(E_\nu, E_{rec}) \epsilon^{FD}_{\nu_x}(E_\nu, E_{rec})\, dE_\nu, \tag{2.1}$$

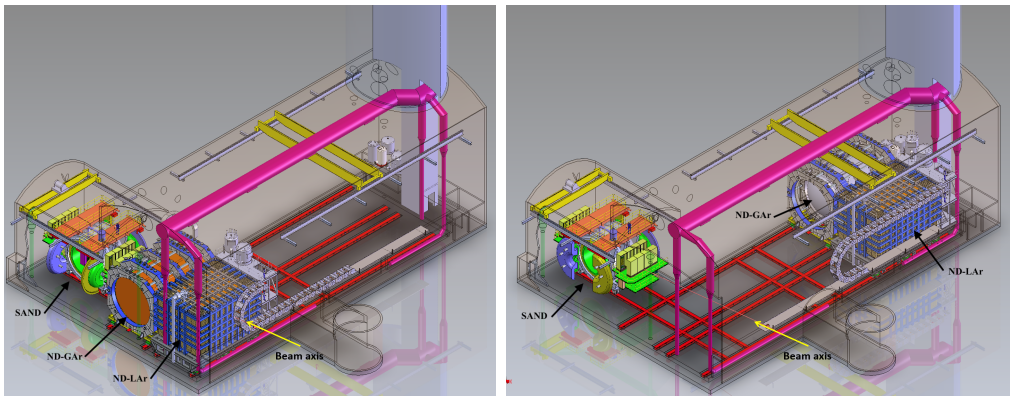

(a) (b)

Figure 2.11: Design of the DUNE ND complex, with component detectors all on-axis (a) and with ND-LAr and ND-GAr off-axis (b). The beam axis and direction is indicated by the yellow arrow [55].

$$\frac{dN_{\nu_x}^{ND}}{dE_{rec}} = \mathcal{N}^{ND} \int \Phi_{\nu_\mu}^{ND}(E_\nu) P_{\nu_\mu \to \nu_x}(E_\nu) \sigma_{\nu_x}^{Ar}(E_\nu) R_{\nu_x}^{Ar}(E_\nu, E_{rec}) \epsilon_{\nu_x}^{ND}(E_\nu, E_{rec})\, dE_\nu, \tag{2.2}$$

where $\mathcal{N}$ is a normalization factor, E_ν is the true neutrino energy, E_{rec} is the reconstructed one, σ_ν is the neutrino interaction cross section, R_ν is the probability that a neutrino produces a charged particle and ϵ_ν is the detector efficiency. In order to reconstruct neutrino events, understanding neutrino interactions in LAr is a fundamental task. They can be considered as collisions with nucleons, with a possible subsequent scattering where the nucleons can produce mesons. Then, the mesons, crossing the nucleus, can interact with other nucleons. These processes are the main ones responsible for the systematic uncertainties in the interactions.
The DUNE experiment will search for quasi-elastic scattering (QE), resonance production (RES) and deep inelastic scattering (DIS), thus in the energy region between 0.5 GeV and 10 GeV. In particular, SAND aims to constrain these interactions in LAr: indeed, even a small variation in the computation of a relative uncertainty can significantly affect the sensitivity to the parameters of interest, increasing the exposure needed to reach the 5σ significance for claiming a discovery.
In the next paragraphs, ND-LAr, TMS and ND-GAr will be described. SAND will be outlined in the next chapter.

ND-LAr

In order to reduce cross section and detector systematic uncertainties for oscillation analysis, the ND target material must be the same as that of the FD one, i.e. liquid Argon. At the Near Detector, the neutrino flux and the event rate will be high enough to cause pile-up issues in a traditional TPC. To solve this problem, the ND-LAr, shown in Fig. 2.12, will be built on the base of ArgonCube technology: the detector is modularized to improve drift field stability, to reduce the high voltage and purity requirements; the charge readout is pixelized, to provide 3D imaging

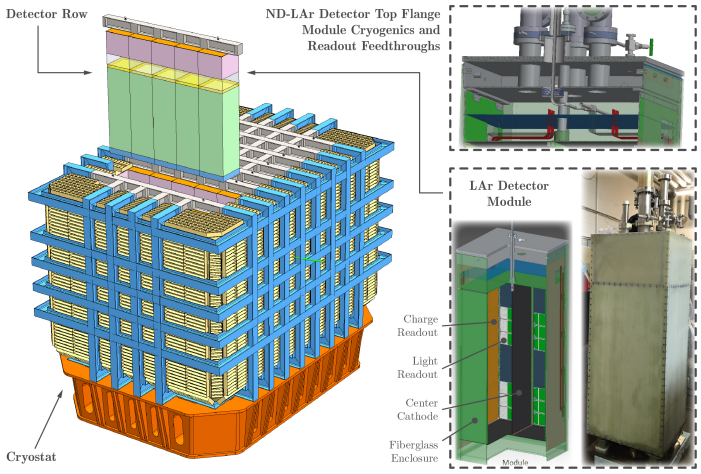

Figure 2.12: Design of the ND-LAr detector, with zoom on the detector modules and read out [55].

of particle interactions; new light detection techniques are proposed to increase the light yield. Furthermore, the dead material due to the modularization will be minimized using a resistive field shell instead of traditional field shaping rings. This subdivision of the volume will allow shorter drift times and distances and will reduce the overlapping interactions.
The detector will be 5 m (along beam) × 7 m (transverse to the beam) × 3 m (height) of dimensions, with 67 ton of fiducial mass, optimized to ensure hadronic showers containment and to provide enough statistics (1×10^8 ν_μ events per year). ND-LAr will be also able to deal with a large number of neutrino interactions in each spill. The LBNF neutrino beam will consist of 10 μs wide spill, with $\mathcal{O}$(ns) structure, delivered at $\sim$ 1 Hz rate. Hence, neglecting the cosmic rays, that have a low rate ($\sim$ 0.3 per spill at 60-m depth), $\mathcal{O}(50)$ interactions per spill are expected. The 3D pixel charge will be read out continuously. The slow drifting electrons will be read out with an arrival time accuracy of 200 ns and a corresponding charge amplitude within $\sim$ 2 μs-wide bin. This, together with the spill width, will give a position accuracy of $\sim$ 16 mm. Even if this is an already good spatial resolution, the light system of ND-LAr will provide a more accurate time-tag of the charge, associating all charges to the proper neutrino event and rejecting the pile-up of charges from other neutrino signals.

TMS

ND-LAr will be optimized to contain hadronic showers, but its acceptance for muons with momentum larger than $\sim$ 0.7 GeV/c will be low. For this reason, in Phase I, an additional spectrometer, called The Muon Spectrometer (TMS) will measure the properties of the muons that escape ND-LAr (Fig. 2.13).
TMS will be made of a magnetized range stack with 100 layers, with dimensions 7.4 m (width) × 5 m (height) × 7 m (depth). Each plane will be made of 192 scintillator slats, 3.5 wide and read out by SiPMs, separated by steel plates 15-mm thick in the 40 layers upstream and 40-mm thick in the 60 layers downstream.
The magnetic field of 0.5 T will allow TMS to reconstruct the muon charge sign and

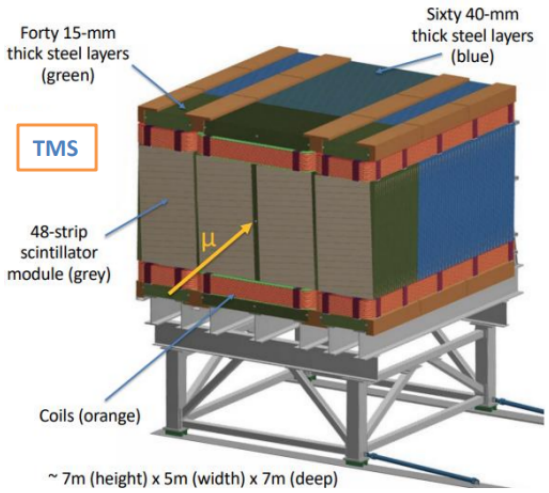

Figure 2.13: Design of the TMS detector.

the momentum up to $\sim$ 5 GeV with $\sim$ 5% resolution.

ND-GAr

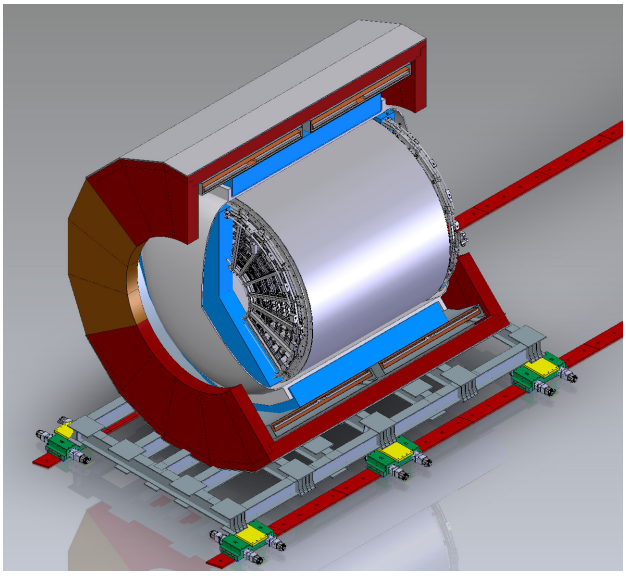

Figure 2.14: Design of ND-GAr, showing the HPgTPC, the pressure vessel, the ECAL, the magnet. The muon-tagging detectors are not shown [55].

In Phase II, TMS will probably be replaced by ND-GAr, shown in Fig. 2.14. It will be a magnetized detector system consisting of a high-pressure gaseous argon TPC (HPgTPC) surrounded by an electromagnetic calorimeter (ECAL), both in a 0.5 T magnetic field and a muon system.
Basically, it will be a gas-filled cylinder with a high-voltage electrode at mid-plane, that provides the drift field for ionization electrons. The gas chosen for this purpose is an Ar-CH_4 mixture, 90%-10% (molar fraction), at 10 bar. In ND-GAr, the structure will be organized such that the magnetic and the electric fields are parallel,

to reduce transverse diffusion thus giving better point resolution. The end plates of the cylinder, where the primary electrons drift, will be provided with multi-wire proportional chambers (MWPCs), that start avalanches (that is, gas gain) at the anode wires. Signals proportional to the avalanches are induced on cathode pads located behind the wires. The hit position reconstruction will be given by the induced pad signals for two of three coordinates, for the third one the drift time will be exploited.
ND-GAr will collect $\sim 1.6 \times 10^6$ ν_μ CC events per year, given its 1-t fiducial mass. These events can be studied with a very low momentum threshold for charged particle tracking and with systematic uncertainties that differ from those of the liquid detectors. Since it can access lower-momentum protons and has PID capabilities better than ND-LAr one, it will be very useful for the study of charged particles' activity near the interaction vertex. The misidentification of π as knocked-out protons can cause significant mis-reconstruction of neutrino energies and event topologies in the LAr TPCs.

Chapter 3

SAND and GRAIN Detector

The System for on-Axis Neutrino Detection (SAND) is one of the three detector of the Near Detector complex of the DUNE experiment.
SAND aims to monitor the beam on-axis, producing statistically significant measurements of the neutrino beam spectrum, to control systematic uncertainties for the oscillation analysis, to contribute to precisely measures neutrino cross-sections and to perform short-baseline neutrino physics studies.
The SAND design (see Fig. 3.1) consists of a superconducting solenoidal magnet, which surrounds the Electromagnetic Calorimeter (ECAL), the Straw Tube Tracker (STT) and GRAIN, a LAr active target. Both the magnet with its iron yoke and the ECAL were originally part of the KLOE experiment, located at INFN LNF in Frascati. The STT and GRAIN replace the central tracker of KLOE. They will contribute to study the neutrino interaction models and to constrain nuclear effects. GRAIN (GRanular Argon for Interactions of Neutrinos) detector will be an active LAr target, located in the upstream region of SAND. It will perform tracking and calorimetric measurements through a novel imaging technique, exploiting the scintillation photons produced in LAr by the passage of a charged particle.

In this chapter, the physics goals of SAND and its components will be presented. GRAIN will be discussed in greater detail in the last section, as it is the subject of this thesis work. If not otherwise specified, the information presented here is sourced from the ND Conceptual Design Report [55] or the SAND proposal [58].

3.1 Physics goals

The main goal for SAND is the monitoring of the neutrino interactions, of the beam spectrum and of the time variations of the neutrino beam on-axis. To accomplish this task, SAND must have a large enough target mass such that the neutrino interaction rate can provide a statistically significant feedback on changes in the beam over a time period of a few days. All these measurements will be crucial to optimally describe the beam model and to extract the expected FD spectra: it is important indeed to know which are the causes that induce variations in the off-axis flux observed by ND-LAr and TMS/ND-GAr.
Satisfying these goals leads SAND to have several additional capabilities. In particular, it is able to measure independently the interaction rate and energy spectra of muon and electron components of the neutrino beam and it can combine informa-

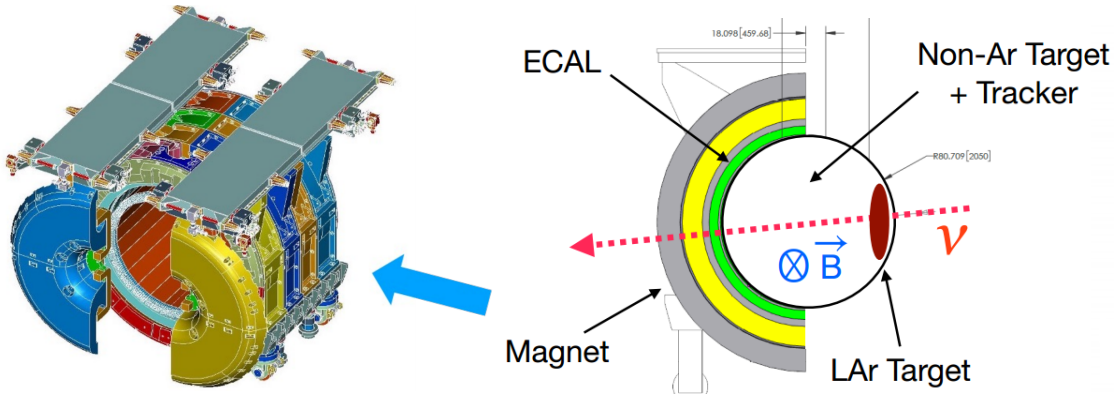

(a) (b)

Figure 3.1: (a) Magnet and ECAL of the KLOE detector [56], (b) Sketch of SAND vertical cross-section [57].

tion from the ECAL and tracker/target to tag neutrons and measure their energy, improving the neutrino energy resolution.

Flux measurements

The SAND detector will perform measurements on the absolute and relative on-axis neutrino flux for the different components of the beam, through several physics processes. A precise knowledge of the fluxes is fundamental to unfold the different terms that appear in the calculation of the event rate at the ND, defined in Eq. 2.2. SAND will be able to determine absolute $\nu_\mu, \overline{\nu}_\mu$ and relative $\nu_\mu, \overline{\nu}_\mu, \nu_e, \overline{\nu}_e$ fluxes with excellent precision, in particular:

- absolute ν_μ flux from $\nu + e \to \nu + e$ elastic scattering;
- absolute and relative $\overline{\nu}_\mu$ flux from $\overline{\nu} + p \to \mu^+ + n$ quasi-elastic scattering on H with $Q^2 \approx 0$, since the σ_{QE} is a constant determined by neutron β-decay with 1% precision;
- relative ν_μ and $\overline{\nu}_\mu$ fluxes versus E_ν from $\nu(\overline{\nu}) + p \to \mu^\mp + p + \pi^\pm$ on H with $E_\nu < 0.5$ GeV;
- relative $\overline{\nu}_\mu$ flux versus E_ν from $\overline{\nu} + p \to \mu^+ + n$ quasi-elastic scattering on H with $E_\nu < 0.25$ GeV.
- ratio of $\overline{\nu}_\mu/\nu_\mu$ fluxes versus E_ν from coherent π^-/π^+ on C, measuring the ratio within the same beam polarity (neutrino or antineutrino mode) from coherent interactions on C (isoscalar) inside radiator targets;
- ratio of ν_e/ν_μ and $\overline{\nu}_e/\overline{\nu}_\mu$ from $\nu(\overline{\nu})$ CC interactions on H and on CH_2 targets;
- determination of parent $\mu/\pi/K$ distributions from $\nu(\overline{\nu})$ CC on H and CH_2 at low-ν, that requires a fit of both ν_μ and $\overline{\nu}_\mu$ distributions.

Cross-section and nuclear effects

Nuclear effects due to the neutrino-nucleon interaction are a great source of uncertainties in the computation of the cross section. To tackle this problem, both ND and FD will be provided with a LAr target, such that the effects of nuclear smearing can be cancelled, thus reducing the uncertainties given by the theoretical models. However, a comparison between these two detectors is complicated, mainly because of their different angular acceptance, that causes different energy spectra, and, in addition, not all the factors will cancel exactly. Understanding the nuclear smearing and constraining the corresponding uncertainties is crucial and it requires multiple nuclear targets different from Ar. Among these additional targets, almost all of them still rely on nuclear models to transfer measurements to Ar, except for Hydrogen. Neutrino interaction processes with H, indeed, are very well-known and can provide the missing information to reduce systematic uncertainties.
SAND will contribute to this task by reducing systematic uncertainties and reconstructing events from Ar and H. A pure H target is problematic to build, but measuring the interactions on graphite (C) and plastic (CH_2) targets makes it possible to study the neutrino interaction with H, through a statistical subtraction. Since H is at rest, the CC events are balanced in the transverse plane, hence the muon and the hadron are produced back-to-back in the same plane. In the case of interactions with heavy nuclei, instead, both initial and final states are affected by nuclear effects, so there is a missing transverse momentum and a smearing of the transverse plane kinematics.
Assuming that the fluxes are precisely measured, the terms in Eq. 2.2 are only $\sigma^m_{\nu_x} R^m_{\nu_x} \epsilon^m_{\nu_x}$. Given that Hydrogen has $R^H_{\nu_x} = 1$, a comparison between Ar and H interactions yields:

$$\frac{\mathcal{N}^{Ar}_{\nu_x}}{\mathcal{N}^{H}_{\nu_x}} = \frac{\sigma^{Ar}_{\nu_x} R^{Ar}_{\nu_x} \epsilon^{Ar}_{\nu_x}}{\sigma^{H}_{\nu_x} \epsilon^{H}_{\nu_x}} \tag{3.1}$$

hence the product $\sigma^{Ar}_{\nu_x} R^{Ar}_{\nu_x}$ can be constrained, since the efficiencies ratio is essentially defined by $\delta p/p$ (calibrated to 0.2% from the K_0 mass peak) and $\sigma^H_{\nu_x}$ can be measured as explained above. This product, that has a large theoretical uncertainty, represents the probability for a final-state particle to be produced with momentum p' from a neutrino with momentum p that interacts with a nucleus.

Precision measurements and nucleon structure investigation

The collected statistics and the precise determination of neutrino and antineutrino fluxes will allow DUNE to perform many precision measurements, complementary to the other attempts still ongoing at collider, fixed-target and nuclear physics experiments.

SAND will be able to determine the weak mixing angle $\sin^2\theta_W$ from the ratio of NC and CC deep inelastic scattering (DIS) induced by neutrinos $\mathcal{R}^\nu = \sigma^\nu_{NC}/\sigma^\nu_{CC}$, that actually is dominated by theoretical systematic uncertainties on the structure functions of the target nucleons. Another independent measurement of this angle comes from NC $\nu_\mu e$ elastic scattering, extracting the ratio $\mathcal{R}_{\nu e}(Q^2) = \sigma(\overline{\nu}_\mu e \to \overline{\nu}_\mu e)/\sigma(\nu_\mu e \to \nu_\mu e)$. This channel is free from the hadronic uncertainties but its tiny cross section limits the statistics.

The large statistic of $\nu(\overline{\nu}) - H$ interactions available gives the possibility to test the Adler sum rule $S_A = 0.5 \int_0^1 dx/x(F_2^{\overline{\nu}p} - F_2^{\nu p}) = I_p$ [1]. The Adler sum, in the quark-parton model, is the difference between the number of valence u and d quarks of the target and gives the isospin of the target. The Adler sum is measured as a function of the transfer momentum Q^2 from the structure functions $F_2^{\overline{\nu}p}$ and $F_2^{\nu p}$. The measurement obtained from H can be compared with the one from C, for which $S_A = 0$. It can be also sensitive to possible variations of the isospin (charge) symmetry, heavy quark production (charm) and strange sea asymmetries $s - \overline{s}$.

For a better understanding of the nucleon structure, the strange quark contribution to the vector and axial-vector currents and to the spin Δs of the nucleon is an important element. SAND will be able to determine the axial-vector form factor from a measurement of the NC elastic scattering off protons $\nu_\mu(\overline{\nu}_\mu)p \to \nu_\mu(\overline{\nu}_\mu)p$. Indeed, the NC differential cross-section is proportional to the axial-vector form factor $d^2\sigma/dQ^2 \sim (-G_A/2 + G_A^s/2)^2$, where G_A is the known axial form factor and G_A^s is the strange form factor. This process can also provide the most direct measurement of Δs, by extrapolating the NC differential cross-section to $Q^2 = 0$, since in this limit $G_A^s \to \Delta s$. G_A can be determined by the combined measure of $\mathcal{R}_{\nu p}(Q^2)$ and $\mathcal{R}_{\overline{\nu}p}(Q^2)$, where $\mathcal{R}_{\nu p}(Q^2) = \sigma(\nu_\mu p \to \nu_\mu p)/\sigma(\nu_\mu n \to \mu^- p)$.

The possibility to integrate several thin nuclear targets inside STT allows for a deep study of the nuclear structure with the related nuclear effects on structure functions, form factors and cross sections.

3.2 SAND components

3.2.1 Magnet and iron yoke

The design of the SAND detector features a solenoidal superconducting magnet (see Fig. 3.2), taken from the KLOE detector at the DAΦNE collider, which operated until 2008 at the INFN LNF laboratory [59]. This magnet was designed together with its iron yoke, and produces 0.6 T over a 4.3-m long, 4.8-m diameter volume. The coil operates at a nominal current of 2092 A and its stored energy is 14.32 MJ. It is a two-layer conductor, a composite of an (Nb-Ti) Rutherford cable co-extruded with high-purity aluminium, wound on flat with a full vacuum-impregnated insulation system. The coil is located inside a cryostat, which has an outer diameter of 5.76 m, an inner diameter of 4.86 m, 4.40 m length, and an overall cold mass of $\sim$ 8.5 ton. The return yoke, weighting 475 ton, surrounds the cryostat.

The coil cooling is done through thermo-siphoning cycles: gaseous He at 2.5 K is inserted at 3 bar from the cryogenic plant and melted through Joule-Thomson valves into a liquid He container in thermal contact with the coil. The current leads are cooled with liquid He, while the radiation shields are cooled with gaseous He at 70 K [55].

[1] $F_2 = x(\frac{4}{9}u(x) + \frac{1}{9}d(x))$ where $x = \frac{Q^2}{2pq}$ with $Q = -q$. q represents the momentum transferred by the mediator of the interaction to a parton whose momentum is a fraction x of the total nucleon momentum p.

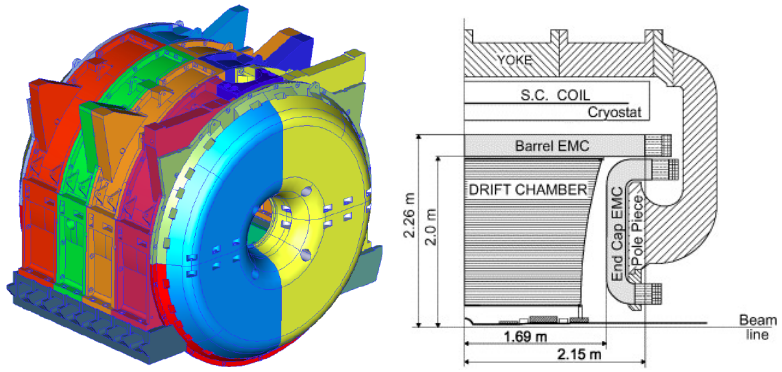

(a) (b)

Figure 3.2: The KLOE detector: (a) 3D engineering CAD model of the magnet and (b) vertical cross section [60].

3.2.2 Electromagnetic calorimeter (ECAL)

In the SAND design, the ECAL also comes from the already existing calorimeter of the KLOE detector. The KLOE ECAL is a lead-scintillating fiber calorimeter, read out by photomultiplier tubes. Scintillating fibers ensure a good light transmission over several meters, sub-nanosecond time accuracy and a very good hermeticity. The calorimeter cylindrical barrel (see Fig. 3.3) is placed inside the KLOE magnet, close to the coil cryostat. It consists of 24 modules, each of dimensions 4.3 m (length) $\times$ 23 cm (thickness) and with a trapezoidal cross section, with bases of 52 and 59 cm. Each end cap is formed of 32 vertical modules that are 0.7$-$3.9 m long and 23 cm thick, with a rectangular cross section of variable width. The modules are stacked in groups of 200 grooved lead foils, with 0.5 mm of thickness, which alternate with 200 layers of cladded 1-mm diameter scintillating fibers. The endcap modules are bent at the upper and lower ends to permit the positioning into the barrel calorimeter and also to place the phototube axes parallel to the magnetic field. The KLOE calorimeter has no inactive gap between its components since there is a large overlap of barrels and end-caps. Its total weight is $\sim$ 100 ton and the read-out system is equipped with 4880 phototubes [60].

The ECAL energy and time resolutions, measured in the KLOE commissioning and operating phases, are:

- spatial resolution in $r - \phi$: $\sim$ 1.3 cm;
- energy resolution: $\sigma_E/E = 5\%/\sqrt{E\ (\text{GeV})}$;
- time resolution: $\sigma = 54/\sqrt{E\ (\text{GeV})}$ ps.

3.2.3 Straw tube tracker (STT)

The Straw Tube Tracker (STT) will be a target-tracker for neutrino interactions, performing precise measurements of all charged particles' momentum. Its building requirements are derived from its physics goals. In particular, it has low density and high track sampling, to ensure optimal momentum, angular and spatial resolution,

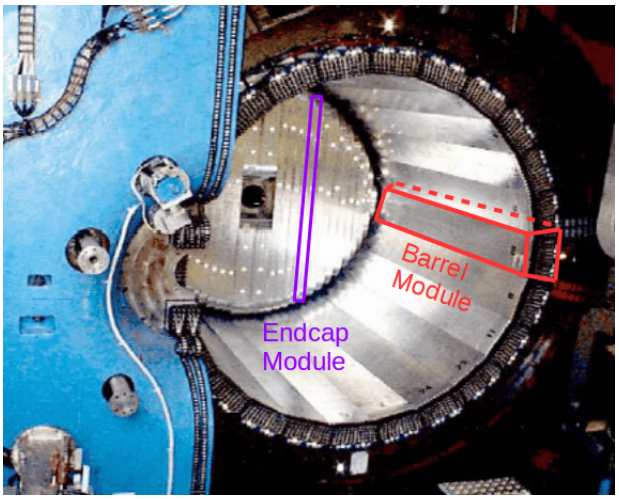

Figure 3.3: A view of the KLOE calorimeter: the far end-cap is closed and ECAL modules can be seen as vertically oriented slabs [55].

and its total thickness is comparable to the radiation length, such that the secondary interactions are minimized. In order to study neutrino-nucleon interactions, it has the possibility to house different target materials. The STT can perform particle identification of $e^{\pm}, \pi^{\pm}, K^{\pm}, p, \mu^{\pm}$, together with the calorimeter, and it has enough target mass to collect sufficient statistics to measure neutrino flux.

The STT system is divided into modules, and each can be operated independently using different nuclear targets (such as C, Ca, Fe, Pb...). Its technology is based on low-mass straws, made of 20 μm gold-plated tungsten wires, placed inside tubes with 5 mm diameter, walls of 12 μm and 70 nm of Al coating. They are filled with a gaseous mixture of Xe/CO_2 70/30 operated at $\sim$ 1.9 atm. The single point resolution is designed to be < 200 μm.

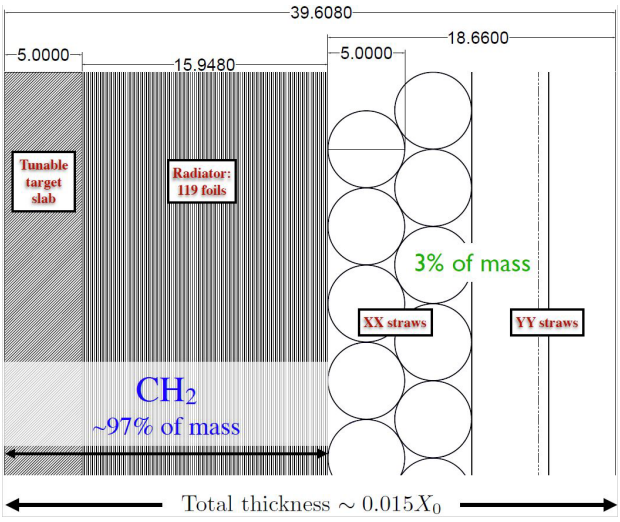

Figure 3.4: STT module scheme, with three main elements (left to right): a tunable polypropylene CH_2 target; a radiator with 119 polypropylene foils for $e^{\pm}$ ID; four straw layers XXYY (beam along z axis and B field along x axis). (Distances in mm) [55].

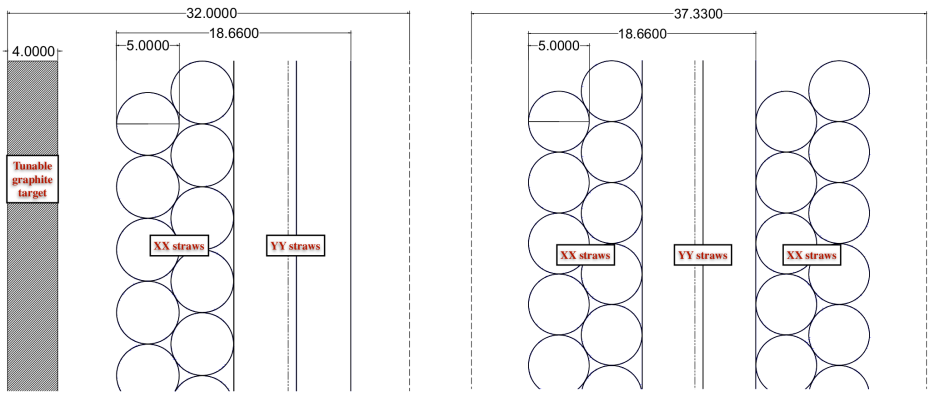

(a) (b)

Figure 3.5: (a) Section of the graphite module with the radiator and the CH_2 slab replaced by a graphite target; (b) Section of the tracking module with six straw layers. (Distances in mm) [56].

At the time of writing this thesis the STT design is not optimized yet. In the latest design, it is planned with three types of STT modules.

The first type of module is a polypropylene CH_2 target slab followed by a radiator and four straw layers XXYY, as in Fig. 3.4. The slab has a thickness of 5 mm. The radiator consists of 105 18-μm thick foils of polypropylene $(CH_2H_6)_n$, separated by 117 μm of air gaps. It is 15.95 mm thick and, using the transition radiation emission, it will be able to perform an optimal e/π differentiation. This STT configuration contains 6.98 mm of CH_2 overall, that corresponds to $\sim 1.5\%$ of the radiation length. The second type of STT module is composed of a graphite (C) target and four straw layers XXYY, as shown in Fig. 3.5.a. The C target is 4 mm thick, that corresponds to the same X_0 percentage of the first module type. It will allow us to measure the C background in the selection of Hydrogen interactions in C_3H_6 target. Modules with graphite are usually alternated with CH_2 modules to have the same detector acceptance for both targets.

The third STT module type, the "tracking module" (see Fig. 3.5.b) consists simply of 6 straw layers fixed together with a XXYYXX configuration.

In total, the STT system contains 70 modules with CH_2, slabs and radiators, 8 with C targets and 6 tracking modules. As shown in Fig. 3.1, it occupies all the SAND volume, except for the upstream region, dedicated to the LAr target (GRAIN). The tracking modules are located close to GRAIN and in the downstream region, while the graphite and CH_2 modules are alternated, filling the inner volume.

3.3 GRAIN

The GRanular Argon for Interactions of Neutrinos (GRAIN) detector is a $\sim$ 1 ton LAr active target. It has the goal of constraining systematic uncertainties from nuclear effects through inclusive Ar interactions. It will be located in the upstream region of the SAND magnetized volume and will be always on-axis, allowing cross-calibration with the other detectors.

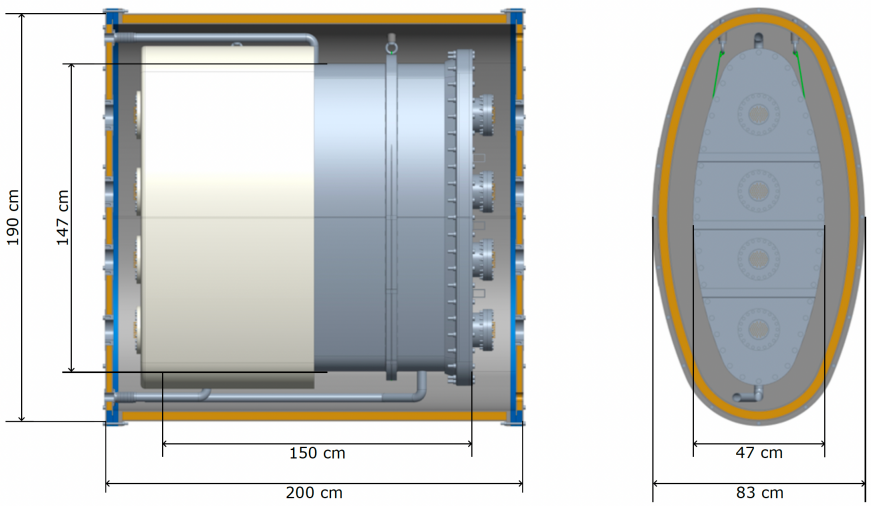

Figure 3.6: Design of the lateral projections of the GRAIN inner and outer vessels with detailed dimensions [56].

The GRAIN design foresees two coaxial cylindrical vessels, with a highly elliptical base, arranged such that the neutrino beam is aligned with the shorter axis of the ellipse, as shown in Fig. 3.6. The inner vessel is 150 cm wide, with a major axis of 146.5 cm and a minor axis of 46.5 cm. It is made of stainless steel, 6 mm thick in the curved walls and 20 mm at the endcaps, where flanges are placed to insert the cables of the readout electronics. It is filled with liquid Argon. The outer vessel is 200 cm long, with axes of 190 cm $\times$ 83 cm. It is composed of a double shelled 6-mm thick Carbon fiber and 40 mm honeycomb structure, reinforced with an aluminium alloy along the ellipse profile. Between the two vessels there is vacuum, maintained at the pressure of $10^{-4} - 10^{-5}$ bar to thermally insulate the inner vessel.

The design aims at minimizing the vessel material, that has a thickness of a small fraction of radiation length. To reduce energy loss, showering and multiple scattering, the overall depth of the LAr volume is kept to a minimum (1 interaction length).
Tipically, a LAr-based detector utilizes a TPC technology for tracking and reconstruction. In this context, however, there are some limitations to the construction of a LArTPC: the primary concern is that at the ND the number of events and the pile-up are too high to be managed by a traditional TPC because the drift time of the ionization charges is $\sim \mathcal{O}$(ms). One possible solution is to design a detector similar to the ND-LAr, with modular small LArTPCs. However, we are currently studying a different approach: a novel tracking and calorimetry system that is entirely based on the imaging of LAr scintillation light.
This idea comes from the bubble chambers detection technique: charged particles crossing a superheated liquid deposit some of their energy, inducing the liquid to vaporize, with a subsequent formation of microscopic bubbles along the particle trajectory. This event is captured by several photographic cameras placed all around the chamber, allowing for a 3D reconstruction of the event. In the same way, charged particles, crossing liquid Argon, deposit energy causing ionization and excitation of the Ar atoms. After the excitation, there is emission of scintillation light, that can be captured by pixel-segmented photon detectors placed on the inner walls and im-

mersed in Ar. Despite the simplicity of this idea, it presents many challenges, such as the need for an imaging system that is able to work in a cryogenic environment and that is sensitive to the wavelength of the photons emitted by Ar.
LAr properties and imaging systems proposed are outlined in the following section. In Sec. (4), the reconstruction technique and the simulation chain will be presented. In particular, a detailed description of the tracking performance of the detector, with the reconstruction implementation and the optimization of camera geometries is discussed in [56]; while calorimetry studies using the same imaging system are presented in [61].

LAr properties

In the experiments of the neutrino and Dark Matter sector, Liquid Argon is commonly chosen as an active medium, mainly because it has an optimal charge yield and transport and good scintillation properties.
The photon emission process of LAr is due to the decay to the ground state of the Ar_2^* excimer: precisely, the lowest-lying single state, $^1\Sigma_u^+$, and the triplet state, $^3\Sigma_u^+$ decay emitting scintillation photons of $\sim$ 9.7 eV in 7 ns and 1.6 μs, respectively. Due to the different lifetimes of these two states, the singlet is considered as the *fast* component, while the triplet as the *slow* component [62]. As clearly shown in Fig. 3.7, the particle type affects the relative abundance of the two components, allowing particle identification. The typical light yield in LAr is $\sim$ 40k photons per MeV of deposited energy.

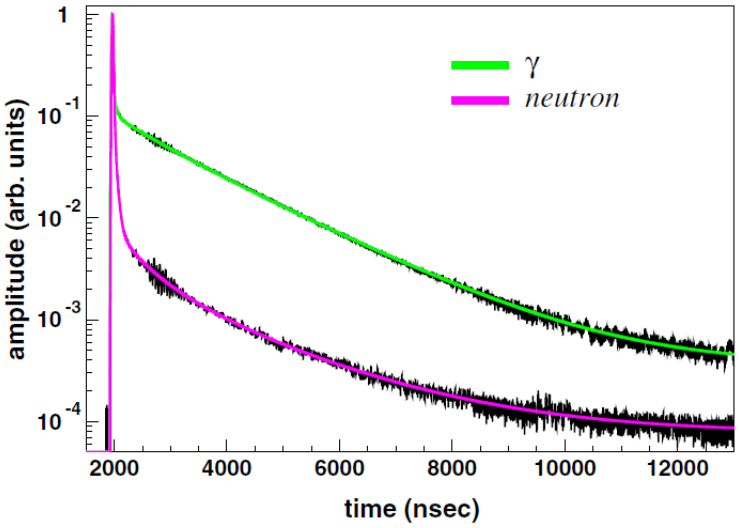

Figure 3.7: Signal shape of scintillation light in LAr for gammas (green) and neutrons (magenta). The peaks are due to the fast component, while the tails come from the slow one [63].

Many experiments measured the typical wavelength of scintillation photons, which is not related to the time components, obtaining a value of about 127 nm, in the vacuum ultraviolet (VUV) range.
Although LAr shows an excellent light yield and transparency to its own scintillation light, quenching and absorption caused by possible impurities worsen its per-

formance. In particular, quenching processes reduce the number of Ar_2^+ molecules by non-radiative decay in two-body collisions with impurity molecules such as N_2 and O_2. For example, the absorption processes due to the presence of Oxygen cause the formation of atomic metastable states, that emit their excitation energy as heat. The only interaction that scintillation photons undergo is the Rayleigh scattering, where there is no direct loss of light yield but only a change of direction. However, this is a problem since it leads to a larger absorption and scattering probability that make the reconstruction process more complicated. According to the results presented in [64], the scattering length is about $\lambda_{RS} = 99.1 \pm 2.3$ cm, derived from the measured propagation group velocity of scintillation light in LAr. The scattering length is related to the wavelength of the photons, as $\lambda_{RS} \propto \lambda^4$, hence it can be increased using a wavelength shifter. This is usually accomplished by doping the LAr with a small amount of Xenon: as presented in [65], the photons emitted in Xenon-doped liquid Argon have a spectrum peaked at 178 nm leading to a scattering length of several meters.

GRAIN will be able to deal with the high ND expected event rate thanks to its imaging system that, collecting the fast component light, has a time response of a few hundreds of ns. The scattering length of about 1 m, instead, can affect the measure at the GRAIN scale, hence some precautions have to be considered. As explained before, a possible solution, currently under study, is Xe-doping, that can reduce the scattering and increase the light collection with an improvement of the detector's efficiency. In this thesis, the analysis is carried on without considering any doping in LAr.

Imaging system

The imaging system design is very challenging since it has to fulfill all the requirements needed in GRAIN, such as a good spatial resolution. The already-known possibilities are conventional lenses, that have relatively poor transmissivity to VUV light or mirror-based optics, which have too large dimensions, thus reducing the fiducial volume of GRAIN. The imaging system must collect enough light and must be provided with adequately segmented photosensors, to guarantee a good resolution. In addition, its electronic component must be able to operate in a cryogenic environment, having also the ability to detect single photons and an adequate bandwidth and digitization system to resolve multiple interactions per spill.

The photodetection system is based on matrices of Silicon Photomultipliers (SiPMs). SiPMs have great single-photon sensitivity and some commercial models can operate at cryogenic temperatures, where the presence of dark noise is reduced. On the other hand, these commercial models have a very low sensitivity to the wavelength of scintillation photons emitted in LAr. To mitigate this problem, a wavelength-shifter (WLS) coating covers the sensors, shifting the UV light into the visible range. The chosen material is tetraphenyl butadiene (TPB), an organic compound that, when excited by UV radiation, emits photons through the fluorescence process. The fluorescence photon spectrum has a peak at 430 nm [66], being perfectly suitable for the PDE spectrum of SiPMs (see Fig. 3.8), and that does not change with the wavelength of incident light in the UV range. The fluorescence photons are emitted isotropically, i.e. half of them are sent back in the detector volume. VUV-dedicated commercial models can be another option that is expected

to be available in the near future.

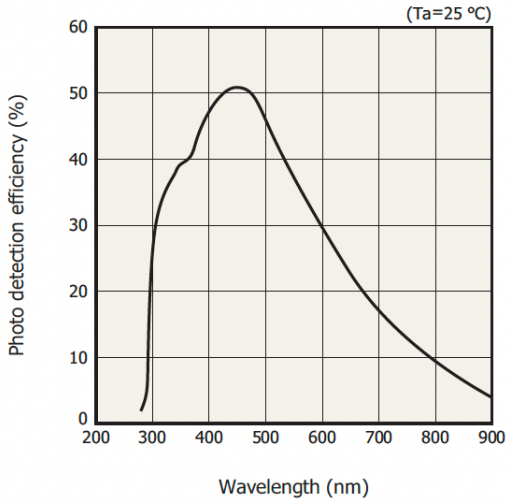

Figure 3.8: Photon detection efficiency (PDE) versus wavelength of incident light of SiPM model Hamamatsu S14160 series [66].

The readout electronics, located inside the Argon volume, must provide information on the arrival time and the number of the incident photons. The design provide a photosensor that consists of a matrix of 32×32 SiPMs, that ensures a relatively high resolution in the reconstruction process. The PDE is set to 25% to take into account the back propagation of half of the photon in the volume.

For the design of this imaging system, two approaches can be pursued. One possible scenario, which is currently under study, uses a novel lens-based system. This system utilizes two plano-convex lenses made of high purity non-crystalline fused silica glasses, that are reasonably VUV-transparent, with a separating volume filled with Nitrogen. The lenses require a LAr-Xe mixture inside GRAIN that produces scintillation light at 175 nm, focused between 40 - 120 cm. They are located in front of a 1024-pixel SiPM arrays of 2×2 mm^2 area, forming the so-called camera, that has a 6 cm diameter and a 12 cm depth. In Fig. 3.9, a design of GRAIN with 53 cameras is displayed. Several studies are still ongoing on this kind of system, and it will not be detailed in this thesis.

The other approach is a mask-based imaging system. Here, the scintillation light coming from LAr passes through coded aperture masks, sheets of opaque material that present a well-defined pattern of square holes, located at a fixed distance in front of the SiPMs. The simple construction process and the absence of transparency requirements on the material choice are among the advantages of this approach. In addition, with a proper optimization of their pattern and of their size, the cameras can be very compact, roughly $2-5$ cm of thickness with a wide field of view, therefore providing a larger fiducial volume for the same cryostat size. Their main drawback is the complexity of the reconstruction process, since the image formed on the sensor is a superposition of images from each aperture. Indeed, the reconstruction technique is based on the back-propagation of the photons through the mask holes, weighting on all the possible combinations. Studies on this technique have been carried out to find the number of cameras, the placement, the sensor size and the pattern for which we have the best reconstruction performance [56]. The possible pattern options

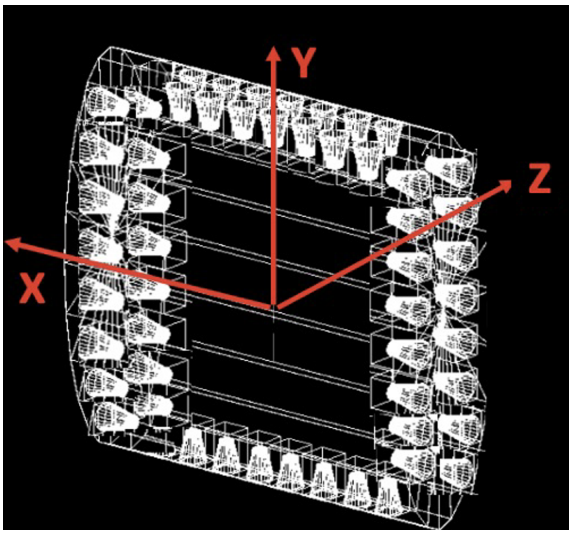

Figure 3.9: Design of GRAIN detector with lens-based imaging system.

for GRAIN, presented in Fig. 3.10, were random patterns and MURAs (Modified Uniformly Redundant Arrays), particular patterns with prime-number rank used in other fields that employ Coded Aperture imaging. A comparison between them indicated a similar performance. As they have no requirements on the matrix rank, random-pattern masks were chosen and used in the simulations. In Fig. 3.11.a, the design of the GRAIN volume is presented, with 60 cameras, where each camera is composed of a mask in front of a sensor, as Fig. 3.11.b shows.

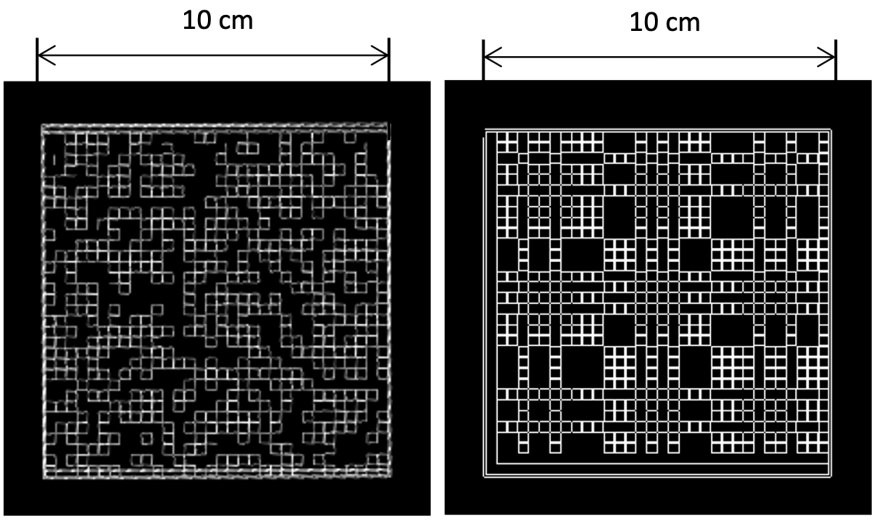

(a) (b)

Figure 3.10: (a) Random-pattern 32×32 mask; (b) MURA 31×31 mask.

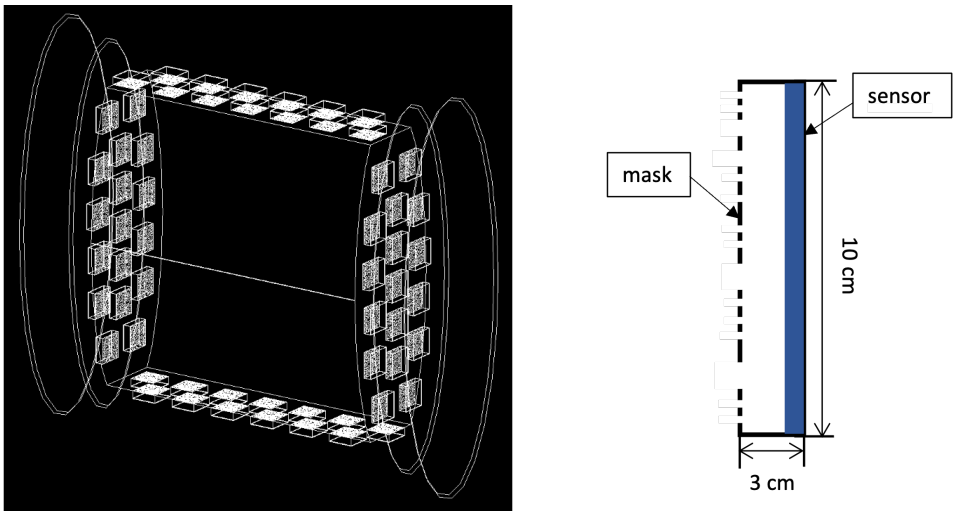

(a) (b)

Figure 3.11: (a) Design of the GRAIN volume with 60 coded aperture cameras; (b) Scheme of the side view of a camera.

Chapter 4

Simulation and reconstruction in GRAIN

A detailed Monte Carlo simulation of the GRAIN detector was implemented to study its performances in reconstructing interactions in LAr using the two different imaging system technologies. It includes several steps, as shown in Fig. 4.1: from the simulation of the detector geometries and the interactions inside the medium to the reconstruction and analysis. In the following, each step will be presented [56].

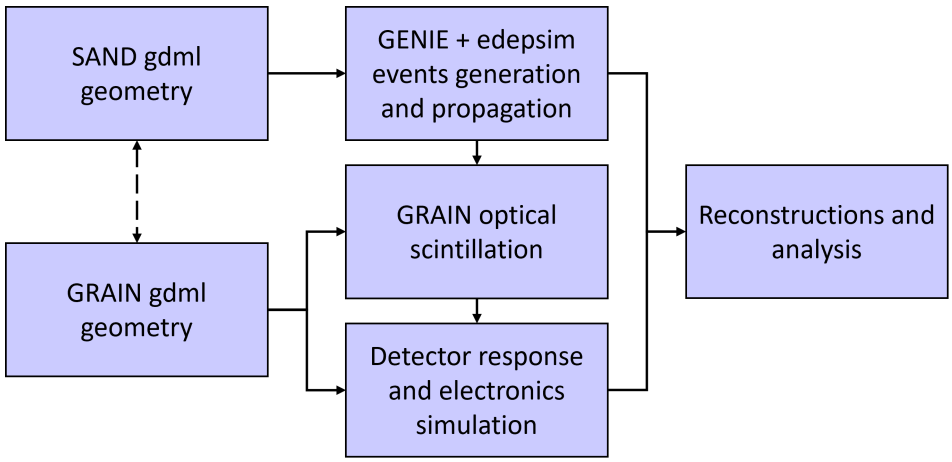

Figure 4.1: Diagram of the simulation and reconstruction chain [56].

4.1 Geometry description

The geometries relative to SAND and GRAIN volume and to the cameras are described through the Geometry Description Markup Language (GDML), a format based on the XML language, that is typically used with Geant4 and ROOT frameworks for the detector geometry description.

The camera description (see Fig. 4.2) includes a mask, a sensor, placed behind the mask, and a surrounding body. The mask is a 0.1 mm thick metal sheet with regular pattern of squared holes with a 3 mm side. The sensor is made of silicon, with typical dimensions 10×10 cm^2 like the effective mask area. The body is a metal box that covers the sensor, shielding it from undesired light. The scintillation

photons produced in GRAIN volume pass through the holes of the mask and arrive on the sensor. Since the camera body is filled with LAr, photons can be produced inside the camera as well. The impact of this extraneous signal and a technique to mitigate it will be discussed in Chap. 5.

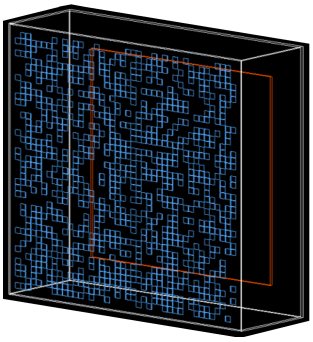

Figure 4.2: Example of camera geometry: the mask (blue) and the sensor (red) are placed on opposite sides, the body (white) is 100% opaque [56].

SAND geometry was implemented using the General Geometry Description software, suggested by the DUNE collaboration. Shown in Fig. 4.3, it contains all the parts described in Sec. 3.2: in particular, GRAIN vessels are simulated according to an elliptical shape with major axis of 192.42 cm and minor axis of 85.4 cm and 193.2 cm of length for the outer vessel; axes of 72.8 cm and 23.75 cm with 150 cm of length for the inner one.
The description of GRAIN cameras is implemented in a separate geometry. This geometry includes the inner vessels, with the same dimensions of the SAND simulation, and the cameras. In this way, it is possible to test many different camera and readout configurations with only one simulation of neutrino interactions in the SAND volume, leading to great flexibility.

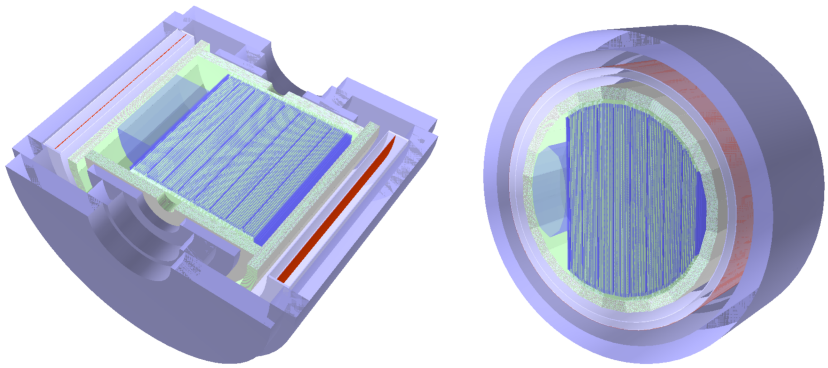

(a) (b)

Figure 4.3: X-Z (a) and X-Y (b) sections of the SAND detector geometry used in the simulation [56].

4.2 Event generation and energy deposit

For the generation of the neutrino interactions, the GENIE neutrino event generator, a ROOT-based MC software adopted by the DUNE collaboration [67], was utilized. It simulates the primary neutrino-nucleon interactions, generating all the particles produced, and the following collisions that the recoiled nucleon makes with other nucleons. This can be accomplished since it includes the description of the main scattering mechanisms. For calibration and validation purposes we simulated other sources such as muon and simple light point directly in GEANT4.

The propagation and the energy deposits of the generated particles are simulated by the Edep-sim software [68], a wrapper around GEANT4. It gives information on the energy deposited through ionization and scintillation processes. In the case of LAr, the Noble Element Simulation Technique (NEST) [69] is used by GEANT4: it is a collection of models that describe the energy loss by scintillation and ionization in noble elements as a function of electric field, particle type and incident energy or energy loss.
Summarizing the process, after a neutrino interaction is generated by GENIE, the file is processed by Edep-sim. Here, its output file contains information on the primary particles, on the trajectories of all the generated particles (also the ones produced in the propagation of the primaries) and on their energy deposit. In particular, Edep-sim documents the starting and stopping point of each energy deposit and the particle that generated it.

4.3 Optical simulation

The output of Edep-sim is then processed by the photon propagation module of GEANT4 to simulate the optical scintillation emission by LAr in GRAIN. The simulation uses the information on energy deposit to emit, propagate and collect the scintillation photons in the simulated GRAIN geometry. The main processes that photons undergo during the propagation are Rayleigh scattering and absorption, for which constant lengths of $\lambda_{RS} = 90$ cm and $\lambda_{abs} = 5$ m, respectively, are fixed in the simulation, even if they are wavelength-dependent. The other input quantities for the simulation are the light yield, the decay times of singlet and triplet states, with the values presented in Sec. 3.3 (LAr properties). In addition, the reflection of the material inside the inner vessel must be considered: since we are developing an imaging system, the reflection must be as small as possible to avoid the detection of photons that are out of interest. Hence, in the simulation, the surface reflection is set to 0%, with an absorption probability of 100%.
The sensor volume inside each camera acts as the detector of the simulation, collecting information on the photons that impinge on its surface. The relevant quantities are: the incident photon position, the direction on the sensor, its detection time and the photon energy. These information are contained in the optical simulation output, which consider 100% efficiency without any fine structure of the image detector. Then, they are processed by another software to simulate the detector response. In this way, it is possible to test many different sensor and readout types with only one optical simulation.

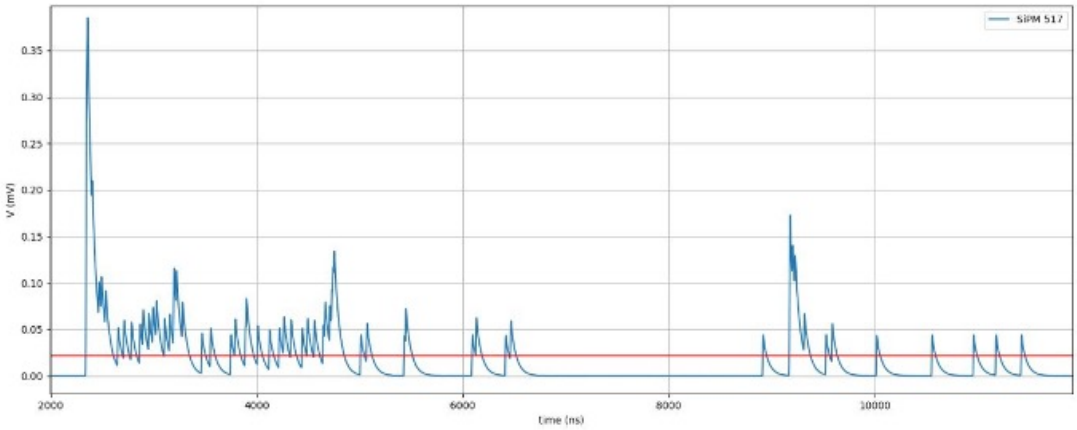

Figure 4.4: Simulated SiPM signal. Note the long tail of separate photons due to the slow component of the argon scintillation (the red line indicates 0.5 p.e. threshold).

4.4 Detector response

A standalone software is dedicated to the simulation of detector response to the collected photons. This tool, mainly written in Python, models the SiPM response and the properties of the electronics. It receives the information from the optical simulation and gives as output the number of photons detected by a SiPM matrix and the arrival time of the first photon for each pixel. The determination of how many photons interact on the sensor surface, among the total amount, relies on a random process. For each photon, a probability value p is extracted from a uniform (0,1) distribution: if $p <$ PDE, the photon is considered as interacting and an amplitude value is associated with it, taken randomly from a Gaussian distribution centered on the average amplitude value generated by a photoelectron. For each photon, a waveform is simulated (4.4) and then all the waveforms are summed together to get the total SiPM response.

4.5 Photon source distribution reconstruction

After the simulation of the detector response, that returns a map of the number of photons measured by each camera, the reconstruction algorithm can be applied.
This process is based on the Maximum Likelihood Expectation Maximization (ML-EM) algorithm [70]. It is an iterative method in which the measured data are considered samples of a set of random variables with p.d.f.s related to the object distribution, according to a mathematical model of the data acquisition process. Through this mathematical model, it is possible to compute the probability that any initial distribution density in the object studied could have produced the observed data. In the set of all possible images, which represent a potential object distribution, the image having the highest such probability is the *maximum likelihood estimate* of the original object [56]. This algorithm is suitable for a 3D application. The volume is divided in voxels and for each voxel the algorithm computes the score, defined as:

$$\lambda^{(k+1)}(j) = \frac{\lambda^{(k)}(j)}{\sum_{s=1}^{S} p(j,s)} \cdot \sum_{s=1}^{S} \frac{H(s)p(j,s)}{\sum_{j'=1}^{J} \lambda^{(k)}(j')\, p(j',s)}, \qquad \text{with} \qquad \lambda^{(0)} = 1. \tag{4.1}$$

The probability matrix $p(j,s)$, called *system matrix*, represents the probability with which an emission from a voxel j is detected in a sensor pixel s; $H(s)$ is the measured number of photon hits in the sensor matrix pixel s and $\lambda(j)$ is the unknown photon counts of voxel j of the segmented volume of interest to be estimated from the measured data.

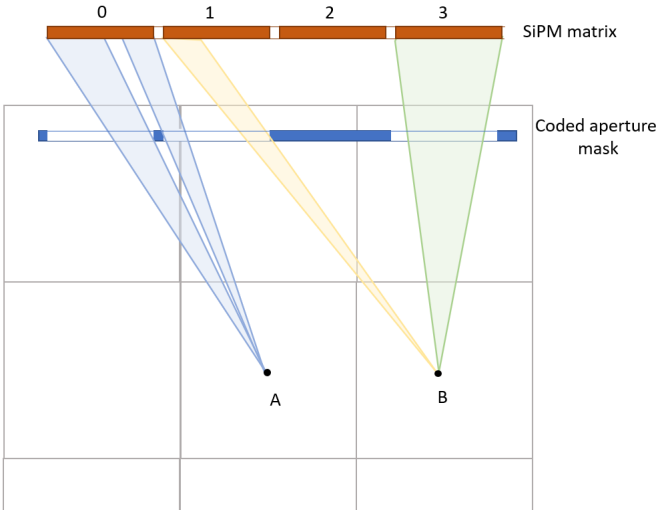

Figure 4.5: Diagram of the solid angle computation for different voxels and sensors, in the case of a Coded Aperture Mask. [56].

Inside the probability term the GRAIN geometry, the attenuation process of the scintillation photons during the propagation and the detector efficiency (i.e. the PDE) are taken into account, resulting in a product of: $p = p_{geom} \cdot p_{LAr} \cdot p_{sensor}$. The estimate of the geometric probability assumes that photons are emitted isotropically, propagate in a straight line and that the distance is large compared to the voxel size. In addition, it depends on the portion of the sensor area that can be seen through the mask holes from the given voxel. Fig. 4.5 shows an example: the voxel with center in A sees sensor 0 through two holes in the mask, and its solid angle is the sum of the angles subtended by the two portions of sensor area visible. For the voxel with center in B, the solid angle relative to sensor 1 is limited by the mask, while the sensor 3 is completely visible.
In this geometric model, the size of pixel edges and mask holes are taken into account, since they are non-negligible with respect to the sensitive area. The iterations, labelled with k, are currently fixed to 500 since it has been observed that further iterations do not improve the reconstruction. As output, the software returns a 3D array that contains the λ values of the voxel scores of the reconstructed volume, where the score is an estimate of the number of photons emitted. This discussion considers only one camera, but the algorithm can be applied directly to multiple cameras, including the probabilities for all sensors in the system matrix.

The ML-EM is well suited for this application, but it has few drawbacks, such as the slow convergence rate and the high computational cost. For these reasons, the computations are performed on GPU, to complete the reconstruction in an acceptable time.

The next step is the simulation chain is the extraction of tracks from the reconstructed voxel clusters. This is the subject of this thesis and it will be presented in Chap. 6.

Chapter 5

Filtering GRAIN data

Not all the scintillation light is produced in the fiducial volume; some is also produced inside a camera when a particle crosses it. Because this light is not *encoded* by the mask the reconstruction technique cannot be applied to it. As a preprocessing step, the cameras that suffer from this issue need to be excluded.

5.1 The problem of dazzled camera recognition

The filtering of GRAIN data is performed immediately prior to the reconstruction step of the simulation chain shown in Fig. 4.1. The particles' propagation and their energy release largely influence the collection of scintillation light in the sensors, resulting in varying light patterns on the sensor matrix depending on the location of the photon emission. There are three possible cases:

- the photons are emitted outside the camera, then all of them are filtered by the mask and observed on the sensors (the camera is called "non-dazzled")(see Fig. 5.1.a);
- the particle hits directly the sensors with a peak amplitude in a narrow region (the camera is called "dazzled")(see Fig. 5.1.b);
- the particle passes within the camera volume without hitting the sensor, and only part of the photons pass through the mask (this case is also considered "dazzled") (see Fig. 5.1.c).

Currently, the reconstruction algorithm does not utilize the dazzled cameras. They have been excluded using the Monte Carlo truth by verifying if there is an energy deposit inside the cameras. However, when reconstructing events from real data, GRAIN will require a classification that relies only on the data itself. This chapter will present a project that aims to classify cameras as either "non-dazzled" or "dazzled", relying on a data-driven approach. The proposed solution is based on Deep Learning, using a Convolutional Neural Network (CNN). The next sections will discuss the dataset used, the chosen method, and its results.

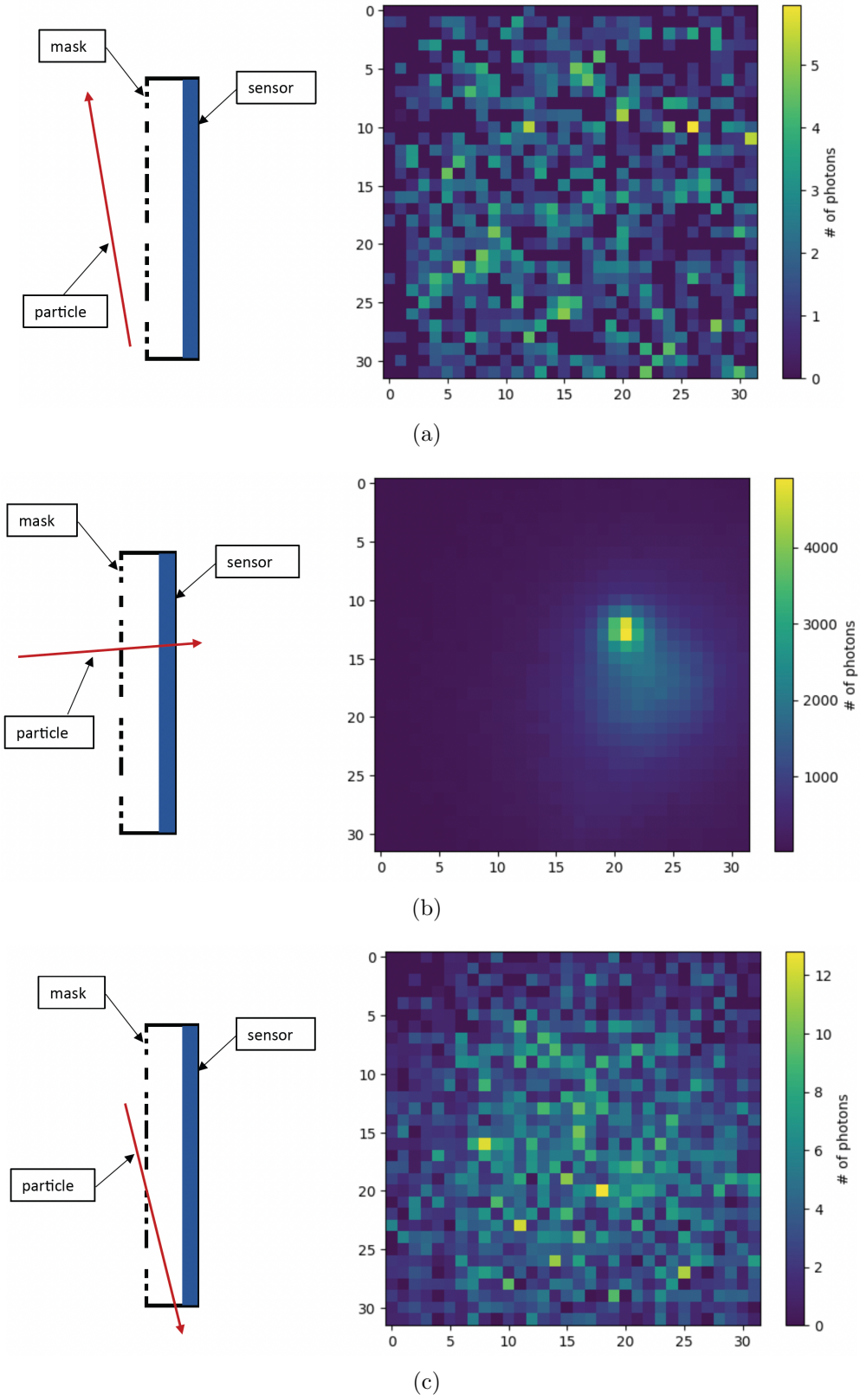

Figure 5.1: (a) non-dazzled camera; (b) dazzled camera; (c) dazzled camera, with an unclear light pattern, each with an example corresponding camera-photon scheme.

5.2 A Deep Learning approach

Deep learning is a subset of machine learning characterized by neural networks. Neural Networks are basically models organized in layers, i.e., a sequence of simple transformations applied to the input data according to the layer's weights [71]. They are commonly used for supervised learning problems, where the model receives in input a set of pairs (X_i, y_i), with $i = 1, ..., N$, and it learns to predict y_i by observing X_i. The input data can be of several types, and in case of a finite set of y_i, the problem will be defined as *classification problem*. The network learns during the training process, where at each step, looking at the *training* dataset, it produces a tentative $\tilde{y}_i$ and compares it to y_i through a loss function. Then, it updates its parameters (the weights of the layers), in order to move towards the minimum of the loss function. In this phase, the performance is monitored on the *validation* dataset. Once the training is completed, the neural network is tested on the separated and unseen *test* dataset.
The primary goal of neural networks is to *generalize* the task on never-before-seen data. A limitation is usually the *overfitting*, which occurs when the network optimally performs on train data but fails on other data.
The network's structure varies depending on the specific problem, and several software libraries allow to implement neural networks. The most used is the *Tensorflow* open source library, together with *Keras*, a wrapper that can work on top of Tensorflow, as done in this case. Further details on the model chosen in this project are discussed in Sec. 5.2.3.

5.2.1 Simulated dataset

We simulated 10 000 neutrino events with the same spectrum of the DUNE beam, divided in 10 files. The detector response was simulated with the configuration described in Chap. 4 These data provide information on the number of photons impinging on each sensor matrix pixel.

The output of the optical simulation contains the MC truth of data, and it will be used to label the data for the CNN training. It is a ROOT file: each camera is a ROOT Tree, and each Tree has some variables organized in TBranches, such as the energy, the space coordinates and momentum components. The variable of interest is the number of photons produced within the camera and detected by the sensor, called *inner photons*.
The simulated data need to be labelled before being passed to the neural network. Let us define, then, the ratio between inner photons and total photons produced by a particle in LAr:

$$r = \frac{N_{\text{inner photons}}}{N_{\text{total photons}}} \tag{5.1}$$

The cameras will be labelled according to the following label criterion:

- **non-dazzled** (ND), if $r < 0.1$,
- **dazzled** (D), if $r \geq 0.1$.

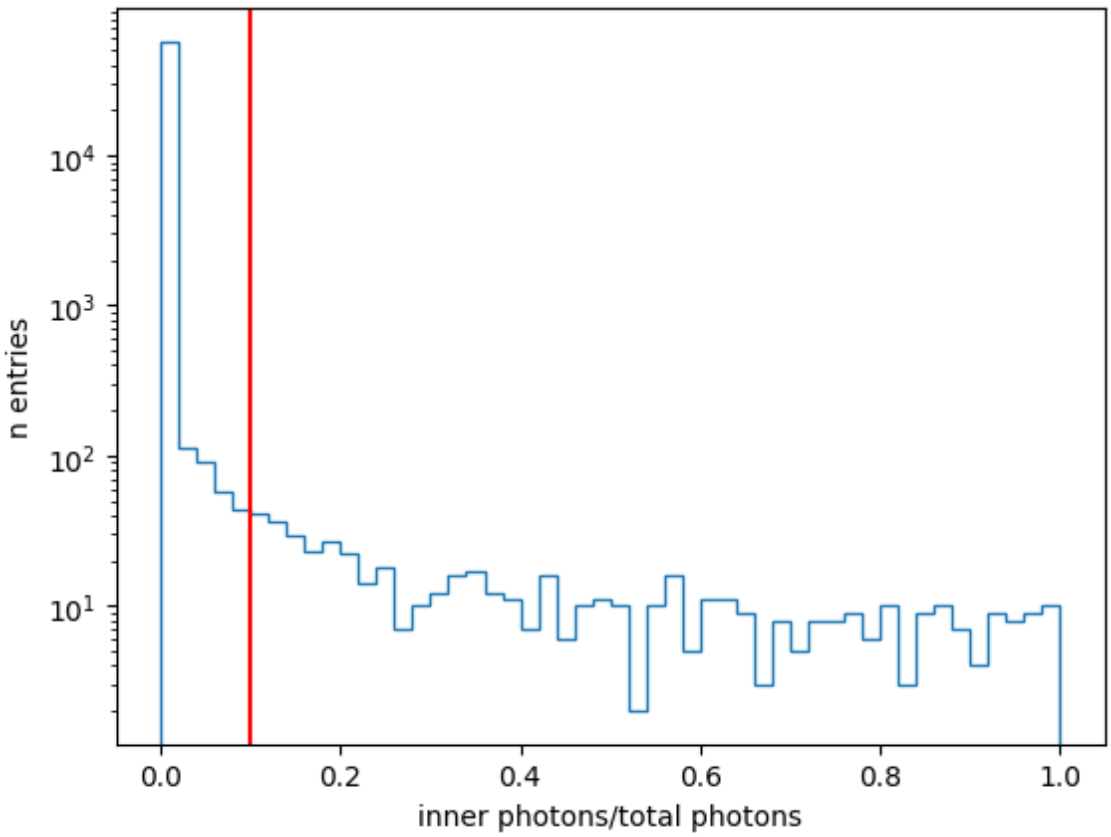

Figure 5.2: Distribution of the ratio between the inner photons and the total photons, with the red line at a value of 0.1.

The absolute number of photons produced within the camera is not always indicative of the dazzling of a camera. Sometimes, in fact, despite a high number of inner photons, the number of photons produced in the rest of the detector can be significantly higher. This can occur in situations such as the third case presented in Fig. 5.1.c, where the particle starts emitting outside the camera and continues in its inner volume. For this reason, we chose a criterion that depends on the ratio between the inner and the total number of photons produced, as presented in Fig. 5.2.

5.2.2 Preprocessing and augmentation

Two files were selected for analysis due to computational constraints, resulting in 120 000 simulated cameras available for use.
First, we applied a cut to esclude the cameras with less than 40 photons, as they do not provide enough information for the track reconstruction. This reduced the dataset by $\sim 21\%$.
The most relevant feature of this dataset, however, is its imbalance towards the non-dazzled cameras, with a percentage of 98.5% ND - 1.5% D. With this kind of data, a neural network would be optimal in finding the non-dazzled cameras, but only because they are in higher amounts. For this reason, the amount of dazzled cameras was enlarged in two ways to re-balance the problem. First, we performed an

augmentation on the dataset by extracting from the remaining eight simulated files, only the dazzled cameras, obtaining a percentage of 91.4% ND - 8.6% D. Then, the dataset was split into train, validation and test datasets, with the scheme 80% - 10% - 10%. In the end, another augmentation was applied on both train and validation datasets, increasing the dazzled percentage up to 48%.

Data augmentation is a technique widely used in the computer vision field with deep learning models. Through this tool, it is possible to generate more data from the existing samples, *augmenting* them by applying random transformations (such as rotation, zoom, flip...) that produce images similar to the real ones [72]. In this way, the model never sees two identical images, reaching a better generalization. Data augmentation is usually used when there are few training samples or when the dataset is imbalanced, as in this case.
The augmentation in this problem is produced applying the transformations of the `RandomFlip`, the `RandomRotation` and the `RandomZoom` layers. They randomly flip (horizontally or vertically), rotate and zoom the image, respectively, according to given options.

After this preprocessing phase, the data are organized as follows:

- training dataset: $\sim 10^6$ images,
- validation dataset: $\sim 10^5$ images,
- test dataset: $\sim 10^5$ images.

5.2.3 CNN Model

When dealing with image classification problems, it is common practice in literature to use Convolutional Neural Networks (CNNs).
CNNs come from studies on the brain's visual cortex, and, since the '80s, they have been used for image recognition. However, in the last decade, they have undergone a notable improvement. They rely on *convolutional layers*, which are the building blocks of a CNN. The artificial neurons, i.e., the computational nodes of the network, in the first convolutional layer are connected only to pixels in their receptive fields. Each neuron, then, is connected to other neurons positioned inside a small area, and so on (see Fig. 5.3). In this way, the network can extrapolate low-level features from the first layer, assembling them into higher-level features in the subsequent layers [71].

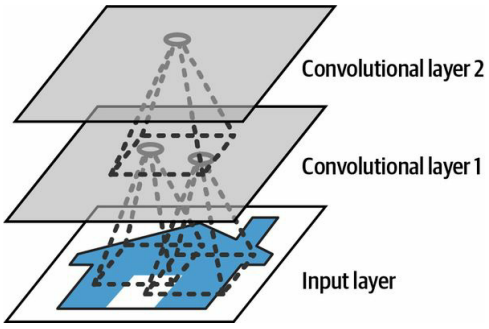

Figure 5.3: CNN layers with rectangular local receptive fields. [72]

The convolution is done by a *kernel*, usually a 3×3 matrix, that slides over the input image, considered as a 3D matrix (height, width, channels). According to a step called *stride*, it stops at every possible location, doing element-wise matrix multiplication. The values pass through the activation function and then are put into the feature map.

The *activation function* is a fundamental parameter for the network layers, as it returns the output of a node inside a layer. Usually, these are non-linear functions: introducing non-linearity allows the network to perform more complex tasks.

Particular attention is given to the edges of the input image: to avoid a loss of information from that region maintaining the input dimensions, usually *padding* operation is applied. Shrinking the input image with no padding would lead to low-dimensional representations without some relevant information. However, dimensionality must be reduced to improve the training time and to fight overfitting. The *pooling layer* accomplishes it, downsampling each feature map independently, reducing the height and the width but not the depth (see Fig. 5.4).

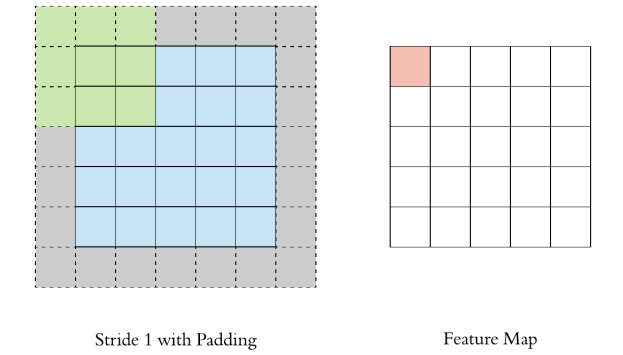

(a)

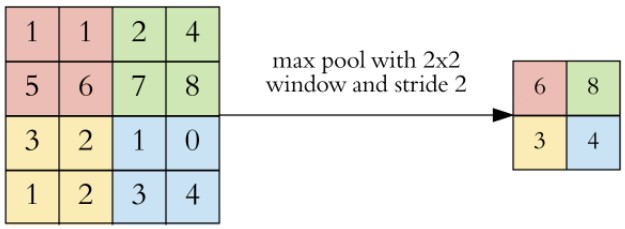

(b)

Figure 5.4: (a) example of padding application with stride 1; (b) example of application of a MaxPooling layer with 2×2 kernel and stride 2. This layer reduces the dimensions by extracting the maximum value in the kernel selection.

The CNN model chosen in this case is presented in Fig. 5.5.

It takes in input the images with dimensions [32,32,1], processing them with four convolutional layers `Conv2D`, with filters' sequence 128-64-32-16. In each layer, the kernel has dimensions 3×3, the activation function is ReLU (see Fig. 5.6.a), and the padding option is active. After each convolutional layer, there is a `MaxPooling2D` layer which downsamples the feature map with a pooling window size 2×2. The `Flatten` layer reduces the feature map from [2,2,16] to a 1D array of 64 elements. At this point, the feature map passes through four `Dense` layers, with the ReLU

Layer (type)	Output Shape	Param #
conv2d (Conv2D)	(None, 32, 32, 128)	1280
max_pooling2d (MaxPooling2D)	(None, 16, 16, 128)	0
conv2d_1 (Conv2D)	(None, 16, 16, 64)	73792
max_pooling2d_1 (MaxPooling2D)	(None, 8, 8, 64)	0
conv2d_2 (Conv2D)	(None, 8, 8, 32)	18464
max_pooling2d_2 (MaxPooling2D)	(None, 4, 4, 32)	0
conv2d_3 (Conv2D)	(None, 4, 4, 16)	4624
max_pooling2d_3 (MaxPooling2D)	(None, 2, 2, 16)	0
flatten (Flatten)	(None, 64)	0
dense (Dense)	(None, 128)	8320
dense_1 (Dense)	(None, 64)	8256
dense_2 (Dense)	(None, 32)	2080
dense_3 (Dense)	(None, 16)	528
dense_4 (Dense)	(None, 1)	17

Total params: 117361 (458.44 KB)
Trainable params: 117361 (458.44 KB)
Non-trainable params: 0 (0.00 Byte)

Figure 5.5: CNN model architecture.

activation function, that are fully connected to the nodes of the previous layer. The regularization option present here is a technique to mitigate overfitting: it constrains the network's weights to take only small values, making the weight distribution more regular by adding a cost to the loss function when it is associated with large weights. In particular, in the *L2 regularization*, the cost added is proportional to the square of the value of the weight coefficients [71]. At last, a `Dense` layers return the output of the model, using a sigmoid activation function (see Fig. 5.6.b).

In Tab. 5.1, the main parameters of the model are presented. The batch size

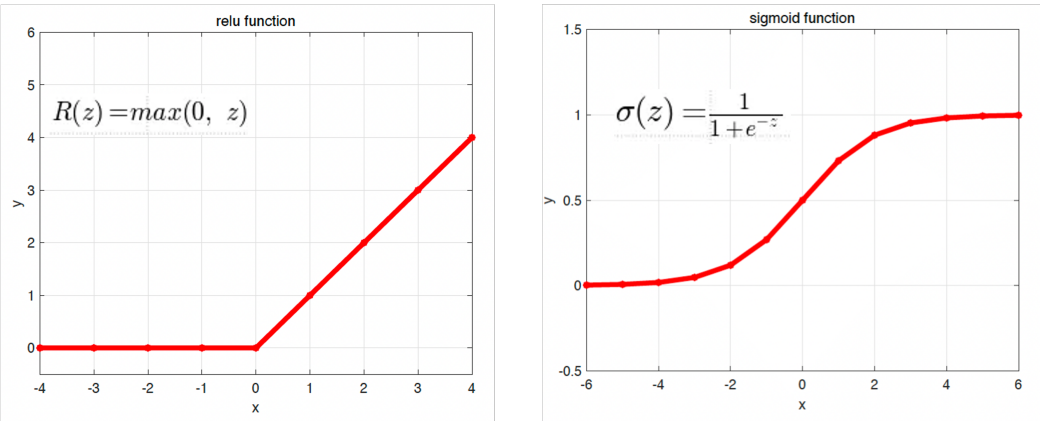

(a) (b)

Figure 5.6: (a) Rectified Linear Unit (ReLU) function and (b) sigmoid function used in the CNN model, with the corresponding analytic expressions. [73]

Model parameters	
batch size	`32`
input shape	[32,32,1]
number of epochs	10
metric	`F1Score`
loss function	`BinaryCrossentropy`
callback	`EarlyStopping`
optimizer	`SGD`

Table 5.1: Parameters of the model.

(the number of training samples used in one iteration) is set to 32, as is common practice in machine learning. The input shape is [32,32,1] because the cameras have 32×32 pixels and one colour channel. The number of epochs, where an *epoch* is each iteration over all the training data, is fixed to 10, nevertheless the `EarlyStopping` callback option allows the model to stop the training when there are no more improvements in the learning process. Given that this is a binary classification problem, the `BinaryCrossentropy` is a well-suited loss function. Furthermore, to evaluate the model by its capacity to reduce the number of misclassifications, the `F1Score` metric is used. It considers both the precision and the recall and is defined as:

$$F1 = 2 \cdot \frac{precision \cdot recall}{precision + recall} = \frac{TP}{TP + \frac{1}{2}(FP + FN)} \tag{5.2}$$

where $precision = \frac{TP}{TP+FP}$ and $recall = \frac{TP}{TP+FN}$. In classification problems, TP indicates true positives (well-identified D cameras), FP false positives (ND cameras classified as D), FN false negatives (D cameras classified as ND) and TN true negatives (well-identified ND cameras).
The Stochastic Gradient Descent `SGD` [74] optimizer is chosen.

5.3 Results

After preprocessing the data and building the CNN architecture, the model was trained for several epochs managed by the `EarlyStopping` callback. During the training, the `F1Score` metric and the loss function have been monitored for both the training and the validation datasets. The score increases approaching ~ 1, while the loss decreases to ~ 0.1, as Fig. 5.7 shows. The better value of the validation score and loss is probably due to the regularization option in the model, which only acts on the training set and increases the loss function value.

Once the training was completed, the model was applied to the test dataset to evaluate its performance on never-seen-before data. The confusion matrix is shown in Tab. 5.2. Although the predicted ND cameras include a part of true D, the purity of the dataset increases after the CNN classification. At the beginning the dataset purity is $p_i = \frac{TN+FP}{N_{totcameras}} \sim 0.91$; after the algorithm processing, it reaches $p_f = \frac{TN}{TN+FN} \sim 0.98$. This means that there is an improvement since the relative abundance of D cameras in the dataset is reduced. The corresponding `F1Score` is ~ 0.85.

		Predicted labels	
		ND	D
True labels	ND	TN: 9113	FP: 56
	D	FN: 192	TP: 716

Table 5.2: Confusion matrix obtained from this model.

As explained at the beginning, this deep-learning algorithm should be applied before the reconstruction step of Fig. 4.1. It has, indeed, to accomplish the rejection of the D cameras, that up to now has been done with MC truth. To observe the effects of this MC truth exclusion, in Fig. 5.8 we present the emitted photons

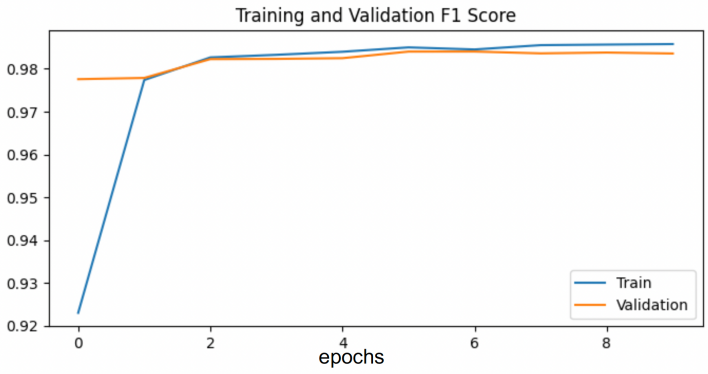

(a)

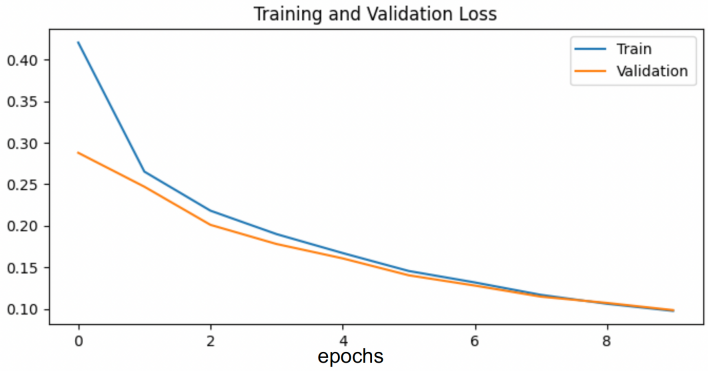

(b)

Figure 5.7: Trends of (a) `F1Score` metric and (b) loss function over 10 epochs for training and validation datasets.

estimate distribution per voxel performed for an event were the proton crosses a camera, including and excluding the D one.

Further improvements

Despite the positive results, further steps can be taken to improve the model's performance. It must be noted that the data are not so clearly distinguishable between dazzled and non-dazzled since sometimes even a D-labelled camera looks like an ND-one, or vice versa, making the task very complex. One possible improvement is to redefine the labelling criterion by defining three categories. In addition to distinguishing non-dazzled cameras, further differentiation can be made among dazzled cameras by considering those where the particle directly hit the sensor and those where the particle emitted photons within the camera without hitting the sensor.

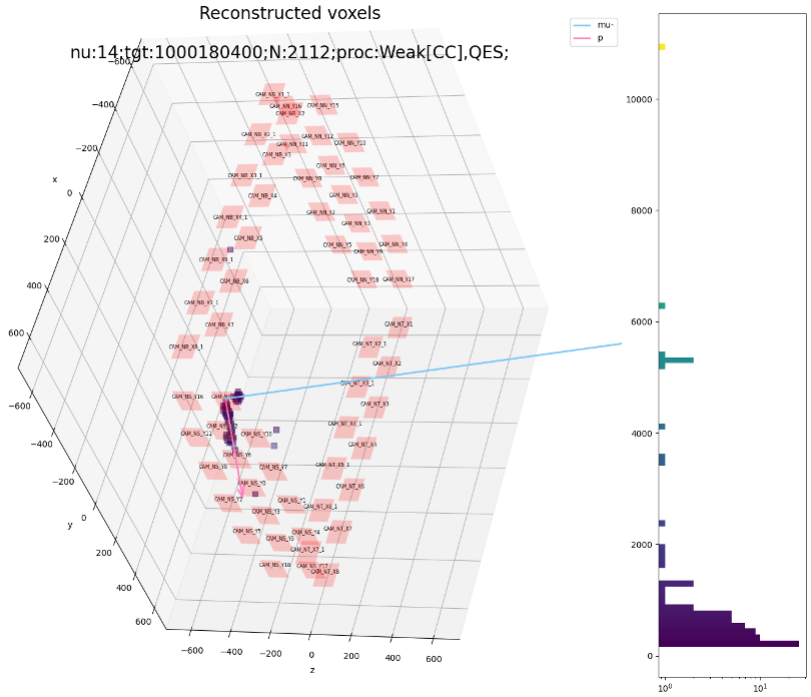

(a)

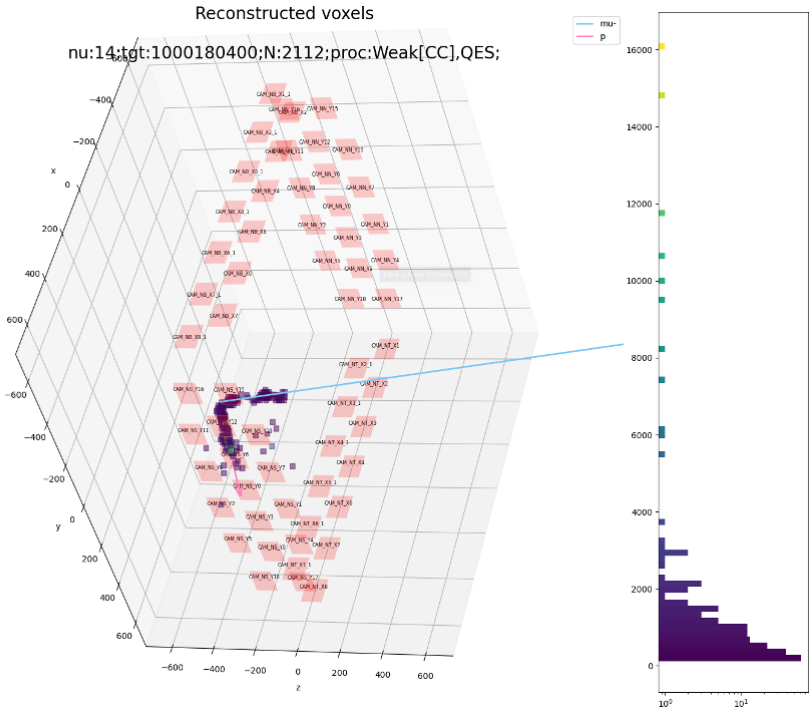

(b)

Figure 5.8: (a) 3D event reconstruction with all the cameras and (b) excluding the dazzled one. The pink and blue arrows represent the true directions of the proton and of the muon, respectively. The red rectangles correspond to the cameras. The score values of the selected voxels in the reconstruction distribution are shown in the histogram on the right. Note that the muon becomes visible in the second image after filtering the dazzled camera that was hit by the proton.

Chapter 6

Reconstruction of tracks and fitting

In this chapter we present the process of track reconstruction for a selection of neutrino charge-current quasi-elastic (CCQE) interaction events in GRAIN. We show the several algorithms applied to the distribution of photon sources in order to estimate the particle directions. As a final step, we discuss the residuals between these reconstructed quantities and the MC-truth ones to assess the performance of the algorithm.

6.1 Reconstruction analysis process

The simulation process described in Section 4 produces a 3D reconstruction of the voxel scores within each voxel. The voxel side is 12 mm. This output is obtained by applying the ML-EM algorithm, with 500 iterations. Additionally, to avoid artifacts of the algorithm, we excluded the regions of the volume within 5-voxel distance from the mask faces. An example is shown in Fig. 6.1.

The reconstruction analysis process of an event is accomplished by first selecting voxels with score above a fixed threshold and then implementing the DBSCAN clustering algorithm [75] on the distribution of voxels. The subsequent step involved the use of a *local principal curve* algorithm [76] to find a set of points. From these points, we identified the collinear ones and associated them to their corresponding track using the *Hough transform* [77]. In the end, we applied a linear fit to these points, determining the directions of the particles produced.

6.2 Track finding

In the following, we discuss the methods used to find the track points.

Score-based voxel selection

The aforementioned simulation output provides the estimate of the number of photons emitted in each voxel, called *score*. However, this output features a large background, as many voxels present a non-zero voxel score. This non-zero background makes it difficult to identify the true path of the particles.

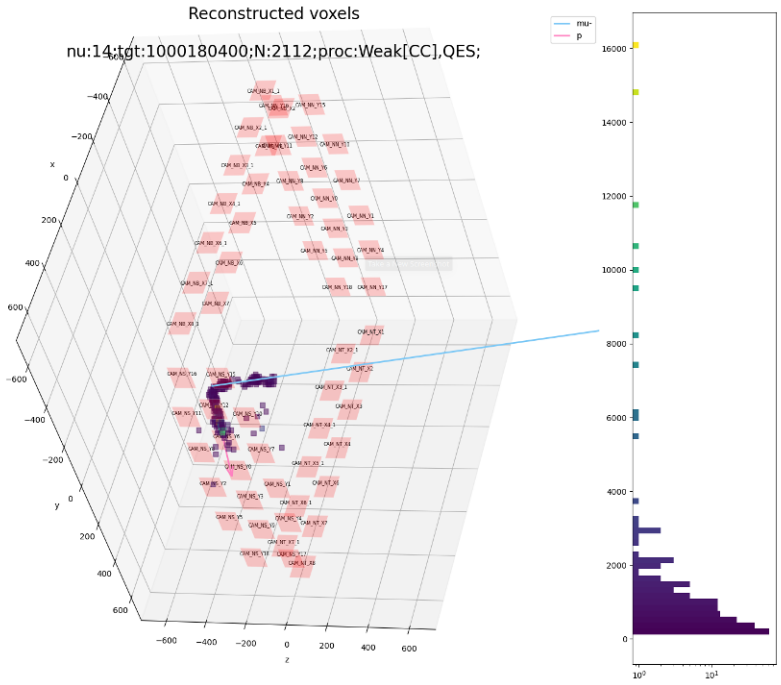

Figure 6.1: Example of the 3D reconstruction of the voxel scores, with the pink and blue arrows representing the true directions of the proton and of the muon, respectively. The red rectangles correspond to the cameras. The score values of the selected voxels in the reconstruction distribution are shown in the histogram on the right.

To obtain a sharper voxel distribution without losing too much information, we applied a cut on the voxels with a score less than 100, that corresponds to less than the 0.5% of the average maximum, setting them to 0. Fig 6.2 illustrates an event before and after the application of this cut.

Clustering algorithm

At times, the events may present clusters due to the presence of multiple tracks. This is particulary evident in case of neutral particles: as they do not release energy, we see only the track of their decay products. Furthermore, sometimes, the event reconstruction does not give a set of voxels with uniform score along the particle tracks. This, together with the application of the cut, leads to a further formation of disconnected clusters of voxels belonging to the same track.
Therefore, to identify the necessary clusters for our reconstruction process while discarding isolated voxel caused by reconstruction artifacts, we utilized the DBSCAN algorithm.

The Density-Based Spatial Clustering for Applications with Noise (DBSCAN) algorithm [75] is an unsupervised learning clustering technique based on the assumption that clusters are dense regions in space, separated by regions of lower density. This algorithm assigns each point to a specific cluster by looking at the density of the points around it. It requires two input parameters: *epsilon* ϵ, that is the radius of the circle to be created around each point to check the density, and *minPoints*, that is the minimum number of points required inside that ϵ-circle for that data

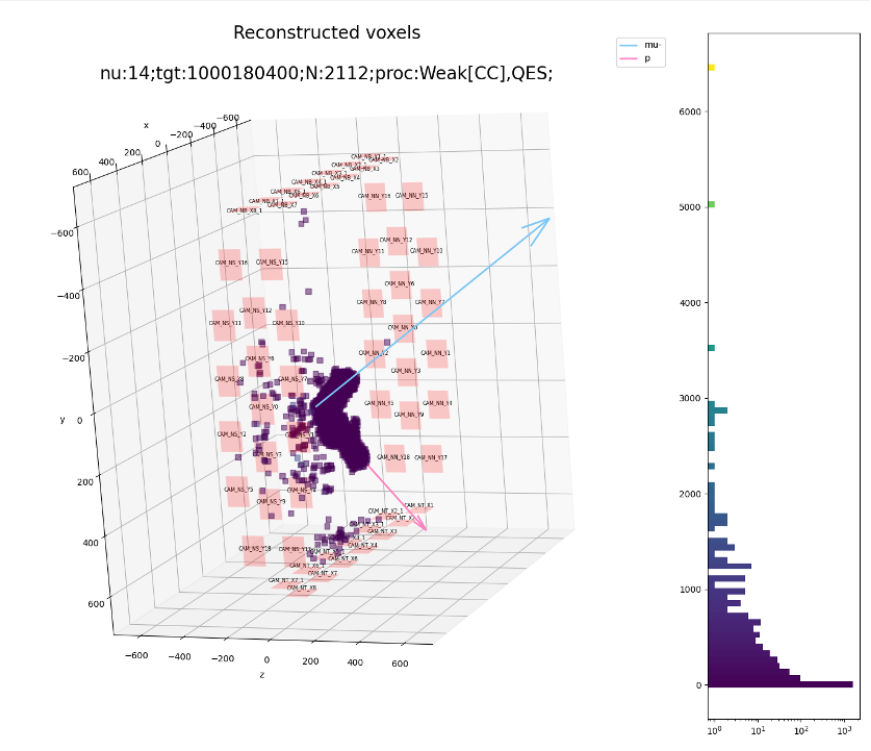

(a)

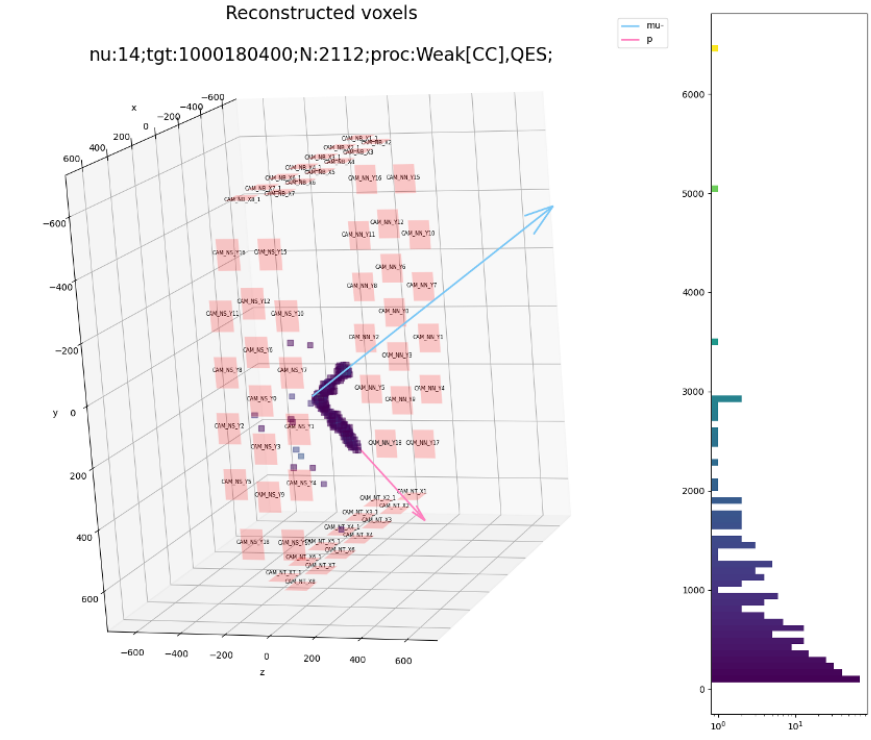

(b)

Figure 6.2: (a) Voxel distribution with a score above 0.1; (b) Voxel distribution with a score above 100. The pink and blue arrows represent the true directions of the proton and of the muon, respectively. The red rectangles correspond to the cameras. The score values of the selected voxels in the reconstruction distribution are shown in the histogram on the right.

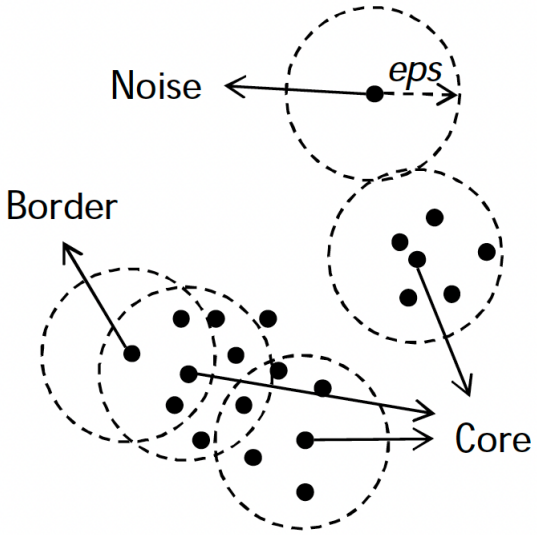

Figure 6.3: Example of DBSCAN application with $minPoints = 5$. [78]

point to be classified as a Core point. Hence, as seen in Fig. 6.3, the points are clusterized as:

- **Core** point, if the ϵ-circle contains at least a number of points equal to *minPoints*;
- **Border** point, if the ϵ-circle contains a number of points less than *minPoints*;
- **Noise** point, if there are no points inside ϵ-circle.

DBSCAN algorithm can be applied to 3D data, as in our case. The parameters chosen in our application are $minPoints = 6$, as suggested in [79] and $\epsilon = 36$ mm, which corresponds to 3 times the voxel size.

LPC algorithm and refinement

Once all the clusters of voxels have been found, we consider the centre of each voxel belonging to the same cluster. Hence, the problem became finding the best curve passing through these points. This is a widely-discussed issue in literature, with many proposed methods. The principal component analysis (PCA) [80] and, its natural extension, the principal curves algorithm [81], are common tools. A principal curve is defined as one-dimensional smooth curve that pass through the "middle" of a d-dimensional data set.
In our application, we have chosen the *local* principal curve algorithm, that is a variant of the principal curve. It follows a "bottom-up" approach, by considering at every step the data in the local neighbourhood of the considered point. In the end, it finds a series of local centres of mass that form the *local principal curve*. The main advantage is that it is more flexible and less computationally expensive [82] with respect to the principal curve algorithm.

The *ℓpc* algorithm [76] is a method based on the *mean shift* procedure, i.e., a process that moves a point to the local mean of the data around this point.

In our case, the algorithm receives in input a set of points $X_i(x, y, z)$, and, choosing an initial location u, it finds the so-called *ℓpc* points, following this iterative procedure:

1. computes the local centre of mass:

$$m\left(u_\ell\right) \equiv u_\ell + s\left(u_\ell\right) \tag{6.1}$$

2. finds the next local neighbourhood location:

$$u_{\ell+1} = m(u_\ell) + t \times \gamma_\ell \tag{6.2}$$

In the first step, chosen a location u, the algorithm computes the local centre of mass by "moving" the location towards a denser region of the data space. This is done by adding the so-called *mean shift*, defined as:

$$s(u) = \frac{\sum_{i=1}^{N} w_i(u)(X_i - u)}{\sum_{i=1}^{N} w_i(u)} \tag{6.3}$$

where $w_i(u)$ are the weights, which determine the size and the shape of the local neighbourhood at the chosen location u. Commonly, they are described through the Gaussian density function:

$$w_i(u) = \frac{Q_i}{(2\pi)^{3/2}h^3} \exp\left\{-\frac{1}{2h^2}\left(X_i - u\right)^T\left(X_i - u\right)\right\} \tag{6.4}$$

where Q_i, in our case, is the score for the voxel centre i, and h is a constant bandwidth parameter that steers the size of the local neighbourhood. If this step is repeated iteratively, computing naively $m_{\ell+1} = m_\ell + s(m_\ell)$, the algorithm can easily find the convergence at a local mode u_m where $s(u_m) = 0$. Despite this can be an appealing property, it has the drawback of getting trapped in the local modes without moving beyond them. For this reason, it is necessary to introduce the second step presented in Eq. 6.2.

In the second step, given the local mean $m(u_\ell)$, the *ℓpc* algorithm finds the next local neighbourhood location by moving one step t in the direction defined by the normalised eigenvector $\gamma(u)$ that corresponds to the largest eigenvalue of the local symmetric 3×3 covariance matrix, defined as:

$$\Sigma(u) = \frac{1}{\sum_{i=1}^{N} w_i(u)} \sum_{i=1}^{N} w_i(u)(X_i - u)(X_i - u)^T \tag{6.5}$$

Actually, γ_ℓ is multiplied by an angle penalization term $a = |\cos\phi|^\alpha$, with $\alpha = 2$ usually, to reduce the probability of the algorithm deviating too much from the principal direction of the points. Hence, the computation of γ_ℓ becomes:

$$\gamma_\ell := a\gamma_\ell + (1 - a)\gamma_{\ell-1} \tag{6.6}$$

Then, the set of *ℓpc* points consists of the series of local centres of mass $m(u_\ell)$, $m(u_{\ell+1})$, ... The procedure starts with $\ell = 0$ from a given point $u = m_0$, which usually is taken as the nearest hit to the energy-weighted centroid of all the hits.

Then, it is repeated iteratively until the required number of ℓpc points N_p is gained, or it reaches the convergence, i.e., the path length along the curve increases no more. Quantitatively, we say that the algorithm converges if:

$$R = \frac{\lambda_\ell - \lambda_{\ell-1}}{\lambda_\ell + \lambda_{\ell-1}} < R_{thr} \tag{6.7}$$

where $\lambda_\ell = \lambda_{\ell-1} + |m(u_\ell) - m(u_{\ell-1})|$ and $\lambda_0 = 0$.
The algorithm starts finding the ℓpc points in one direction, and when it has reached convergence or the number of points is $\frac{1}{2}N_p$, it restarts in the other direction, changing the sign of γ_ℓ.
The parameters chosen for our application are summarized in Tab. 6.1:

ℓpc **parameters**	
N_p	200
R_{thr}	10^{-3}
h	30 mm
t	55 mm
t_{min}	12 mm

Table 6.1: Parameters of the ℓpc algorithm.

As suggested in the paper [76], N_{max} was set to 200, the bandwidth h and the stepsize t were chosen with a similar value, with a larger t since it is penalized by the penalization term. The value of R_{thr} is chosen to prevent the presence of many close ℓpc points towards the edges of the track. The minimum step parameter t_{min} is introduced in our application to avoid ℓpc points being too close to each other. This means that a point is considered an "ℓpc point" only if the distance from the previous ℓpc point is larger than the minimum step.

We processed each cluster of voxels with the ℓpc algorithm. However, we observed that it fails to add ℓpc points on the ends of the tracks. In order to address this issue, we performed a refinement to the ℓpc algorithm. It consists in a reapplication of the ℓpc algorithm to the voxel centres where we have no ℓpc points. These "remaining" voxel centres are selected with the following criterion (see Fig. 6.4). Consider an ideal sphere around each ℓpc point: if the voxel centre is inside at most two sphere it is reprocessed; otherwise not. Fig. 6.5 showed an event after the application of the discussed algorithms.

Hough transform

To determine the tracks of the particles, we grouped the ℓpc points obtained. At a first approximation, the particles in GRAIN go along a straight track since their curvature radius is not easily appreciable considering the cluster size and the momentum of the particles produced by the neutrino interactions. Hence, we can assign the ℓpc points to a particular track by looking for points on the same line, called "collinear" points. For this reason, we applied the *Hough transform*.

The Hough transform [77] is commonly used in computer vision to find straight lines. This problem was originally solved by Hough [83] as a collinear-points detection method, and then reframed by Rosenfeld [84] with a mathematically equivalent

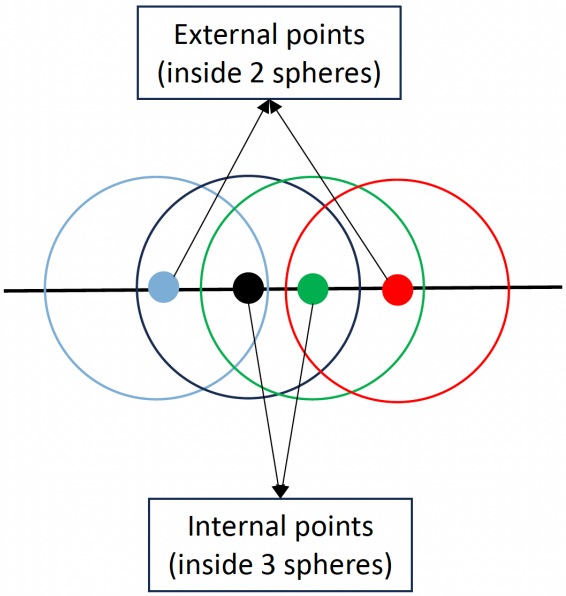

Figure 6.4: Simple example of selection criterion for the ℓpc refinement.

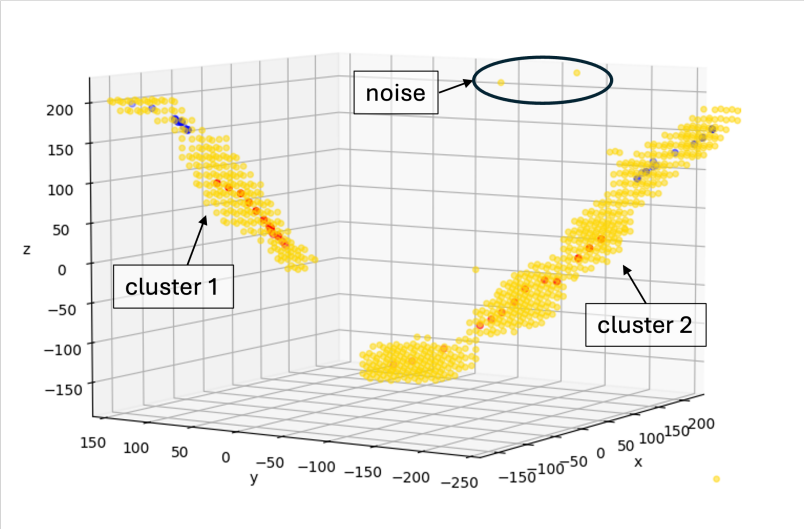

Figure 6.5: CCQE $\mu - p$ event, with two clusters and the noise found by DBSCAN. The red ℓpc points come from the first application of the ℓpc algorithm; the blue ones from the second application.

problem of finding concurrent lines. It is based on the fact that a set of straight lines in a x–y plane can be parametrized, with the so-called *normal parametrization*, by the perpendicular distance ρ from the origin and the angle θ that ρ forms with the horizontal axis, as shown in Fig. 6.6.

The line can be described by the following equation:

$$x \cos\theta + y \sin\theta = \rho. \tag{6.8}$$

Given a set of points $\{(x_1, y_1), ..., (x_n, y_n)\}$, each set of lines passing through a point (x_i, y_i) corresponds to a sinusoidal curve in the $\theta - \rho$ plane defined by:

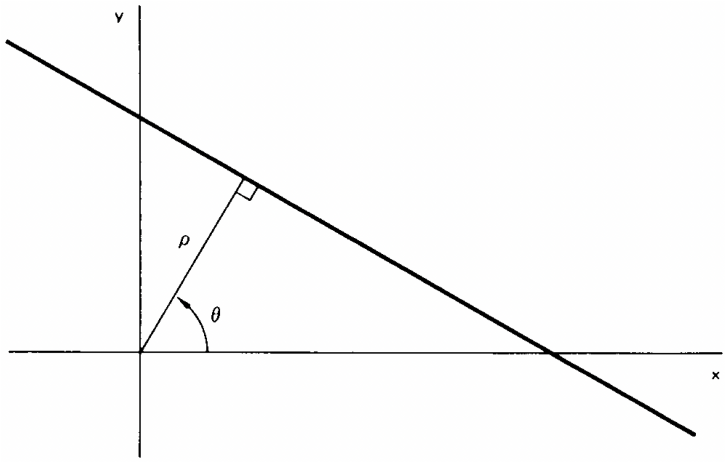

Figure 6.6: The normal parameters for a line in $x - y$ plane. [77]

$$\rho = x_i \cos\theta + y_i \sin\theta. \tag{6.9}$$

Hence, points on the same line share the same values of ρ and θ. This results in the intersection for these (ρ, θ) values between the sinusoidal curves. These parameters define the line that passes through the collinear points[1]. If $\theta \in [0, \pi]$ the parameters are unique.

Practically, this is done by computing a discrete accumulator, that is a 2D array with a fixed resolution on θ and ρ and dimensions $0 \leq \theta < \pi$ and $-R \leq \rho < R$, where R is the maximum length that ρ can assume. The parameter resolution will affect the outcome: a finer discretization will improve the resolution but, on the other hand, will give problems of clustering entries that correspond to nearly collinear points.
For each point (x_i, y_i) in the x–y plane, the corresponding curve is added to the accumulator by increasing the count in each cell along the curve. This means that a cell records the total number of curves passing through it. Hence, the number of collinear points can be inferred by the counts in a specific cell.

In this application, the Hough transform algorithm has been applied to the 2D projection of the 3D reconstruction on z–x and z–y planes for computational reasons. The accumulator has been built with dimensions $0 \leq \theta < \pi$ and $-736 \leq \rho < 736$ and with ρ binning of 36 mm and θ one of 5°.
The value of R is set to the diagonal of the rectangle formed by the two semiaxes of the GRAIN ellipse.
In the end, we determined the local maxima through the `peak_local_max` function of *scikit–image* package. It slides over the image finding a maximum within a region of $(2 \cdot min\_distance + 1)$ if the value of the pixel is higher than a fixed threshold, where *min_distance* is the minimal allowed distance separating peaks. We chose for our application a *min_distance* of 7 bins and a threshold equal to 35% of the number of ℓpc points. The reason behind this choice is that the number of collinear points strongly depends on the total number of ℓpc points. Furthermore, since we are dealing only with two-track events, we imposed a limit of 2 maxima to be found.

[1]The point collinearity is defined according to the bin size of the Hough transform.

An example of an accumulator, with the determined maxima is shown in Fig. 6.7.

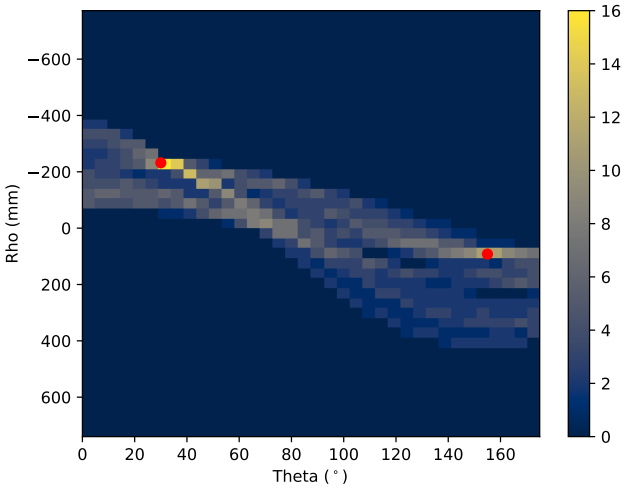

Figure 6.7: Example of Hough accumulator, with the points in red corresponding to the maxima.

Track point association and fitting

With the values of ρ and θ found by the Hough transform, we determined the projections of the track candidates in both z–x and z–y planes. Hence, we tested all the possible combinations (at most 4) of the two projections, in order to match them in the 3D space. As a final step, we associated all the ℓpc points distant less than 100 mm from one of the lines to the closest one, forming then the collinear clusters. We chose this distance threshold by looking at the minimum distances of the ℓpc points to the closest line of all the events of the sample, shown in Fig. 6.8

Once obtained the collinear ℓpc points, we applied a least squares linear fit in the 3D space to each collinear cluster with more than 4 ℓpc points. This was necessary to possibly improve the fit.

Direction reconstruction method

From the linear fit we obtained the reconstructed directions of each particle. Since we have always two true tracks, and we have no information on which particle is reconstructed, we assume that the fitted track is the one with the minimum angle.

6.3 Analysis

We performed the analysis on a selection of CCQE μ–p events from ten files produced as output of the simulation chain. From 10 000 generated events, we considered only the CCQE ones with a muon and a proton. Among these, we selected the events with the vertex inside the fiducial volume and with tracks at least 10-cm long.
We processed all these events with the track finding algorithm. However, we did not

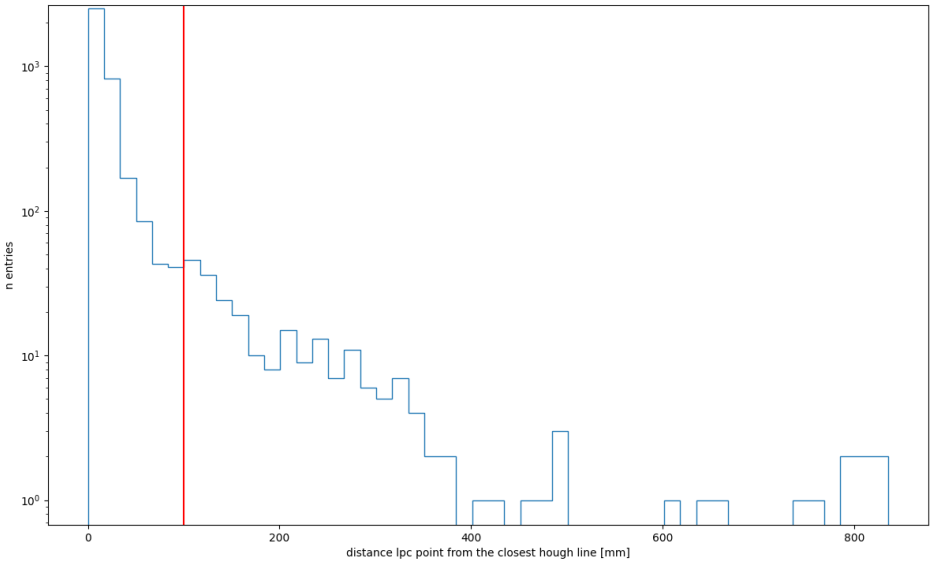

Figure 6.8: Minimum distance of every ℓpc point from the closest "Hough" line, with the red line at a distance of 45 mm.

detect two tracks for every event. This could be due to the reconstruction of the voxel distribution, which sometimes is not sufficient to allow an optimal application of the ℓpc algorithm, but also to the Hough transform, which occasionally struggles to find the track candidates, with a subsequent lack of collinear points associated. For this reason, we applied the linear fit only to the collinear clusters with more than 4 ℓpc points, as aforementioned. This results in a substantial loss of efficiency.

We reconstructed the directions of all the fitted collinear clusters. Then, we compared it with the MC one, computing the angle, to test the performance of the reconstruction process. The angle difference distribution is presented in Fig. 6.9.

Data are fit with a Rayleigh distribution (related with the χ^2 distribution with two degrees of freedom). The best estimate of the Rayleigh scale parameter is $\sigma = 2.5°$ and this corresponds to the angular resolution of the reconstruction process.

As mentioned earlier, the reconstruction of the μ–p vertex is not always possible. Therefore, we evaluated the performance of the reconstruction algorithm by computing the distance between the true vertex and the reconstructed direction. The distribution, shown in Fig. 6.10, has a most probable value of 19 ± 1 mm.

Even in those cases where only one track can be reconstructed, the impact parameter with the vertex of the single reconstructed track is reasonably small.

6.4 Possible improvements

The obtained results in the angular and impact parameter are sufficient to achieve track matching with other SAND subdetectors in terms of resolution. However, the track finding efficiency needs to be improved. An insufficient number of ℓpc points may result from a non-optimal quality of the reconstructed voxel distribution, since

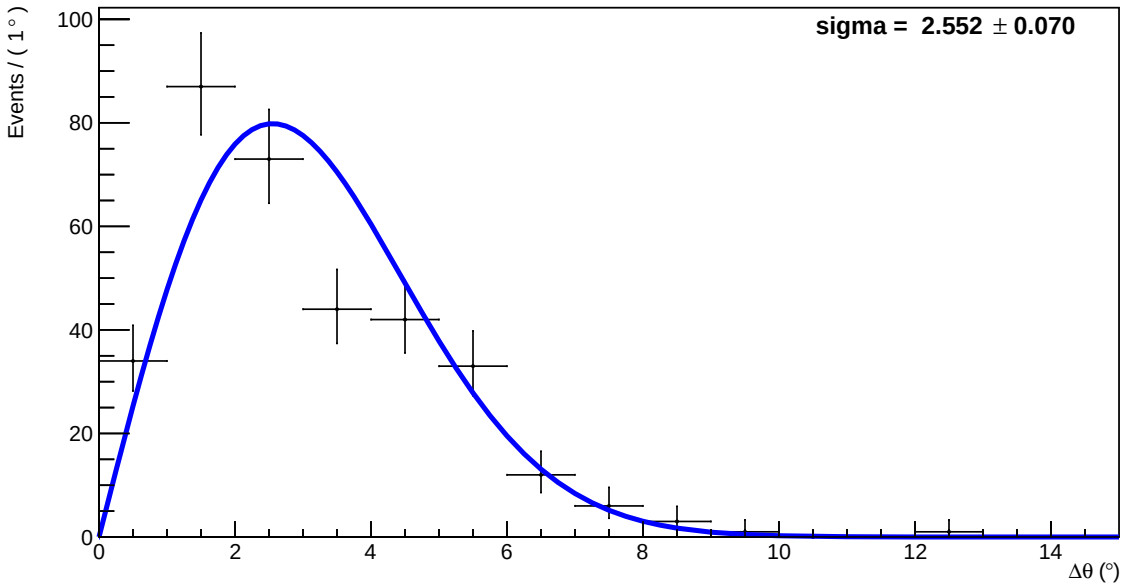

Figure 6.9: Distribution of the angles between the reconstructed and the MC-truth directions, with the fit line in blue.

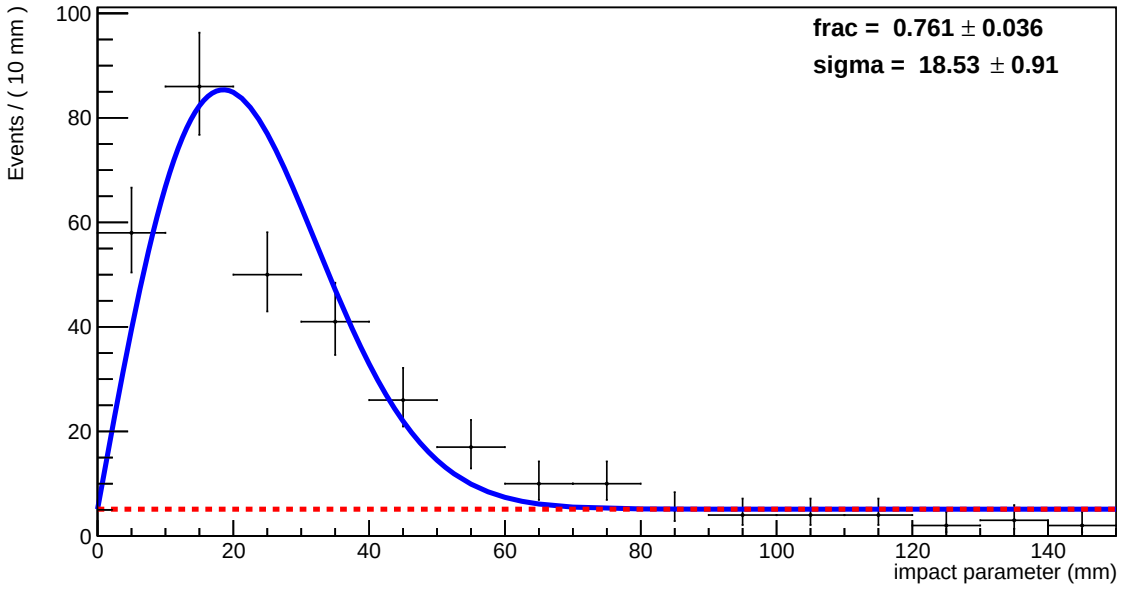

Figure 6.10: Closest distance between the true vertex and the reconstructed track, with the fit line in blue.

the track of the particle that releases less energy in argon (the muon in most cases) is not always reconstructed in its entirety. The *ℓpc* algorithm as well may not find a number points that well-approximates the track. Improvements can be achieved with systematic studies on the *ℓpc* parameters, possibly eliminating the need for the refinement process. Moreover, the Hough transform often struggles to identify the track candidates. Its performance could be improved by moving to a single 3D accumulator in spite of its significant computational cost. Another possible improvement can be pursued by a preliminar implementation of a principal component analysis

(PCA) that identifies the plane that contains both the tracks. Projecting the event in the plane where it has the maximum width, making the identification through the Hough transform more efficient.

Conclusions

As part of the SAND apparatus of the DUNE Near Detector complex, the GRAIN detector will play an important role in the characterization of the neutrino-Ar interactions. In order to perform studies on the feasibility of the GRAIN sub-detector, a detailed reconstruction and simulation chain has been developed.

In this thesis I assessed the performance of a track finding algorithm for the reconstruction of charged-current quasi-elastic interaction in GRAIN, with a muon and a proton in the final state.

First, to deal with the presence of dazzled cameras, caused by scintillation photons emitted between the mask and the sensor, I applied a filtering algorithm to the data to keep only the non-dazzled ones. To this end, I implemented a convolutional neural network. I tested it on $\sim 10^5$ images and it reached a `F1Score` of ~ 0.85. This led to an increase of the purity of the dataset: from an initial value of $p_i = 0.91$ I obtained a final purity of $p_f = 0.98$, substantially reducing then the presence of the dazzled cameras. Further steps can be taken to improve the CNN performance, such as the addition of a third class to represent the intermediate light emission topology.

The most prominent result of this thesis is the study and optimization of the track reconstruction applied to the photon source distribution. The reconstruction is based on a sequence of algorithms which, starting with the application of voxel clustering, and continuing with local principal curve, Hough transform and finally fitting. This allowed me to obtain the direction of the particles with an angular resolution of 2.5° with respect to the MC truth and an impact parameter less than 20 mm from the true vertex position.

The obtained results in the angular and impact parameter are sufficient to achieve track matching with other SAND sub-detectors in terms of resolution. Future improvement should focus on the track finding efficiency.

Bibliography

[1] W. N. Cottingham and D. A. Greenwood. *An Introduction to the Standard Model of Particle Physics*. 2nd ed. Cambridge University Press, 2007. DOI: 10.1017/CBO9780511791406.

[2] R. L. Workman et al. "Review of Particle Physics". In: *PTEP* 2022 (2022), p. 083C01. DOI: 10.1093/ptep/ptac097.

[3] Samoil Bilenky. "Bruno Pontecorvo and Neutrino Oscillations". In: *Advances in High Energy Physics* 2013 (Jan. 2013). DOI: 10.1155/2013/873236.

[4] John N. Bahcall and R. Davis. "Solar Neutrinos - a Scientific Puzzle". In: *Science* 191 (1976), pp. 264–267. DOI: 10.1126/science.191.4224.264.

[5] A. Bellerive et al. "The Sudbury Neutrino Observatory". In: *Nuclear Physics B* 908 (2016). Neutrino Oscillations: Celebrating the Nobel Prize in Physics 2015, pp. 30–51. ISSN: 0550-3213. DOI: https://doi.org/10.1016/j.nuclphysb.2016.04.035. URL: https://www.sciencedirect.com/science/article/pii/S0550321316300736.

[6] Ettore Majorana. "Teoria simmetrica dell'elettrone e del positrone". In: *Il Nuovo Cimento (1924-1942)* 14 (1937), pp. 171–184. DOI: 10.1007/BF02961314. URL: https://doi.org/10.1007/BF02961314.

[7] Carlo Giunti and Chung W. Kim. *Fundamentals of Neutrino Physics and Astrophysics*. Oxford University Press, Mar. 2007. ISBN: 9780198508717. DOI: 10.1093/acprof:oso/9780198508717.001.0001. URL: https://doi.org/10.1093/acprof:oso/9780198508717.001.0001.

[8] Erica Andreotti et al. "MARE, Microcalorimeter Arrays for a Rhenium Experiment: A detector overview". In: *Nuclear Instruments and Methods in Physics Research Section A: Accelerators, Spectrometers, Detectors and Associated Equipment* 572 (Mar. 2007), pp. 208–210. DOI: 10.1016/j.nima.2006.10.198.

[9] The KATRIN Collaboration. "Direct neutrino-mass measurement with sub-electronvolt sensitivity". In: *Nat. Phys.* 18 (2022), pp. 160–166. DOI: 10.1038/s41567-021-01463-1. URL: https://doi.org/10.1038/s41567-021-01463-1.

[10] Guofu Cao. "Search for $0\nu\beta\beta$ decay with EXO-200 and nEXO". In: *PoS* HQL2018 (2018), p. 054. DOI: 10.22323/1.332.0054.

[11] S. M. Bilenky and C. Giunti. "Neutrinoless double-beta decay: A probe of physics beyond the Standard Model". In: *International Journal of Modern Physics A* 30.04n05 (Feb. 2015), p. 1530001. ISSN: 1793-656X. DOI: 10.1142/s0217751x1530001x. URL: http://dx.doi.org/10.1142/S0217751X1530001X.

[12] Felix Boehm and Petr Vogel. *Physics of Massive Neutrinos*. 2nd ed. Cambridge University Press, 1992.

[13] Mathieu BONGRAND. *Results of the NEMO-3 Double Beta Decay Experiment*. 2011. arXiv: 1105.2435 [hep-ex].

[14] D. Q. Adams et al. "New Direct Limit on Neutrinoless Double Beta Decay Half-Life of ^{128}Te with CUORE". In: *Physical Review Letters* 129.22 (Nov. 2022). ISSN: 1079-7114. DOI: 10.1103/physrevlett.129.222501. URL: http://dx.doi.org/10.1103/PhysRevLett.129.222501.

[15] M. Günther et al. "Heidelberg-Moscow $\beta\beta$ experiment with^{76}Ge: Full setup with five detectors". In: *Phys. Rev. D* 55 (1 Jan. 1997), pp. 54–67. DOI: 10.1103/PhysRevD.55.54. URL: https://link.aps.org/doi/10.1103/PhysRevD.55.54.

[16] A. Bettini. "GERDA. Germanium Detector Array. Search for Neutrino-less $\beta\beta$ Decay of 76Ge". In: *Nuclear Physics B - Proceedings Supplements* 168 (2007). Proceedings of the Neutrino Oscillation Workshop, pp. 67–69. ISSN: 0920-5632. DOI: https://doi.org/10.1016/j.nuclphysbps.2007.02.018. URL: https://www.sciencedirect.com/science/article/pii/S0920563207001144.

[17] M. Agostini et al. "Final Results of GERDA on the Search for Neutrinoless Double-β Decay". In: *Physical Review Letters* 125.25 (Dec. 2020). ISSN: 1079-7114. DOI: 10.1103/physrevlett.125.252502. URL: http://dx.doi.org/10.1103/PhysRevLett.125.252502.

[18] Ramkumar Venkataraman. "Chapter 4 - Semiconductor detectors. Contributors to this chapter in previous editions are Jan Verplancke, Paul F. Fettweis, Ramkumar Venkataraman, Brian M. Young, and Harold Schwenn." In: *Handbook of Radioactivity Analysis (Fourth Edition)*. Ed. by Michael F. L'Annunziata. Fourth Edition. Academic Press, 2020, pp. 409–491. ISBN: 978-0-12-814397-1. DOI: https://doi.org/10.1016/B978-0-12-814397-1.00004-2. URL: https://www.sciencedirect.com/science/article/pii/B9780128143971000042.

[19] Eleonora Di Valentino, Stefano Gariazzo, and Olga Mena. "Most constraining cosmological neutrino mass bounds". In: *Physical Review D* 104.8 (Oct. 2021). ISSN: 2470-0029. DOI: 10.1103/physrevd.104.083504. URL: http://dx.doi.org/10.1103/PhysRevD.104.083504.

[20] Kevork Abazajian et al. *Snowmass 2021 CMB-S4 White Paper*. 2022. arXiv: 2203.08024 [astro-ph.CO].

[21] Andrea Pocar et al. "Solar neutrino physics with Borexino". In: *SciPost Physics Proceedings* (Feb. 2019). DOI: 10.21468/SciPostPhysProc.1.025.

[22] T.A. Kirsten et al. "GALLEX solar neutrino results and status of GNO". In: *Nuclear Physics B - Proceedings Supplements* 77.1 (1999), pp. 26–34. ISSN: 0920-5632. DOI: https://doi.org/10.1016/S0920-5632(99)00389-8. URL: https://www.sciencedirect.com/science/article/pii/S0920563299003898.

[23] V. N. Gavrin et al. "First measurement of the integral solar neutrino flux by the Soviet-American Gallium Experiment (SAGE)." In: (1990). Ed. by K. K. Phua and Y. Yamaguchi, pp. 693–697.

[24] K. Arisaka; T. Kajita; T. Kifune; M. Koshiba; K. Miyano; M. Nakahata; T. Suda; A. Suzuki; K. Takahashi; M. Takita; Y. Totsuka. "KAMIOKA Nucleon Decay Experiments; status and performance." In: *AIP Conf. Proc. 114, 54–76 (1984)* 114 (May 1984). Ed. by K. K. Phua and Y. Yamaguchi, pp. 693–697. DOI: https://doi.org/10.1063/1.34507.

[25] M.P. Decowski. "KamLAND's precision neutrino oscillation measurements". In: *Nuclear Physics B* 908 (2016). Neutrino Oscillations: Celebrating the Nobel Prize in Physics 2015, pp. 52–61. ISSN: 0550-3213. DOI: https://doi.org/10.1016/j.nuclphysb.2016.04.014. URL: https://www.sciencedirect.com/science/article/pii/S0550321316300529.

[26] B. Aharmim et al. "Combined Analysis of all Three Phases of Solar Neutrino Data from the Sudbury Neutrino Observatory". In: *Phys. Rev. C* 88 (2013), p. 025501. DOI: 10.1103/PhysRevC.88.025501. arXiv: 1109.0763 [nucl-ex].

[27] Zhiyuan Chen. *Latest results from Daya Bay using the full dataset*. 2023. arXiv: 2309.05989 [hep-ex].

[28] T. Nakaya. *Atmospheric and Long Baseline Neutrino*. 2002. arXiv: hep-ex/0209036 [hep-ex].

[29] N. Agafonova et al. "Final Results of the OPERA Experiment on ν_τ Appearance in the CNGS Neutrino Beam". In: *Phys. Rev. Lett.* 120 (21 2018), p. 211801. DOI: 10.1103/PhysRevLett.120.211801. URL: https://link.aps.org/doi/10.1103/PhysRevLett.120.211801.

[30] M. Sanchez et al. "Measurement of the L/E distributions of atmospheric ν in Soudan 2 and their interpretation as neutrino oscillations". In: *Phys. Rev. D* 68 (11 2003), p. 113004. DOI: 10.1103/PhysRevD.68.113004. URL: https://link.aps.org/doi/10.1103/PhysRevD.68.113004.

[31] K. Abe et al. "Observation of Electron Neutrino Appearance in a Muon Neutrino Beam". In: *Phys. Rev. Lett.* 112 (6 2014), p. 061802. DOI: 10.1103/PhysRevLett.112.061802. URL: https://link.aps.org/doi/10.1103/PhysRevLett.112.061802.

[32] M. A. Acero et al. "First measurement of neutrino oscillation parameters using neutrinos and antineutrinos by NOvA". In: *Physical Review Letters* 123.15 (Oct. 2019). ISSN: 1079-7114. DOI: 10.1103/physrevlett.123.151803. URL: http://dx.doi.org/10.1103/PhysRevLett.123.151803.

[33] Kirk T McDonald. *An Off-Axis Neutrino Beam*. 2001. arXiv: hep-ex/0111033 [hep-ex].

[34] A. Aguilar et al. "Evidence for neutrino oscillations from the observation of $\overline{\nu}\nu_e$ appearance in a $\overline{\nu}\nu_\mu$ beam". In: *Physical Review D* 64.11 (Nov. 2001). ISSN: 1089-4918. DOI: 10.1103/physrevd.64.112007. URL: http://dx.doi.org/10.1103/PhysRevD.64.112007.

[35] Pedro A.N. Machado, Ornella Palamara, and David W. Schmitz. "The Short-Baseline Neutrino Program at Fermilab". In: *Annual Review of Nuclear and Particle Science* 69.1 (2019), pp. 363–387. DOI: 10.1146/annurev-nucl-101917-020949. eprint: https://doi.org/10.1146/annurev-nucl-101917-020949. URL: https://doi.org/10.1146/annurev-nucl-101917-020949.

[36] Lino Miramonti. "Neutrino Physics and Astrophysics with the JUNO Detector". In: *Universe* 126.11 (2018). DOI: 10.3390/universe4110126.

[37] Soo-Bong Kim. *New results from RENO and prospects with RENO-50*. 2014. arXiv: 1412.2199 [hep-ex].

[38] M G Aartsen et al. "PINGU: a vision for neutrino and particle physics at the South Pole". In: *Journal of Physics G: Nuclear and Particle Physics* 44.5 (Apr. 2017), p. 054006. ISSN: 1361-6471. DOI: 10.1088/1361-6471/44/5/054006. URL: http://dx.doi.org/10.1088/1361-6471/44/5/054006.

[39] Piotr Kalaczyński. "KM3NeT/ORCA: status and perspectives for neutrino oscillation and mass hierarchy measurements". In: *Proceedings of 40th International Conference on High Energy physics — PoS(ICHEP2020)*. ICHEP2020. Sissa Medialab, Feb. 2021. DOI: 10.22323/1.390.0149. URL: http://dx.doi.org/10.22323/1.390.0149.

[40] A. Abed Abud et al. *Snowmass Neutrino Frontier: DUNE Physics Summary*. 2022. arXiv: 2203.06100 [hep-ex].

[41] J. Bian et al. *Hyper-Kamiokande Experiment: A Snowmass White Paper*. 2022. arXiv: 2203.02029 [hep-ex].

[42] Sanjib Kumar Agarwalla, Suprabh Prakash, and S. Uma Sankar. "Resolving the octant of θ_{23} with T2K and NOvA". In: *JHEP* 07 (2013), p. 131. DOI: 10.1007/JHEP07(2013)131. arXiv: 1301.2574 [hep-ph].

[43] Ivan Esteban et al. "The fate of hints: updated global analysis of three-flavor neutrino oscillations". In: *Journal of High Energy Physics* 2020.9 (Sept. 2020). ISSN: 1029-8479. DOI: 10.1007/jhep09(2020)178. URL: http://dx.doi.org/10.1007/JHEP09(2020)178.

[44] K. Abe et al. *Proposal for an Extended Run of T2K to* 20×10^{21} *POT*. 2016. arXiv: 1609.04111 [hep-ex].

[45] K. Abe et al. "Constraint on the matter-antimatter symmetry-violating phase in neutrino oscillations". In: *Nature* 580.7803 (Sept. 2020), pp. 339–344. ISSN: 1029-8479. DOI: 10.1038/s41586-020-2177-0. URL: https://doi.org/10.1038/s41586-020-2177-0.

[46] M. A. Acero et al. "Improved measurement of neutrino oscillation parameters by the NOvA experiment". In: *Phys. Rev. D* 106.3 (2022), p. 032004. DOI: 10.1103/PhysRevD.106.032004. arXiv: 2108.08219 [hep-ex].

[47] B. Abi et al. "Volume I. Introduction to DUNE". In: *Journal of Instrumentation* 15.08 (2020), T08008. DOI: 10.1088/1748-0221/15/08/T08008. URL: https://dx.doi.org/10.1088/1748-0221/15/08/T08008.

[48] M. Bass et al. "*Baseline optimization for the measurement of of CP violation, mass hierarchy, and θ_{23} octant in a long-baseline neutrino oscillation experiment*". In: *Physical Review D* 91.5 (Mar. 2015). ISSN: 1550-2368. DOI: 10.1103/physrevd.91.052015. URL: http://dx.doi.org/10.1103/PhysRevD.91.052015.

[49] B. Abi et al. "*Long-baseline neutrino oscillation physics potential of the DUNE experiment: DUNE Collaboration*". In: *The European Physical Journal C* 80.10 (Oct. 2020). ISSN: 1434-6052. DOI: 10.1140/epjc/s10052-020-08456-z. URL: http://dx.doi.org/10.1140/epjc/s10052-020-08456-z.

[50] Steve Ritz et al. "Building for Discovery: Strategic Plan for U.S. Particle Physics in the Global Context". In: (May 2014).

[51] B. Abi et al. *Deep Underground Neutrino Experiment (DUNE), Far Detector Technical Design Report, Volume II: DUNE Physics*. 2020. arXiv: 2002.03005 [hep-ex].

[52] DUNE Collaboration et al. *Long-Baseline Neutrino Facility (LBNF) and Deep Underground Neutrino Experiment (DUNE) Conceptual Design Report Volume 2: The Physics Program for DUNE at LBNF*. 2016. arXiv: 1512.06148 [physics.ins-det].

[53] R. Acciarri et al. *Long-Baseline Neutrino Facility (LBNF) and Deep Underground Neutrino Experiment (DUNE) Conceptual Design Report Volume 1: The LBNF and DUNE Projects*. 2016. arXiv: 1601.05471 [physics.ins-det].

[54] Sabrina Sacerdoti. "A LArTPC with Vertical Drift for the DUNE Far Detector". In: *PoS* NuFact2021 (2022), p. 173. DOI: 10.22323/1.402.0173.

[55] A. Abed Abud et al. *Deep Underground Neutrino Experiment (DUNE) Near Detector Conceptual Design Report*. 2021. arXiv: 2103.13910 [physics.ins-det].

[56] Valentina Cicero. "Study of the tracking performance of a liquid Argon detector based on a novel optical imaging concept". PhD thesis. Alma Mater Studiorum - Università di Bologna, amsdottorato, Bologna U., 2023. DOI: 10.48676/unibo/amsdottorato/10871..

[57] Matteo Vicenzi. "A GRAIN of SAND for DUNE: Development of simulations and reconstruction algorithms for the liquid Argon target of the SAND detector in DUNE". PhD thesis. Genoa U., 2023. DOI: 10.15167/vicenzi-matteo_phd2023-01-20.

[58] G. Adamov et Al. "A proposal to enhance the DUNE Near-Detector Complex". In: (May 2021).

[59] K.D. Smith et al. "Progress in the design and manufacture of the KLOE solenoid for the DAPHNE ring at Frascati". In: *IEEE Transactions on Applied Superconductivity* 7.2 (1997), pp. 630–632. DOI: 10.1109/77.614583.

[60] M Adinolfi et al. "The KLOE electromagnetic calorimeter". In: *Nuclear Instruments and Methods in Physics Research Section A: Accelerators, Spectrometers, Detectors and Associated Equipment* 482.1 (2002), pp. 364–386. ISSN: 0168-9002. DOI: https://doi.org/10.1016/S0168-9002(01)01502-9. URL: https://www.sciencedirect.com/science/article/pii/S0168900201015029.

[61] Valerio Pia. "Study of the calorimetric performance of a liquid Argon detector based on a novel optical imaging concept". PhD thesis. alma, June 2023. URL: http://amsdottorato.unibo.it/10933/.

[62] Ettore Segreto. "Properties of liquid argon scintillation light emission". In: *Physical Review D* 103.4 (Feb. 2021). ISSN: 2470-0029. DOI: 10.1103/physrevd.103.043001. URL: http://dx.doi.org/10.1103/PhysRevD.103.043001.

[63] Ettore Segreto. "Properties of liquid argon scintillation light emission". In: *Phys. Rev. D* 103 (4 Feb. 2021), p. 043001. DOI: 10.1103/PhysRevD.103.043001. URL: https://link.aps.org/doi/10.1103/PhysRevD.103.043001.

[64] M. Babicz et al. "A measurement of the group velocity of scintillation light in liquid argon". In: *Journal of Instrumentation* 15.09 (Sept. 2020), P09009. DOI: 10.1088/1748-0221/15/09/P09009. URL: https://dx.doi.org/10.1088/1748-0221/15/09/P09009.

[65] A. Neumeier et al. "Intense vacuum ultraviolet and infrared scintillation of liquid Ar-Xe mixtures". In: *Europhysics Letters* 109.1 (Jan. 2015), p. 12001. DOI: 10.1209/0295-5075/109/12001. URL: https://dx.doi.org/10.1209/0295-5075/109/12001.

[66] Hamamatsu Photonics. *MPPC S14160-3050*. 2022. URL: https://www.hamamatsu.com/eu/en/product/optical-sensors/mppc/mppc_mppc-array/S14160-3050HS.html (visited on 01/19/2024).

[67] C. Andreopoulos et al. "The GENIE neutrino Monte Carlo generator". In: *Nuclear Instruments and Methods in Physics Research Section A: Accelerators, Spectrometers, Detectors and Associated Equipment* 614.1 (2010), pp. 87–104. ISSN: 0168-9002. DOI: https://doi.org/10.1016/j.nima.2009.12.009. URL: https://www.sciencedirect.com/science/article/pii/S0168900209023043.

[68] Clark D. McGrew. *edep-sim*. 2021. URL: https://github.com/ClarkMcGrew/edep-sim.git (visited on 01/21/2024).

[69] M Szydagis et al. "Enhancement of NEST capabilities for simulating low-energy recoils in liquid xenon". In: *Journal of Instrumentation* 8.10 (Oct. 2013), p. C10003. DOI: 10.1088/1748-0221/8/10/C10003. URL: https://dx.doi.org/10.1088/1748-0221/8/10/C10003.

[70] Ludwig Strauss and George Kontaxakis. "Maximum Likelihood Algorithms for Image Reconstruction in Positron Emission Tomography". In: *Radionuclides Oncol* (June 1998).

[71] François Chollet. *Deep Learning with Python*. Manning, Nov. 2017. ISBN: 9781617294433.

[72] Aurelien Geron. *Hands-On Machine Learning with Scikit-Learn, Keras, and TensorFlow: Concepts, Tools, and Techniques to Build Intelligent Systems*. 2nd. O'Reilly Media, Inc., 2019. ISBN: 1492032646.

[73] Yingying Wang et al. "The Influence of the Activation Function in a Convolution Neural Network Model of Facial Expression Recognition". In: *Applied Sciences* 10.5 (2020). ISSN: 2076-3417. DOI: 10.3390/app10051897. URL: https://www.mdpi.com/2076-3417/10/5/1897.

[74] Sebastian Ruder. *An overview of gradient descent optimization algorithms*. 2017. arXiv: 1609.04747 [cs.LG].

[75] Martin Ester et al. "A Density-Based Algorithm for Discovering Clusters in Large Spatial Databases with Noise". In: *Knowledge Discovery and Data Mining*. 1996. URL: https://api.semanticscholar.org/CorpusID:355163.

[76] J. J. Back et al. "Implementation of a local principal curves algorithm for neutrino interaction reconstruction in a liquid argon volume". In: *The European Physical Journal C* 74.3 (Mar. 2014). ISSN: 1434-6052. DOI: 10.1140/epjc/s10052-014-2832-4. URL: http://dx.doi.org/10.1140/epjc/s10052-014-2832-4.

[77] Richard O. Duda and Peter E. Hart. "Use of the Hough transformation to detect lines and curves in pictures". In: *Commun. ACM* 15.1 (Jan. 1972), pp. 11–15. ISSN: 0001-0782. DOI: 10.1145/361237.361242. URL: https://doi.org/10.1145/361237.361242.

[78] Mohamamd Rezaei. "Clustering validation". PhD thesis. June 2016.

[79] Jörg Sander et al. "Density-Based Clustering in Spatial Databases: The Algorithm GDBSCAN and Its Applications". In: *Data Mining and Knowledge Discovery* 2.2 (1998), pp. 169–194. DOI: 10.1023/A:1009745219419. URL: https://doi.org/10.1023/A:1009745219419.

[80] Karl Pearson. "LIII. On lines and planes of closest fit to systems of points in space". In: *The London, Edinburgh, and Dublin Philosophical Magazine and Journal of Science* 2.11 (1901), pp. 559–572. DOI: 10.1080/14786440109462720. URL: https://doi.org/10.1080/14786440109462720.

[81] Trevor Hastie and Werner Stuetzle. "Principal Curves". In: *Journal of the American Statistical Association* 84.406 (1989), pp. 502–516. DOI: 10.1080/01621459.1989.10478797. URL: https://www.tandfonline.com/doi/abs/10.1080/01621459.1989.10478797.

[82] Jochen Einbeck, Gerhard Tutz, and Ludger Evers. "Local principal curves". In: *Statistics and Computing* 15.4 (Oct. 2005), pp. 301–313. DOI: 10.1007/s11222-005-4073-8. URL: https://doi.org/10.1007/s11222-005-4073-8.

[83] P V.C. Hough. "METHOD AND MEANS FOR RECOGNIZING COMPLEX PATTERNS". In: (Dec. 1962). URL: https://www.osti.gov/biblio/4746348.

[84] Azriel Rosenfeld. "Picture Processing by Computer". In: *ACM Comput. Surv.* 1.3 (Sept. 1969), pp. 147–176. ISSN: 0360-0300. DOI: 10.1145/356551.356554. URL: https://doi.org/10.1145/356551.356554.